

PhD in Astroparticle Physics, XXXII cycle



GRAN SASSO SCIENCE INSTITUTE

---

**Exploring the Inelastic Dark Matter frontier  
with the CRESST experiment**

*PhD candidate:*  
Miriam OLMÍ

*Internal Advisor:*  
Paolo GORLA (LNGS - INFN)

*External Advisor:*  
Federica PETRICCA (MPP - Munich)



# Contents

<b>Introduction</b>	<b>7</b>
<b>Acknowledgement</b>	<b>9</b>
<b>1 Dark Matter</b>	<b>11</b>
1.1 Evidence for Dark Matter	12
1.1.1 Velocity dispersion and Coma Cluster	12
1.1.2 Galactic rotation curve	12
1.1.3 Gravitational lensing and Bullet Cluster	14
1.1.4 Cosmic Microwave Background	15
1.1.5 Other indirect evidence	16
1.2 Models and candidates	18
1.3 The inelastic dark matter framework	22
1.3.1 iDM interaction	23
1.3.2 Kinematics of iDM	23
1.3.3 Rate in the iDM framework	26
1.4 Detection of WIMPs	29
1.4.1 Elastic dark matter rate	30
1.4.2 Experimental approaches for direct dark matter searches	32
<b>2 The CRESST experiment</b>	<b>37</b>
2.1 Background and shielding	37
2.2 CRESST Cryostat	41
2.3 CRESST detector	43
2.3.1 Cryogenic detector	43
2.3.2 The CRESST-III detector	44
2.3.3 Transition Edge Sensor	45
2.3.4 Working principle	46
2.3.5 Background discrimination	48
2.4 Inelastic dark matter search with CRESST	53
2.5 Data acquisition	54
2.5.1 TES readout	54
2.5.2 TES response	55
2.5.3 Recorded pulses	55
2.5.4 Control and heater pulses	56

<b>3</b>	<b>Raw data analysis</b>	<b>59</b>
3.1	Data sets . . . . .	59
3.2	Event types . . . . .	60
3.3	Analysis chain . . . . .	60
3.4	Stability and Rate Cut . . . . .	62
	3.4.1 Stability Cut . . . . .	62
	3.4.2 Rate Cut . . . . .	64
3.5	Gamma calibration data . . . . .	65
	3.5.1 Template creation . . . . .	65
	3.5.2 Fit procedure and Truncation Limit . . . . .	67
	3.5.3 Conversion from Pulse height to Energy (CPE factor) . . . . .	68
3.6	Background data . . . . .	69
	3.6.1 Data quality cuts . . . . .	69
	3.6.2 Carrier cut . . . . .	70
	3.6.3 Coincidences cuts . . . . .	74
	3.6.4 Light Yield plot and $\eta$ factor . . . . .	74
3.7	Neutron calibration data . . . . .	77
3.8	Cut Efficiency . . . . .	78
3.9	Trigger Threshold . . . . .	79
<b>4</b>	<b>Band fit</b>	<b>83</b>
4.1	Energy resolution . . . . .	83
4.2	Electron/Gamma Band . . . . .	84
	4.2.1 Mean line . . . . .	84
	4.2.2 Width . . . . .	84
	4.2.3 Excess light events . . . . .	85
4.3	Nuclear recoil Band . . . . .	86
4.4	Energy spectra . . . . .	86
	4.4.1 Electron rate . . . . .	87
	4.4.2 Gamma rate . . . . .	88
	4.4.3 Neutron rate . . . . .	88
	4.4.4 DM rate . . . . .	89
4.5	Density Functions . . . . .	89
4.6	Band fit results . . . . .	90
<b>5</b>	<b>Exclusion limit</b>	<b>95</b>
5.1	Extended Likelihood function . . . . .	95
	5.1.1 Logarithmic Likelihood . . . . .	97
	5.1.2 Profile Likelihood . . . . .	97
5.2	Calculating the exclusion limit . . . . .	97
5.3	Results . . . . .	99
<b>6</b>	<b>Conclusions and outlook</b>	<b>111</b>
	<b>Appendices</b>	<b>113</b>

---

<b>A</b>	<b>Inelastic dark matter rate derivation</b>	<b>115</b>
<b>B</b>	<b>Detector modules details</b>	<b>119</b>
B.1	Detector Anja . . . . .	120
B.2	Detector Daisy . . . . .	122
B.3	Detector Lise . . . . .	124
B.4	Detector VK31 . . . . .	126
B.5	Detector VK34 . . . . .	128
B.6	Detector Frederika . . . . .	130
B.7	Detector Verena . . . . .	132
B.8	Detector VK33 . . . . .	134
B.9	Detector Zora . . . . .	136
	<b>Bibliography</b>	<b>136</b>



## Introduction

The quest for the nature of dark matter (DM) is one of the most fundamental in today's physics research. Until today the existence of DM is inferred by indirect (gravitational) effects. The best interpretation to date of these observations is the existence of new massive particles with an interaction cross section at the (sub)weak scale. This explanation sets some strict requests for the DM candidate (cold, stable and interacting only gravitationally and sub-weak) but leaves a wide range of properties completely unconstrained. The most commonly searched dark matter candidate, the WIMP (Weak Interacting Massive Particle), is only one among all the possible candidates to solve the DM puzzle. One interesting possibility, explored in many theoretical frameworks, is that dark matter predominantly scatters inelastically off nuclei, causing the DM particle to up-scatter into an excited state.

In the work of Bramante et al. [1] the inelastic scattering framework is widely investigated with a particular focus on the available kinematic phase space depending on the target nucleus. This article pointed out that, for a fixed dark matter mass, the heavier the target mass the larger mass splitting will be accessible. Among all the direct dark matter searches CRESST [2] (Cryogenic Rare Event Search with Superconducting Thermometer) is the most suitable for probing the inelastic dark matter (iDM) scenario, being tungsten the heaviest target element used in such experiments at present. CRESST is one of the leading experiments for a light direct dark matter search. Located at the Laboratori Nazionali del Gran Sasso (Abruzzo, Italy), CRESST target consists of arrays  $\text{CaWO}_4$  crystals operated at a temperature of few mK. For each crystal both the phonon and light signal produced by a particle interaction are detected, allowing particle identification as well as a precise energy measurement.

In this PhD thesis the analysis of CRESST data in the framework of the inelastic dark matter scenario is presented. This work is focused on the combination of the results from multiple detector modules to exploit the total exposure of the experiment. Due to kinematic reasons, the iDM is characterised by a suppressed effective DM-nuclear scattering rate and a minimum recoil energy in the detector, corresponding to the minimum required energy for inelastic DM-nuclear collisions to happen. In light of these considerations, CRESST-II [3] phase 2 data have been chosen for this analysis instead of more recent data in order to increase the total exposure available. The target mass of a CRESST-II detector is more than 10 times larger than the one of CRESST-III detector leading to a gross exposure of  $\sim 160$  kg d for each detector module in the data taking campaign considered

in this work.

In the manuscript the raw data analysis procedures, which require in this case optimizing calibration and linearisation of the individual detector response for a non-standard region of interest, are described in detail. Particular attention is devoted to the explanation of the data quality selections performed on the background data to remove all the signals due to non-physical processes. This procedure is not trivial because each detector has an individual behaviour and specific populations of events that need to be understood and associated with the physical/non-physical process that caused them. A blind analysis is performed using a small part of the data set ( $\sim 20\%$ ) as training data to define all the selections. These are then applied blindly to the full data set avoiding any unwanted bias. For all detector modules a dedicated simultaneous fit of the energy spectra measured by the phonon and light detector has been performed to optimise particle identification and thus improve background discrimination.

The expected iDM spectrum in the CRESST modules has been produced and compared with the measured one for each module and the exclusion limit on the iDM cross section was obtained for each module. The background discrimination performances as well as the exclusion limit of each detector have been evaluated carefully and only the most suitable modules have been selected for the final combined analysis. Finally the results obtained with the chosen detectors have been combined. With the resulting enhanced exposure obtained from CRESST-II phase 2 data the final exclusion limit on the inelastic dark matter cross section is given.

## Acknowledgement

Writing a thesis is never an easy task, but this is true especially for a PhD thesis, for which many people's help and support is fundamental. For this reason I would like to use this opportunity to say thank to all of you for the encouragement I experienced during the last (almost) four years.

First of all I would like to thank my advisors Paolo Gorla and Federica Petricca. Paolo, thank you for the patient and constant supervision during all these years, in particular in the last months. Federica, without you this thesis would not have been possible.

Secondly, I would like to thank the CRESST Analysis team, especially Florian, Martin, Philipp, Daniel and Christian, for all the fruitful discussions and advice you gave me along all my analysis work.

After the Analysis team, I would like to thank of course all my CRESST colleagues for the joint effort we put to keep the experiment running and growing and obviously also for all the nice meetings and dinners we had during the past two years. A special mention to Valentyna: thank you for all our peculiar chats!

Now it is time for thanking the merged CRESST-CUORE group at LNGS. Thank you Carlo, Laura and Giovanni for the useful and funny meetings Laura was able to arrange: they were precious for my work and my personal growth, especially in preparing and giving talks!

A dedicated thank goes to Nello, my office mate. Thank you for your patience in teaching me your cryogenic knowledge and for your enthusiasm for everything related to physics and life in general!

I would also like to thank Roberta, Alessia and all the LNGS Outreach team for the opportunity of helping in organizing all the events of popular science of the last 3 years: it has taught me a lot.

I am deeply grateful to Francesco Vissani: you have been one of the person to refer to for problems and suggestions of any type during all these years. Thank you for being always so kind and sincere.

The working atmosphere at LNGS would have been way more empty, sad and hard if I had not found an amazing group of friends always ready to encourage me and make me laugh. Thank you Giovanni, Irene, Daniele, Andrea, Valentina, Ambra and Guido for being there at anytime for a coffee, a ping-pong match, a stupid video on YouTube and many other similar things.

In the same way I want to thank all my friends and PhD-colleagues of GSSI. Thank you Enri, Zhao, Carlo, Benny, Ody and Alex for having make my life downtown in AQ so hilarious and filled with social life. Thank you of course also

to the other GSSI AP (AstroParticle) students: I have neither the time nor the space to write down all your names and, in case, I would for sure forget someone so I go for a big and unique thank to all of you.

In addition to my LNGS and GSSI friends and colleagues I would really like to thank my friends of the Basilica di San Bernardino: the friars, the choir and the UACF guys. You have been an important part of my off-work life, probably more than you can imagine.

Despite for obvious reasons I have spent most of my time in L'Aquila, I would really like to thank my friend in Firenze. Thank you Alberto, Stefano, Lorenzo, Chiara M., AlessandraAmore for all the nice chats and calls during which we annoyed each other with the PhD-life problems: it was important to feel I was not alone.

Thank you Chiara&Ros, Ire, ValeMele and Lau for having always found some time to have a coffee whenever I was back home, no matter the short notice of my messages.

Thank you Bianca, Babe, Lele and Cami for being able to keep alive our friendship even though our lives have become so different now.

I am sincerely thankful to my colleague and friend and above all flatmate Vanessa. As my first (and unique) flatmate thank you for helping me find out what I am capable of: it has been an adventure full of surprises! Thank you for every single moment of our life together in this four years. Thank you for being present and understanding with me during my dark days and at the same time thank you letting me be present for yours.

A special thought goes to Stefano: thanks for helping me in an infinity of situations, from the analysis of this work to the (dead and alive) spiders occasionally popping out in my apartment, from L<sup>A</sup>T<sub>E</sub>X issues to moments of despair both partially due to this thesis. In one phrase, thank you for being always there whenever I need you.

Last but not least I thank all my family: my parents, my sisters and my uncles and cousins. Thank you all for being always extremely supportive and present for me despite the distance, that has been so hard to bear especially in the last few months.

## Dark Matter

The first to suggest the existence of dark matter, using stellar velocities, was Dutch astronomer Jacobus Kapteyn in 1922 [4]. Ten years later also the fellow Dutchman and radio astronomy pioneer Jan Oort hypothesized the existence of dark matter while studying stellar motion in the local galactic neighborhood [5].

In 1933 the Swiss astrophysicist Fritz Zwicky made an analogous deduction after studies of galaxy clusters while working at the California Institute of Technology [6–8]. Zwicky applied the virial theorem to the Coma Cluster and found the velocity dispersion of its members was too high to keep the system stable. From this result he deduced the presence of some unseen mass that he called *dunkle Materie* ('dark matter'). Zwicky's estimates were off by more than an order of magnitude, mainly because of an obsolete value of the Hubble constant. The same calculation today shows a smaller fraction, using greater values for luminous mass. Nonetheless, Zwicky did correctly conclude from his calculation the bulk of the matter was dark.

Further indications the mass-to-light ratio was not unity came from measurements of galaxy rotation curves in the following years [9, 10]. In the 1960s and 1970s Vera Rubin, Kent Ford, and Ken Freeman's work provided further strong evidence, again using galaxy rotation curves [11, 12]. In 1980 Rubin and Ford published a paper [13] in which they showed most galaxies must contain about six times as much dark as visible mass making dark matter one of the major unsolved problem in astronomy.

At the same time Rubin and Ford were exploring optical rotation curves, radio astronomers were making use of new radio telescopes to map the 21 cm line of atomic hydrogen in nearby galaxies showing that also the H-I rotation curve did not trace the expected Keplerian decline [14–17].

A stream of observations in the 1980s supported the presence of dark matter, including gravitational lensing of background objects by galaxy clusters, the temperature distribution of hot gas in galaxies and clusters, and the pattern of anisotropies in the cosmic microwave background. According to all the evidences collected in the last decades, dark matter is composed primarily of a not yet characterized type of subatomic particle. The search for this particle, by a variety of means, is one of the major efforts in particle physics, as well as in astrophysics and cosmology.

## 1.1 Evidence for Dark Matter

### 1.1.1 Velocity dispersion and Coma Cluster

The velocity dispersion is the spread of velocities in group of objects such as stars or galaxies in a cluster. Stars or galaxies in a cluster have in fact individual velocities which differs from the mean velocity of the cluster. The velocity dispersion can be estimated measuring the radial velocities of the members of the cluster and this is performed measuring the Doppler width of their spectral lines. Through the virial theorem the total mass of the cluster can be derived from the information of the velocity dispersion as Zwicky did for the first time in 1933 with the Coma Cluster [6, 7]. The Coma Cluster (Abell 1656) is a large cluster of galaxies and up to now more than 1000 galaxies have been identified inside it.

In 1930s the Coma Cluster was one of the best investigated cluster and measurements of the radial velocities of its components led to apparent differences in velocity of  $1500 \div 2000$  km/s. In his paper Zwicky presented several considerations related to this enormous velocity dispersion. If the Coma Cluster is in a mechanically stationary state, the virial theorem can be applied. Considering a total mass of the cluster coming from all the luminous matter, the root-mean-square velocity of the cluster obtained from this calculation is of the order of 80 km/s. In order to obtain, as observed, a Doppler effect of the order of  $\sim 1000$  km/s the mass of the cluster should be larger and this would request an higher density (of at least a factor 400) since the dimension of the cluster are known from other observations. The other possibility is that the system is not in stationary equilibrium. In this case the entire available potential energy appears as kinetic energy but still this would be not enough and the need of an higher density still would remain. Zwicky discussed also the case of average density determined only by luminous matter. In this case, however, the observed velocities should make the Coma system fly apart in the course of time. If this would be the case, single nebulae with large proper speed should be observed as result of the expansion of clusters but this hardly matches the experimental data. Finally such high velocity dispersion cannot be due to redshift because the change of wavelength would be too small in the hypothesis of a total mass equal to the luminous one.

These calculations were improved in the following years [8] but the large velocity dispersion in the Coma cluster as well as in other dense clusters of nebulae have remained an unsolved problem for a long time. After other dark matter evidence was found, the Coma Cluster has been considered the first evidence of dark matter thanks to Zwicky work.

### 1.1.2 Galactic rotation curve

The rotation curve of a galaxy shows the circular velocity (i.e. the orbital speed) of stars as a function of their radial distance from the galactic center. For a spiral galaxy there is a central bulge where most of the mass is concentrated and

the spiral arms are spread over a disk. A star in a spiral galaxy set at a distance  $r$  from the galactic center and moving with a circular velocity  $v(r)$  experiences the gravitational force balancing the centrifugal force according to the following equation:

$$\frac{mv(r)^2}{r} = \frac{GmM(r)}{r^2} \quad (1.1)$$

where  $M(r)$  is the mass within the radius  $r$ . If the star is inside the dense central region of the galaxy, then  $M(r) = \frac{4}{3}\pi r^3 \rho$ , where  $\rho$  is the average density of the central hub. Therefore the orbital speed in the central region is expected to be linear with the radius:  $v(r) \sim r$ . On the other side for a star outside this dense central hub, the mass  $M(r)$  can be considered constant and this leads to a orbital speed decreasing with increasing radius according to:  $v(r) \sim 1/\sqrt{r}$ .

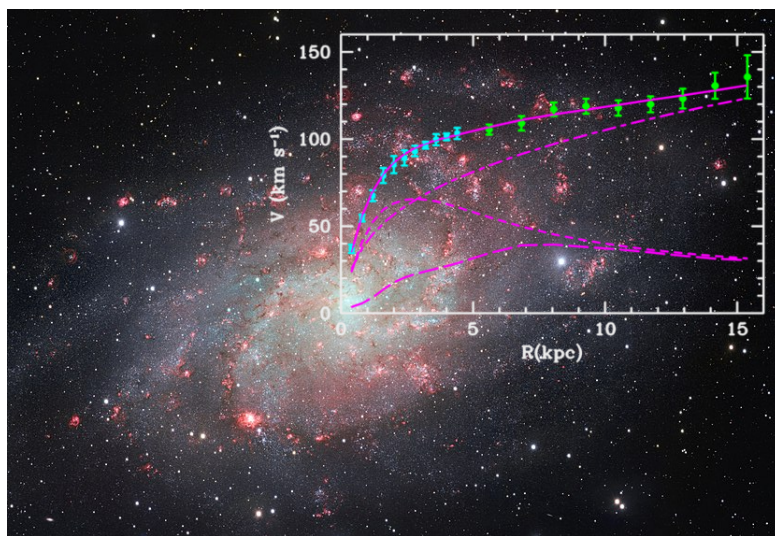


Figure 1.1: VST's very detailed image of Triangulum Galaxy [18] with its rotation curve on top. Experimental points with error bars come from optical and radio measurements respectively in cyan and green. Experimental points are compared with a recent mass distribution model (continuous line). Also shown the halo contribution (dashed-dotted line), the stellar disk (short dashed line) and the gas contribution (long dashed line) [19].

In the hypothesis of a correct modelling of the galaxy mass distribution the rotation curve should show an initial increase corresponding to the central hub and then it should drop to zero according to  $1/\sqrt{r}$ . The experimental data of rotation curves for several spiral galaxies are not supporting such hypothesis. For large  $r$  the orbital speed present a constant behaviour suggesting the presence of a immense hidden mass inside the galaxy. This so-called “dark matter” is now believed to form a “halo” in which the galaxy is embedded. As an example the rotation curve of the Triangulum Galaxy (catalogued as Messier 33, M33 or NGC598) is shown in figure 1.1 above an image of the same galaxy. The experimental data with relative error bars are depicted in cyan and green according to their origin: optical and radio measurements. In dashed magenta the

different contributions to the mass distribution are shown: halo, stellar disk and gas contribution are drawn in dashed-dotted, short dashed and long dashed line respectively. The solid magenta line corresponds to the sum of the three contributions [19].

### 1.1.3 Gravitational lensing and Bullet Cluster

The gravitational lensing is a phenomenon corresponding to the bending of light while it passes close to a gravitating mass. It is a direct consequence of Einstein's general theory of relativity. The gravitating mass curves the surrounding time-space and then light follows such curved time-space giving rise to the lensing effect in which the mass acts as a lens to the light coming from a background object. This lensing effect can be classified into three categories, namely strong lensing, weak lensing and micro-lensing. When the gravitational lens has enough mass to deflect the light from the source in the background so to form multiple images of it, arcs or even rings we talk of strong lensing. If instead the image of the background object is "simply" distorted or deformed because the mass of the gravitational lens is massive enough the weak lensing term is used. Finally in case of gravitational micro-lensing an object in the background has a brightness that changes in time, the so-called "apparent brightness", due to the small gravitational lens passing by the source in a reasonable amount of time.

Making use of strong and weak gravitational lensing one of the most compelling evidences of dark matter was discovered: the "bullet cluster" or more formally the cluster 1E 0657-56 (see figure 1.2). The bullet cluster was discovered in 1998 [20] and consists of two clusters of galaxies<sup>1</sup> that collided at a distance of  $\sim 4 \cdot 10^9$  light years ( $\sim 1$  Gpc) from the Earth in the constellation Carina. Observed from Earth, the sub-cluster passed through the center of the larger cluster 150 million years ago creating a "bow-shaped" shock wave near the right side of the cluster.

The x-ray analyses reveals the baryonic mass distribution of the two colliding clusters while the weak and strong lensing reconstruct the dark matter components present inside them. From the analysis the effect of the collision was revealed. After the collision in fact the baryonic mass distribution of the smaller cluster took the shape of a bullet (and hence the name). Moreover the "normal" baryonic matter of each colliding cluster was displaced from its respective dark matter halo while the two dark matter halos themselves passed through each other rather unperturbed and undistorted.

Many other hypotheses have emerged aiming to explain the observational phenomena that dark matter was conceived to explain and the most common consists in modifying gravity. A problem with alternative hypotheses is that dark matter evidences come from many independent approaches and succeed in explaining all of them with a unique model is very difficult. Because of these

---

<sup>1</sup>More precisely with the term 'bullet cluster' the smaller sub-cluster moving away from the larger one is denoted.

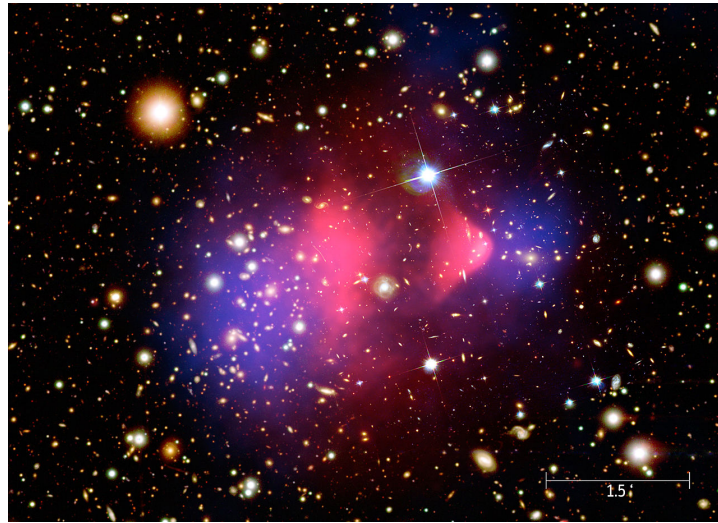


Figure 1.2: Bullet cluster: X-ray image (pink) superimposed over a visible light image (galaxies), with the dark matter distribution calculated from gravitational lensing (blue).

results the “Bullet Cluster” is considered to provide the best evidence of the existence of dark matter [21, 22] and suggests its collisionless nature. Similar results were also obtained for the cluster MACS J0025.4-1222 [23].

#### 1.1.4 Cosmic Microwave Background

The Cosmic Microwave Background (CMB) is a very homogeneous electromagnetic radiation that permeates the Universe. It has been observed in all directions of the sky and its emission peak is located in the microwave domain, from which the name. According to the “Standard Cosmological Model”, the universe expanded from an initial state characterized by very high-density and high-temperature. In this state the temperature was so high that atomic bound states were not possible and thus the electromagnetic radiation could not travel freely: it was scattered off the many charged particles contained in this early universe. Because of the continuous expansion both temperature and density decreased until the formation of hydrogen atoms was finally possible. This condition determines the so-called “recombination epoch”. At the same time the universe became transparent to radiation that could travel through the universe without interacting with matter and constitutes the present CMB radiation. For this reason it is often referred to as “relic radiation” of the early universe.

The CMB radiation was discovered in 1964 by Arno Penzias and Robert Wilson, two American scientists working at Bell Telephone Laboratories in New Jersey, that were studying microwave emission from the Milky Way to identify and eliminate unwanted interference in satellite communications. They published their detection in 1965 [24] and their finding earned the two physicists the 1978 Nobel Prize in Physics. As a matter of fact, theorists had predicted the exis-

tence and the general properties of the CMB well before its discovery [25–27]. They estimated the CMB temperature to be at about 3K but this part of the electromagnetic spectrum is difficult to observe from ground and only after 25 years astronomers could demonstrate all its properties. In 1990 the COsmic Background Explorer (COBE), a NASA satellite dedicated to cosmology, measured the spectrum of the CMB radiation and confirmed it is well described by a black-body with a temperature of just over 2.7 K [28]. After few years of data taking another feature of the CMB radiation predicted by theorists was confirmed: its high level of isotropy with very faint anisotropies of the order  $\sim 10^{-5}$  [29]. Inspired by the COBE results, several experiments measured the cosmic microwave background radiation. The most important results were obtained with WMAP [30] and Planck [31] and all these observations have led to a strong confirmation of the “Standard Model of Cosmology”.

In particular from the CMB anisotropy, measurements constraints on several cosmological parameters can be obtained. One possible way of investigating CMB anisotropies is by looking at the scales at which such small temperature variations occur and this can be done through a decomposition in spherical harmonics. The power spectrum of the CMB fluctuation thus obtained is usually expressed in terms of the multipole moment or angular scale. The power spectrum obtained with the most recent data is presented in figure 1.3. The horizontal axis here is logarithmic for the lowest multipoles and linear for the other multipoles. The gray sold line corresponds to the best fit of the standard model. Three peaks dominates the spectrum and from such peaks the constraints on most of the cosmological parameters are obtained. The height of the first peak is linked to the density of baryons in the universe. Moreover the angular scale of this peak is an indicator of the universe geometry. Since the CMB radiation comes from the farthest edge of the visible universe, its light might be distorted by the eventual cosmic curvature. According to the position of this peak in the power spectrum the universe is very close to spatially flat. The second peak is related to the amount of matter in the universe while the third peak is associated to the density of dark matter. More precisely the relative height of the second and the third peak give information on the ratio of baryonic matter to dark matter: without dark matter the second peak would have not be present. Last release of Planck analysis presents a dark matter density  $\Omega_c h^2 = (0.120 \pm 0.001)$ , a baryon density  $\Omega_b h^2 = (0.0224 \pm 0.0001)$ , a matter density parameter  $\Omega_m h^2 = (0.1428 \pm 0.0011)$  and finally a constrain on the neutrino mass  $\Sigma m_\nu \leq 0.12$  eV [32].

### 1.1.5 Other indirect evidence

The ones described in the last pages are only some of the several evidences of dark matter collected in the last 50 years. Other measurements had been carried out to further investigate the universe and refine the standard ad model of cosmology.

Type Ia supernovae result from the nuclear explosion of white dwarfs. As the explosion is possible only above a certain critical mass, type Ia supernovae shine with about the same brightness and therefore can be used as standard candles

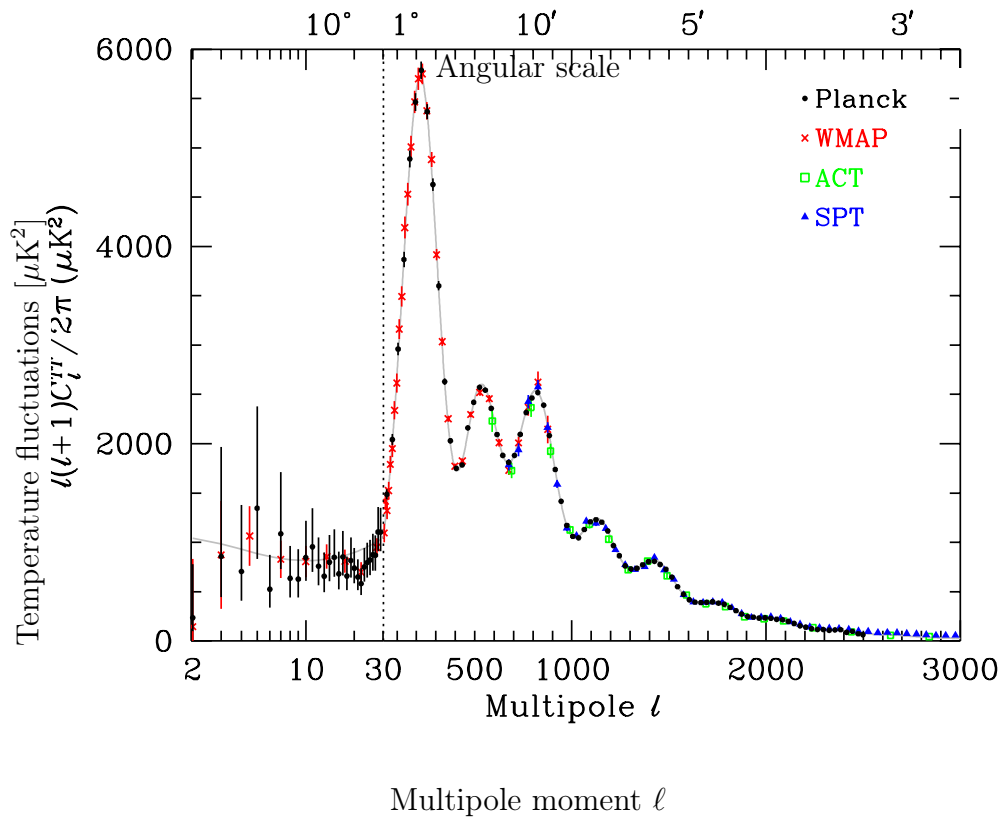


Figure 1.3: The CMB temperature anisotropy power spectrum in terms of the angular scale (top axis) or multipole moment (bottom axis). The horizontal axis here is logarithmic for the lowest multipoles and linear for the other multipoles. The experimental points come from the Planck(2018), WMAP(2013), ACT(2014) and SPT(2013) experiments. The best fit of the Planck  $\Lambda$ CDM model is shown with gray solid line.

to measure extra-galactic distances as well as the expansion rate of the universe.

The Big Bang Nucleosynthesis (BBN) describes the production of very light

nuclei during the early phases of the universe, namely deuterium, tritium, helium, beryllium and lithium. The predicted abundances of such light atoms exactly match the data as long as atoms are only 4-5% of the total constituents of the universe [33]. Both type Ia supernovae measurements of the universe expansion rate as well as the primordial nucleosynthesis abundances are fundamental confirmation of the  $\Lambda$ CDM model and thus indirect evidence of dark matter existence.

The last very important piece of evidence for dark matter is the existence of structures. After the expansion consequent to the Big Bang, the universe was mostly uniform and so extremely hot and dense that structure formation was not possible. As the universe expanded radiation and matter both diluted and so did their energy densities. Since the energy density in radiation dies away more quickly, matter overtook radiation as the leading contributor to the universe's energy and expansion. Only at this point small compact structures could begin to grow from slightly denser regions. Radiation in fact would have washed out perturbation while matter could slow down and clump together. Exclusively slowly-moving matter collapses sufficiently to form structures and that is the reason why the standard cosmological model considers a "cold" dark matter: not hot and relativistic. Two compelling forces were present during the structure growth: gravity, that was pushing matter in, and radiation, that was pulling it out. Because of its immunity to radiation and because of its greater abundance, dark matter was the major contributor to the attractive potential wells, really causing the collapse into structures. Without dark matter in fact galaxy formation would have occurred substantially later because of the dynamical equilibrium between gravity and radiation pressure. This would have led to a universe completely different with respect to the one in which we live. With the universe expansion under-dense regions expand more rapidly while over-dense regions expand more slowly. The result is depleted regions always growing and high density regions reduced to filaments. When the filaments intersect, nodes with extremely high density forms giving birth to the so called cosmic web. The nodes seed the formation of galaxies and this process continue over time: structures form and patterns repeat on increasingly larger scales. Numerical simulations confirm these predictions on the largest scales, with dark matter correctly accounting for the density and shape of structure in the Universe. Moreover in the last few years the cosmic web has been observed using the light of double quasars [34–36]. Cosmic web and structure formation again confirm the  $\Lambda$ CDM model and the existence of dark matter, without which structures as well as the universe as we know it, could not have been possible.

## 1.2 Models and candidates

Thanks to the many and different evidences collected to now the scientific community in general accepts the existence of dark matter. Nevertheless there are

lots of alternative hypothesis that aim to explain the observed phenomena commonly referred to as “evidence of dark matter” without invoking supplemental non-baryonic matter [37]. The most common method is to modify the general relativity and the best-known theories of this class are called MOND from Modified Newtonian Dynamics [38–40]. Despite all the efforts, they have not yet succeeded in explaining with a unique model all the “dark matter evidences” as the latter involve very different phenomena. Such theories are mentioned for completeness but they are largely beyond the object of this work.

All the evidence collected in the last decades have revealed the existence of this unknown matter but apart from that, only very general information regarding its nature are available:

1. the average energy density in the cosmos from the CMB anisotropies
2. the nearby density from galaxies rotation curves
3. it is cold, i.e. not relativistic, from structure formation
4. it interacts at most extremely weakly from the shape of the Bullet Cluster as well as from the lack of direct evidence despite the huge efforts
5. it is electrically neutral from its “darkness”

Despite all the constraints listed above, it is still possible to build a lot of different dark matter models and a plethora of dark matter candidates has been proposed during the last decades. Particle dark matter model building has been strongly influenced by the quest to extend the Standard Model of particle physics. For this reason two main strategies have been adopted: looking for DM candidates that could at the same time solve some open issues in particle physics or creating ad hoc models to explain an eventual experimental or observational signal. Nevertheless, only a direct dark matter detection can provide definitive information on the nature of the particle. Presenting the huge variety of all these candidates goes well beyond the purpose of this work. Therefore, only few classes of candidates deriving from the most developed models are briefly presented here with a preference for light dark matter candidates as CRESST is the leading experiment for such mass regions.

**WIMPs** One of the most popular and appealing class of candidates for Cold Dark Matter (CDM) is represented by WIMPs, the acronym of Weakly Interacting Massive Particles. The term “weakly” does not refer to the weak nuclear force as WIMPs are supposed to interact with baryonic matter even more weakly than neutrinos. For the production mechanism the standard scenario assumes WIMPs were in thermal equilibrium with all the other particles in the early universe. At temperatures much higher than the WIMP mass, both their self-annihilation into standard model particles and their pair production from the plasma were possible. During universe expansion, the temperature of the plasma became smaller than the WIMP mass and the WIMP pair production was no more possible. On the contrary the annihilation process could continue and the abundance of WIMPs decreased. At the same time the universe expansion caused a reduction of WIMP numerical density and thus a reduction of its annihilation rate. When the expansion rate of the universe became higher than the WIMPs annihilation

rate, WIMPs annihilation ceased and their number density in a comoving volume remained approximately constant. In this hypothesis the present relic density of WIMPs is calculated to be approximately:

$$\Omega_\chi h^2 \approx \frac{3 \times 10^{-27} \text{ cm}^3 \text{ s}^{-1}}{\langle \sigma_{ann} v \rangle} \quad (1.2)$$

where  $\Omega_\chi h^2$  is the physical density of dark matter,  $\sigma_{ann}$  is the WIMP annihilation cross-section,  $v$  the relative velocity of the annihilating WIMPs and the angle brackets denote the average over the WIMP thermal distribution. Since Planck measured  $\Omega_\chi h^2 \simeq 0.12$  [32] and  $v \sim c/1000$  is commonly used for cold dark matter, the annihilation cross-section required to achieve the appropriate relic density is of the same order of magnitude of a typical weak interaction process. Moreover the reason why WIMPs became so popular is that they arise naturally when trying to extend the Standard Model of particle physics to embed it in a more fundamental theory. An example of framework containing a paradigmatic WIMP is the minimal supersymmetric extension to the Standard Model if the lightest supersymmetric particle is a neutralino. Under some conditions, in fact, the lightest supersymmetric particle (LSP) would be a good candidate for cold dark matter. Over the past two decades a myriad of different theories have been proposed, from the early proposals of supersymmetry and technicolour to the more recent ideas of large and warped dimensions and Little Higgs [41] [42].

**Asymmetric dark matter** Another class of dark matter relic is called asymmetric dark matter (ADM). The motivation for this models comes from the observation that the present-day mass density of DM is about a factor of five higher than the density of baryonic matter [32, 43]:

$$\Omega_{dm} h^2 \simeq 5 \Omega_b h^2 \quad (1.3)$$

where  $\Omega_{dm} h^2$  and  $\Omega_b h^2$  are the physical densities of dark matter and baryonic matter respectively. In the standard WIMP paradigm DM is a thermal, non-relativistic relic particle (usually self-conjugate) with mass in the GeV-TeV range that decouples when its weak-scale annihilations fall out of equilibrium due to the Boltzmann suppression of the WIMP population. The similarity of the dark matter and baryonic matter densities then must be taken to be a coincidence, at least in most of the WIMP scenarios. Alternately, the similarity in these observed densities can suggest a common origin, some kind of a unification or strong connection between the physics and cosmological evolution of baryonic and dark matter. The basic idea of ADM is that the dark matter particle is distinct from the anti-particle and the current abundance arises almost entirely from one species as in the baryonic sector (conventionally taken as the particle). A variety of mechanisms have been suggested for generating the asymmetry between baryonic matter and anti-matter. If the same mechanism also generates the asymmetry between dark matter and dark anti-matter, then the number density of dark matter should be simply related to the baryonic number density.

The observed relation of equation 1.3 then requires the DM particle mass to be typically, though not exclusively, in the 1-15 GeV regime, with the precise figure depending on details of the model [44]. Such light dark matter candidates lie in the mass range in which CRESST is the leading experiment. The idea that the DM and baryon asymmetries might be related to each other dates almost from the time of the WIMP paradigm itself [45, 46]. In the last several years, Asymmetric Dark Matter has become a flourishing subfield of DM research and this is driven in part by a purely theoretical motivation to explore well-motivated models outside the standard WIMP parameter space, and in part by anomalies in Direct and Indirect Detection. For recent reviews of asymmetric dark matter, see Refs. [44, 47, 48].

**Axions and axion-like-particles** An additional class of DM candidates present in the panorama since several decades is represented by axions and axion-like-particles (ALPs). Axions resulted from the symmetry breaking in the solution of the strong CP problem proposed in 1977 by Peccei and Quinn [49, 50]. According to the current mathematical formulation of quantum chromodynamics (QCD), a violation of CP-symmetry in strong interactions could occur. However, no violation of the CP-symmetry has ever been seen in any experiment involving only the strong interaction. As there is no known reason in QCD for it to necessarily be conserved, this is a “fine tuning” problem known as the strong CP problem. Axions and ALPs are an especially compelling example of a broad category of DM candidates encompassing very light particles, arisen from very light scalar or pseudoscalar fields, and extremely weak interactions. The mass range relevant for axion dark matter is very wide  $10^{-6} \lesssim m_a[\mu eV] \lesssim 10^3$  [51] and this generally implies the imprint of quantum effects on macroscopic scales [41]. Moreover they are expected to be extremely weakly interacting with ordinary particles, which implies that they were not in thermal equilibrium in the early universe. For recent review of axions and axion-like particle see Ref. [41].

**Sterile neutrinos** The only Standard Model (SM) particle that may qualify to be a candidate for dark matter is the neutrino. Unfortunately the estimated neutrino relic density is too small in comparison to the dark matter relic density obtained from the CMB measurements. An estimate of the neutrino relic density is obtained as

$$\Omega_\nu h^2 = \sum_{i=0}^3 \frac{m_{\nu_i}}{93.14 eV} \quad (1.4)$$

The 2018 Planck results [32] show an upper limit for the sum of neutrino masses  $m_\nu$  equal to 0.12 eV. The same data provided a measured dark matter energy density of  $\sim 0.12$ . From these measured quantities it is clear that neutrinos cannot account for the dark matter content of the Universe as the neutrino relic energy density is too small with respect to the dark matter one. According to the Standard Model of particle physics, neutrinos are massless as a consequence of the requirements of gauge invariance and renormalizability of the theory and the three different leptonic numbers associated with the three flavours, are separately conserved. At the same time there are several pieces of evidence that neutrinos

have tiny but non-zero masses and that neutrinos of different flavours mix with each other. For a review see Ref. [52]. One of the most appreciated possible solutions for the neutrino mass problem is the introduction of the so called “sterile neutrinos”. Sterile neutrinos (or inert neutrinos) are hypothetical particles that interact only via gravity and do not interact via any of the fundamental interactions of the Standard Model. The term sterile neutrino is used to distinguish them from the known active neutrinos in the Standard Model, which are charged under the weak interaction. Some times this term is referred to right-handed neutrinos whose mass is unknown and could have any value between  $10^{15}$  GeV and less than 1 eV [53]. Among various non-baryonic dark matter models, sterile neutrinos are also assumed to be viable candidates to address the dark matter problem in the Universe. The simplest model including sterile neutrinos assumes the presence of a single generation of right-handed neutrino to serve as a dark matter candidate. Sterile neutrinos with masses  $\sim 100$  eV can serve as both warm and cold dark matter candidates [54, 55]. Light neutrinos are disfavored as dark matter candidates due to considerations on the structure formation in the early universe: simulations show they are too hot to allow a proper structure formation in agreement with the observed data. They can at best account for a few percent of the observed dark matter. On the other hand the heavy sterile right-handed neutrinos are a possible candidate for a dark matter WIMP [56].

### 1.3 The inelastic dark matter framework

The most common kinetic framework used for the dark matter interaction consider an elastic scattering to happen between dark matter and the target nucleus. Another possible framework is the inelastic one: dark matter scatters off nuclei into an excited state  $\chi^*$  with a certain mass splitting  $\delta = m_{\chi^*} - m_{\chi}$ . The inelastic dark matter (iDM) was first proposed implicitly at the end of 90s [57] and is well known by that time [58–62]. Nonetheless, it was widely used only to explain DAMA/LIBRA annual modulation reconciling it with the results of the other experiments [58, 59, 62–65]. Despite the numerous attempts, it is now extremely difficult to conciliate DAMA/LIBRA annual modulation with current data from several different experiments with the iDM interpretation [1]. Nevertheless, the iDM is a worthy hypothesis by itself and it is important to include it in the possible dark matter interactions. The kinematics and rate in the iDM framework are presented in sections 1.3.2 and 1.3.3 respectively, following the result of [1]. Currently inelastic mass splittings are predicted in many of well-motivated dark matter models. In Ref. [1] three models are considered as example: the Higgsino, the magnetic inelastic dark matter and dark photons mediated dark matter. For other iDM models see Ref. [60].

### 1.3.1 iDM interaction

The case that is of particular interest for this work is when only inelastic scattering of dark matter takes place. As it will be discussed in the following subsections, the kinematic phase space of the iDM is a subset of the elastic interaction one and the rate of the inelastic scattering is strongly suppressed with respect to the elastic one. As a consequence of this, it is clear that performing an iDM analysis is interesting only in case of a dark matter interacting purely inelastically. If the elastic process is possible, it would completely dominate over the inelastic spectrum. This scenario can be a consequence of the presence of a new interaction as explored in different models [58, 59, 63, 66]. In this models the DM interaction is obtained via a vertex of the type  $\chi\chi^*B$  where  $\chi$  is the dark matter particle ground state,  $\chi^*$  the dark matter particle excited state, and  $B$  is the new mediator, while the vertex  $\chi\chi B$  does not exist.

A relevant consequence of this scenario it that the predicted spectrum is characterised by high recoil energies and very different spectra are expected for different mass splittings and target materials. As it will be described in the following, CRESST detectors play a crucial role in this search thanks to Tungsten as it allows to probe a mass splitting range as wide as possible at present time. From now on, if not differently specified, all the events surviving the selection procedure will be treated as candidate of iDM.

### 1.3.2 Kinematics of iDM

Let's consider a dark matter particle with mass  $m_\chi$  and a kinetic energy  $E_0 = \frac{1}{2}m_\chi v^2$ , where  $v$  is the velocity in the laboratory frame. In the hypothesis of mass splitting  $\delta \ll m_\chi$  and in the non-relativistic limit the recoil energy is:

$$E_R = \frac{\mu}{m_N} \left[ (\mu v^2 \cos^2 \theta_{lab} - \delta) \pm (\mu v^2 \cos^2 \theta_{lab})^{1/2} (\mu v^2 \cos^2 \theta_{lab} - 2\delta)^{1/2} \right] \quad (1.5)$$

where  $\theta_{lab}$  is the scattering angle in the laboratory frame,  $m_N$  is the nucleus mass and  $\mu$  is the reduced mass of the system [dark matter particle - nucleus target].

In figure 1.4 the kinematically allowed space of recoil energies for different target materials as a function of velocity for a dark matter mass  $m_\chi = 1\text{TeV}$  and several mass splittings. The two branches present in each plot correspond to the two solutions of equation 1.5 while contours correspond to maximal scattering angle  $\cos^2(\theta) = 1$ . From this plot two main features of the inelastic scattering can be appreciated:

1. A minimum velocity does exist that depends on the mass splitting and below which the inelastic scattering cannot happen. This feature is due to the kinematics of the inelastic process: the initial kinetic energy has to be sufficiently high in order to access to the excited state of the DM particle.
2. The presence of a minimum velocity implies the existence of a minimum recoil energy but the inelastic scattering kinematics lead to a recoil energy

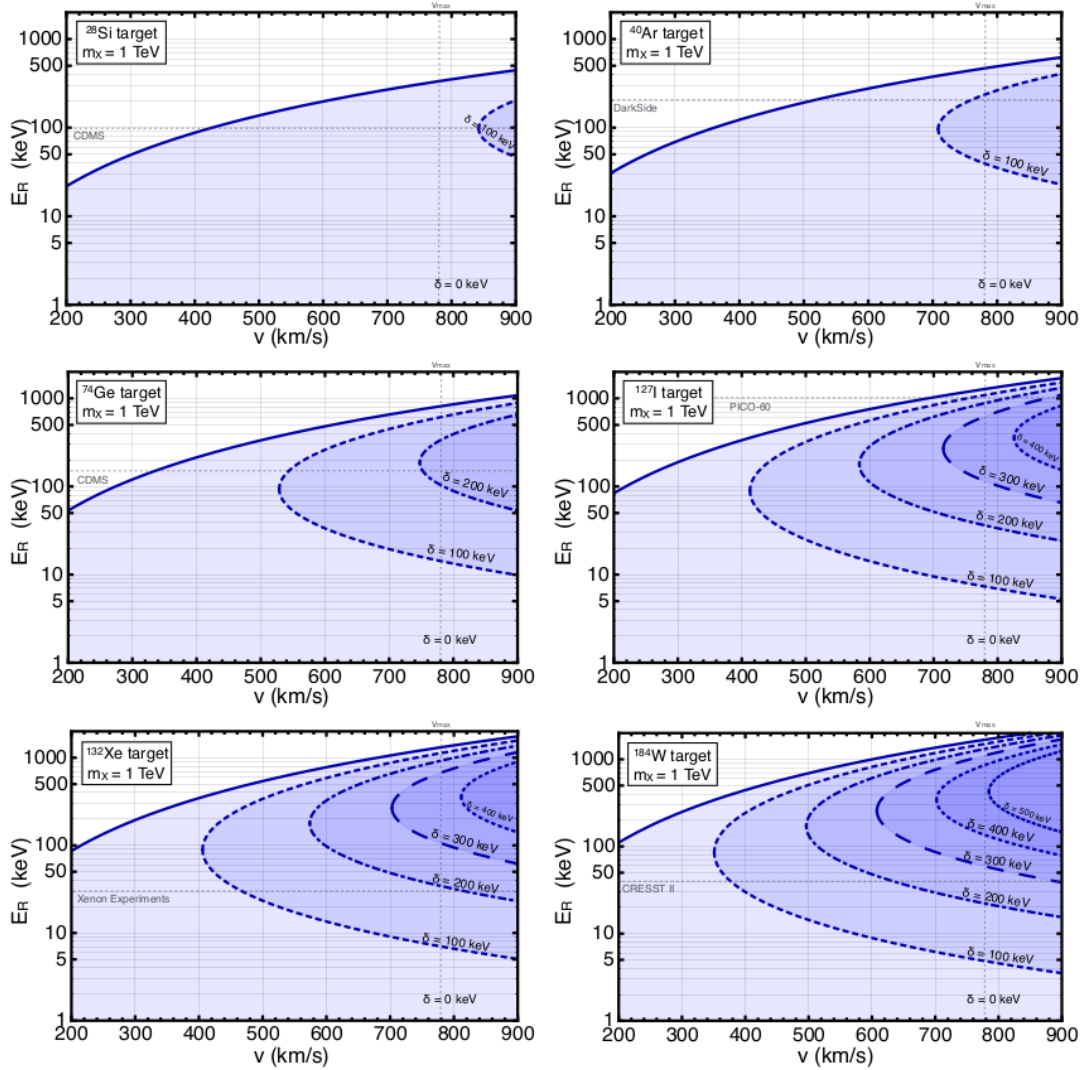


Figure 1.4: Kinematically allowed space of recoil energies as a function of the incoming dark matter velocity (shaded region) for different target materials and a dark matter mass  $m_\chi = 1 \text{ TeV}$ . The contours indicate the mass splitting:  $\delta = 0$  in solid and  $\delta = 100, 200, 300, 400, 500$  keV in dashed, dotted-dashed, dotted, long-dashed and fine dotted respectively. The dashed gray horizontal line indicate the maximum recoil energy window used by the considered collaborations. The maximum incoming terrestrial dark matter speed is expected to be  $780^{+54}_{-41} \text{ km/s}$  [67] and it is indicated with a gray dashed vertical line. Figure taken from [1].

with both a lower and an upper bound for a fixed incoming terrestrial dark matter speed.

Two considerations, crucial for direct detection experiments<sup>2</sup>, can be made in light of these features. Firstly, having a minimum velocity reduces the available kinematic phase space of the DM-nuclear scattering and thus the effective rate is suppressed. The fraction of dark matter in the galactic halo that has a velocity higher than the minimum one will determine the amount of suppression of the effective rate. Secondly, the recoil energy with both a lower and an upper bound can in principle make it extremely difficult for a traditional direct detection experiment to find inelastic dark matter. One of the major efforts of the last decades in direct dark matter searches has been to optimize the sensitivity to the elastic DM-nuclei scattering, and this was done pushing the observed recoil energy window as low as possible. For inelastic dark matter though this can make the experiment insensitive to detect it if the minimum inelastic recoil energy is higher than the window of recoil energies considered by the analysis. The minimum velocity to allow the scattering at any recoil energy correspond to the apex of the parabola:

$$v_{\min}^{apex} = \sqrt{\frac{2\delta}{\mu}} \quad (1.6)$$

and the relative recoil energy is done by:

$$E_R(v_{\min}^{apex}) = \frac{\mu}{m_N} \delta. \quad (1.7)$$

The general expression of the minimum velocity as a function of the recoil energy is:

$$v_{\min} = \frac{1}{\sqrt{2E_R m_N}} \left( \frac{E_R m_N}{\mu} + \delta \right) \quad (1.8)$$

and it is valid up to corrections of  $\mathcal{O}(E_0/m_X, \delta/m_x)$ , negligible for fixed terrestrial experiments and  $m_X \gg 1$  GeV. Using the simple expressions for the apex of the parabola, it is possible to understand qualitatively how the kinematic phase space can change depending on the target mass and both the dark matter mass and splitting. If the mass splitting  $\delta$  goes to zero, the elastic scattering phase space is obtained. If instead the mass splitting is at least of few hundred keV the features of the inelastic kinematics become predominant and two different cases can be considered. For a heavy dark matter  $m_X \gg m_N$ , thus  $\mu \simeq m_N$  and therefore  $v_{\min}^{apex} \simeq \sqrt{2\delta/m_N}$  and  $E_R(v_{\min}^{apex}) \simeq \delta$ . Consequently experiments with light target will have low sensitivity for inelastic dark matter due to the high minimum velocity necessary to make the excited dark matter state accessible. Moreover, because the recoil energy is proportional only to the mass splitting, the experiments' sensitivity will in general depend only of the energy interval considered for the analysis as shown with the gray horizontal line in figure 1.4. On the

<sup>2</sup>A brief overview of experimental methods for dark matter search is presented in section 1.4.

other hand for a light dark matter  $m_X \ll m_N$ ,  $\mu \simeq m_X$  and so  $v_{min}^{apex} \simeq \sqrt{2\delta/m_X}$  and  $E_R(v_{min}^{apex}) \simeq \delta m_X/m_N$ . In this case, a very high incoming velocity is needed to access even low mass splittings. With lower velocities only light dark matter with very low  $\delta$  will undergo inelastic scattering but the kinematics of the process will be quite similar to the elastic case. For this reason the “frontier” of inelastic dark matter corresponds to heavy dark matter, that can be tested only by experiments with a heavy target material (see section 1.4) [1].

### 1.3.3 Rate in the iDM framework

The rate of DM scattering for a given recoil energy  $E_R$  in a detector with  $N_T$  scattering targets per unit mass is given by:

$$\frac{dR}{dE_R dM} = n_X N_T \int_{v_{min}}^{v_{max}} v f(\vec{v}, \vec{v}_e) \frac{d\sigma}{dE_R} d^3v, \quad (1.9)$$

where  $n_X = \rho_X/m_X$  is the local dark matter number density,  $\vec{v}$  and  $\vec{v}_e$  are the dark matter and Earth’s velocity in the Galactic rest frame respectively,  $v_{min}$  is the minimum dark matter velocity needed for the inelastic scattering to happen (eq. 1.8) and  $v_{max}$  is the maximum velocity of the incoming dark matter in the laboratory rest frame,  $f(\vec{v}, \vec{v}_e)$  is the dark matter velocity distribution and finally  $d\sigma/dE_r$  is the differential cross-section for dark matter scattering off a nucleus. Before discussing the result of this integral, a brief but more detailed discussion of the velocity distribution and the differential cross-section will be presented following the outline of [1].

#### Velocity distribution

For the study presented in Ref. [1] the dark matter velocity distribution was considered to be a Maxwellian distribution with a sharp cutoff at the escape velocity<sup>3</sup>:

$$f(\vec{v}, \vec{v}_e) = \frac{e^{-(v^2+v_e^2+2v v_e \cos \theta)/v_0^2}}{N(v_0, v_{esc})} \quad (1.10)$$

where  $\theta$  is the angle between Earth’s and dark matter’s velocity in the Galactic rest frame and  $N(v_0, v_{esc})$  is the normalization factor that depends on the characteristic dark matter velocity  $v_0$  and the escape velocity  $v_{esc}$ . From the integral  $\int_0^{v_{max}} f(\vec{v}, \vec{v}_e) = 1$  the normalization factor can be obtained:

$$N(v_0, v_{esc}) = \pi^{3/2} v_0^3 \left( \text{erf} \left( \frac{v_{esc}}{v_0} \right) - \frac{2v_{esc}}{\pi^{1/2}v_0} e^{-\frac{v_{esc}^2}{v_0^2}} \right). \quad (1.11)$$

The Earth’s velocity around the Sun can be described by:

$$v_e = \left[ 232 + 15 \cos \frac{2\pi(t - 152\text{days})}{365\text{days}} \right] \text{ km/s} \quad (1.12)$$

<sup>3</sup>The escape velocity is the minimum speed needed for a free object to escape from the gravitational influence of a massive body.

where  $t$  indicates the day of the year, from the 1st of January ( $t = 0$ ) to the 31st of December ( $t = 365$ ). The maximum velocity of incoming dark matter is given by the difference of the escape velocity and the Earth's velocity:  $\vec{v}_{max} = \vec{v}_{esc} - \vec{v}_e$ . For finite  $v_{esc}$ , the velocity integral depends on the value of  $v_{min}$  that is more precisely on the relative order of  $v_{min}$  and  $v_{esc} - v_e$ :

$$\begin{aligned} \int_{v_{min}}^{v_{max}} d^3v &= \int_{v_{min}}^{v_{max}} \int_{-1}^1 \int_0^{2\pi} v^2 dv d\cos\theta d\phi = \\ &= 2\pi \begin{cases} \int_{v_{min}}^{v_{esc}-v_e} v^2 dv \int_{-1}^1 d\cos\theta + \int_{v_{esc}-v_e}^{v_{esc}+v_e} v^2 dv \int_{-1}^{c^*} d\cos\theta & v_{min} < v_{esc} - v_e \\ \int_{v_{min}}^{v_{esc}+v_e} v^2 dv \int_{-1}^{c^*} d\cos\theta & v_{esc} - v_e < v_{min} < v_{esc} + v_e \end{cases} \end{aligned} \quad (1.13)$$

where  $c^* = \cos\theta^* = (v_{esc}^2 - v^2 - v_e^2)/(2vv_e)$  is the minimum angle possible for the scattering when  $v_{esc} - v_e < v_{min} < v_{esc} + v_e$ . Considering that the Earth's velocity change during the year according to equation 1.12, the limits of the integral will change consequently leading to some dramatic features for the inelastic scenarios. In case of a high  $v_{min}$  it could happen that the scattering occurs only during some short period of the year.

### Differential cross-section

For simplicity let's consider the differential cross-section  $d\sigma/dE_R$  to be spin independent and dependent on the recoil energy only through the nuclear form factor  $F(E_R)$ :

$$\frac{d\sigma}{dE_R} = \frac{\sigma_n m_N [Zf_p + (A - Z)f_n]^2}{v^2 2\mu_n^2 f_n^2} F^2(E_R) \quad (1.14)$$

where  $\sigma_n$  and  $\mu_n$  are the dark matter-nucleon scattering cross-section and reduced mass,  $A$  and  $Z$  are the nuclear atomic mass and number of the target material, and  $f_p$  and  $f_n$  contain the DM-proton and DM-neutron effective couplings respectively. In this hypothesis the correct calculation of the nuclear form factor energy dependence is crucial in order to have a reliable expected spectrum to be compared with experimental data. In fact, the nuclear form factor accounts for the internal structures of the target nucleus that cannot be neglected for high momentum transfers. Thus the nuclear form factor critically determines the spectrum of the recoil nuclei. There are various models used to describe the nuclear form factor. One of the most used is the Helm form factor which is an analytic expression of the nuclear form factor dependence on the energy. In the last year, numerical models have been used often to obtain a better description, more accurate because it is applied to a specific nucleus. Whenever possible, using such recent calculations is preferable of course.

The goal of this work is to search for inelastic dark matter signals in the CRESST experiment (see chapter 2). For this reason the expected spectrum

for Tungsten will be explicitly discussed in the following. For more detailed information we refer to [1].

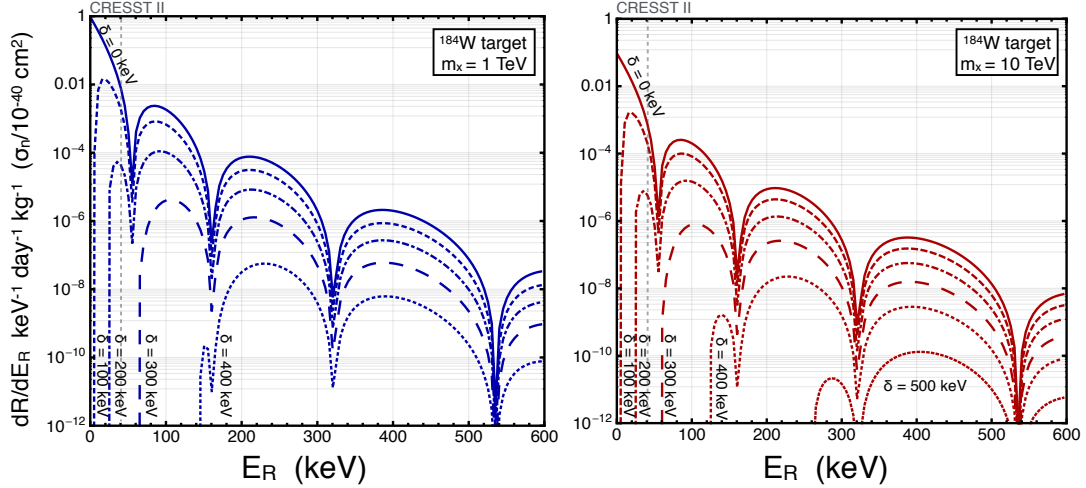


Figure 1.5: Recoil rate per unit of mass and energy for two different dark matter mass values:  $m_X = 1$  TeV on the left (blue plot) and  $m_X = 10$  TeV on the right (red plot). A target made purely of  $^{184}\text{W}$  has been considered together with a DM-nucleon cross-section  $\sigma_n = 10^{-40}\text{cm}^2$ . The spectrum for some mass splittings is presented with different line style. The vertical gray line represents the maximum recoil energy employed in CRESST-II analysis [3]. Figure taken from [1].

In the hypothesis of equal coupling of dark matter with protons and neutrons ( $f_p = f_n$ ) the differential cross-section become:

$$\frac{d\sigma}{dE_R} = \frac{\sigma_n m_N}{v^2 2\mu_n^2} A^2 F^2(E_R). \quad (1.15)$$

In absence of specific calculation for Tungsten, the Helm form factor has been used:

$$F_h^2(E_R) = \left( \frac{3j_1(qr/\hbar)}{qr/\hbar} \right)^2 e^{-s^2 q^2/\hbar^2} \quad (1.16)$$

where  $q = \sqrt{2E_R m_N}$ ,  $r = \sqrt{r_n^2 - 5s^2}$ ,  $s = 1$  fm, and  $r_n = A^{1/3}$  fm.

Regarding the velocities the following values have been used:  $v_{esc} = 533$  km/s,  $v_0 = 220$  km/s and  $v_e = 232$  km/s. Finally a DM density of  $0.3 \text{ GeV}/\text{cm}^3$  and a cross-section  $\sim 10^{-40} \text{ cm}^2$  are assumed. The recoil rate per unit of mass and energy is shown in figure 1.5 for two different dark matter masses, 1 TeV and 10 TeV and several values of mass splittings. The derivation of such expected spectra can be found in appendix A.

The trends shown in figure 1.4 become manifest in the expected spectra of figure 1.5. The available phase space as well as the event rate become smaller with

increasing  $\delta$  and also the optimal recoil energy for inelastic dark matter search increases with higher mass splittings. The nuclear form factor is responsible for the steep abatement of the event rate. Finally, from the comparison of left and right plot, it is clear that larger reduced mass makes higher mass splittings accessible. Heavy nuclei are more effective in setting constraints on highly inelastic DM. For this reason a new analysis of CRESST data will explore the inelastic frontier exploiting the presence of Tungsten in the target.

## 1.4 Detection of WIMPs

There is a large number and variety of experiments aimed to detect dark matter and they can be roughly classified in colliders and accelerators searches and direct and indirect detection experiments.

### Colliders and accelerators searches

Various DM searches have been carried out by the CMS and ATLAS collaborations at the LHC in pp collisions [68–72]. The basic assumption in this type of detection is that dark matter particles are naturally produced during interaction of particles beams. Then the expected detection is that dark matter particles escape the detector without interacting and thus leading to significant amounts of missing energy and momentum. There is a wide assortment of DM models that have been targeted and at the same time there is a big variety of possible DM signals. However no signal for DM has been observed in the LHC experiments so far. Instead, limits have been set on masses, couplings and cross-sections. Finally it is important to note that collider searches can indeed discover new particles but they cannot prove such particles are dark matter. Nevertheless they can provide precious information to direct and indirect detection experiments. At the same time accelerator and collider searches can benefit from information and constrains obtained with direct and indirect experiments as well as CMB measurements.

### Indirect detection

Indirect DM detection refers to the search of annihilation or decay products of DM particles resulting in detectable species, especially gamma rays, neutrinos and antimatter particles. The implicit assumption if searching for annihilation signatures is that both dark matter particles and anti-particles are present inside the halo with a reasonable ratio. In fact, in first approximation the less abundant specie is the one determining the number of annihilation processes that can take place. Gamma ray emission from DM annihilation can be produced in lots of astrophysical objects in principle but some of them have been preferred to maximize the signal to noise ratio: dwarf spheroidal galaxies, and the inner region of the Milky Way. Observations with the Fermi Large Area Telescope (LAT) as well as ground-based facilities have provided an unprecedented picture

of the gamma-ray sky ideally suited to look for a signal from DM annihilation or decay for DM particles from a few GeV mass up to several TeV. Standard model particles can be produced in DM annihilation processes if enough DM accumulates inside a celestial body. Such particles can heat up the body or escape from it. In both cases constraints can be put on DM particle properties. Also the cosmic radiation is populated by stable charged particle that can be produced by DM annihilation or decay. To maximise the signal to noise ratio, this searches focus on relatively rare species such as positrons, antiprotons and antinuclei. A complete review can be found in Ref. [41].

## Direct detection

The basic hypothesis behind the direct detection experiments is that DM particles interacts (weakly) with atomic nuclei or with electrons in the detector material. Under this assumption, direct detection experiments aim to observe the nuclear/electron recoil due to elastic or inelastic scattering of Galactic DM particles. The elastic dark matter rate is presented in subsection 1.4.1 while a list of the main experimental approaches for DM direct detection is described in subsection 1.4.2.

### 1.4.1 Elastic dark matter rate

For DM scattering off nuclei, the differential scattering rate  $R$  as a function of the nuclear recoil energy  $E_R$  has the form:

$$\frac{dR}{dE_R dM} = n_X N_T \int_{v>v_{min}} v f(\vec{v}, \vec{v}_e) \frac{d\sigma}{dE_R} d^3v, \quad (1.17)$$

with the same variables of equation 1.9. The inelastic case has been already discussed in section 1.3. Because of the kinematics of the elastic process there is no minimum velocity needed for the scattering to happen. The minimal velocity able to induce a recoil energy  $E_R$  is given by:

$$v_{min} = \sqrt{\frac{E_R m_N}{2 \mu^2}}. \quad (1.18)$$

The shape of the expected energy spectrum resulting from elastic scattering of DM particles off nuclei in a detector is exponentially rising towards lower energies without any particular feature and depends on the masses of both the DM particle and the target nucleus. Because of this a multi-element target can provide tighter constraints on the DM mass.

The expected energy spectrum for elastic scattering off  $\text{CaWO}_4$  is shown in figure 1.6 for a dark matter mass of  $1 \text{ TeV}/c^2$ . The colored lines correspond to the rate of the individual target elements weighted according to their mass fraction in  $\text{CaWO}_4$ . The sum of the individual rates gives the black line spectrum. In figure 1.7 the Helm form factor as a function of the recoil energy is shown

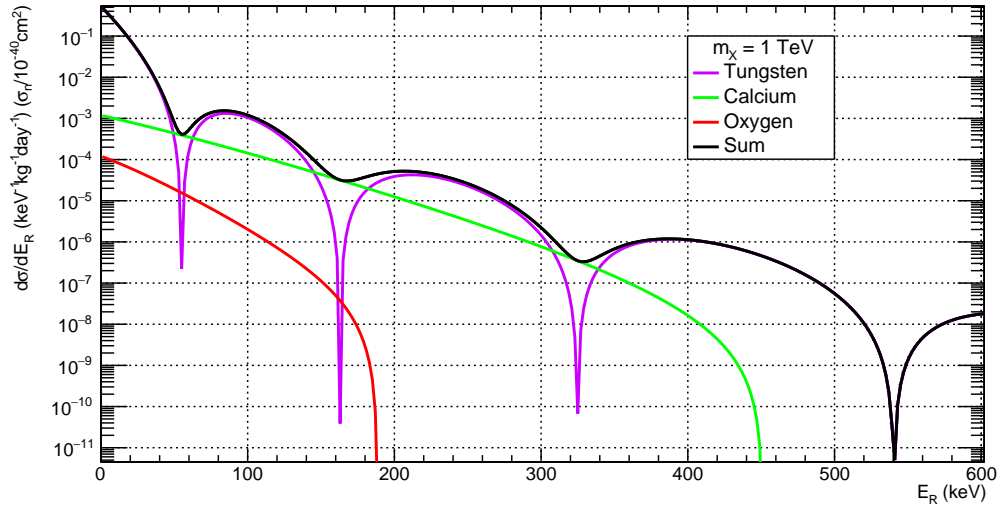


Figure 1.6: Expected energy spectrum for 1 TeV DM particle elastic scattering off  $\text{CaWO}_4$ . The colored lines represent the contributes of the single elements weighted according to their mass fraction: Tungsten in violet, calcium in green and oxygen in red. The black line correspond to the total expected spectrum, obtained as the sum of the constituents elements spectra.

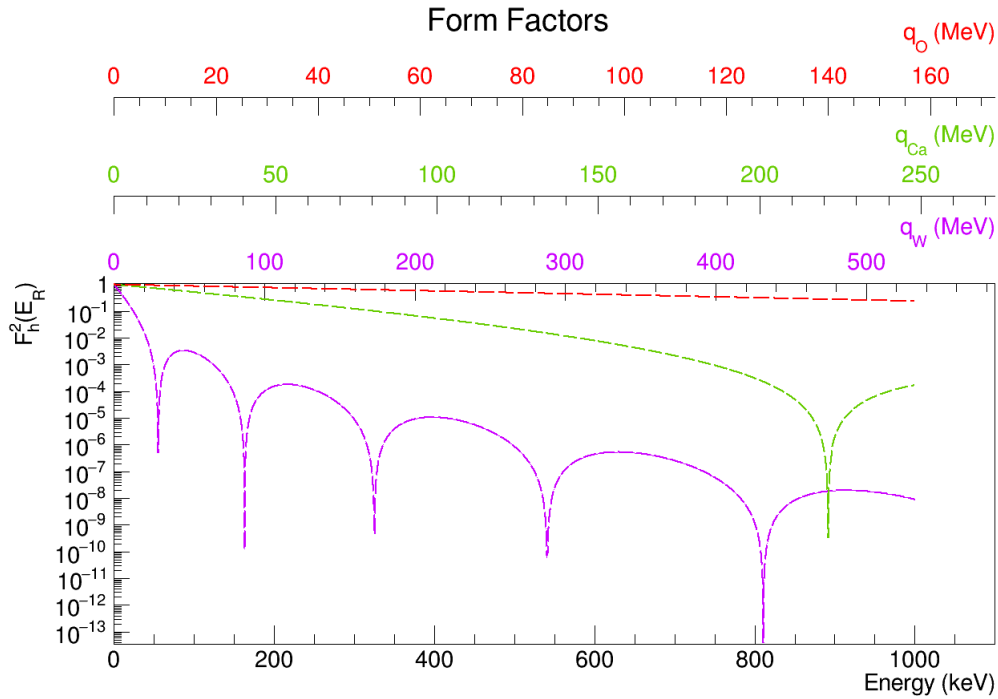


Figure 1.7: Helm form factors as a function of the recoil energy (bottom x axis) for Tungsten, Calcium and Oxygen in violet, green and red respectively. The top x-axes show the corresponding momentum transfer to the three nuclei in case of scattering. Label and title of the axes have the same color legend of the plot in figure 1.6.

with the same color legend of figure 1.6. The three x-axes on the top show the corresponding momentum transfer to the three nucleus in case of scattering. As briefly discussed in subsection 1.3.3, at low energies the effect of the form factor is negligible and the spectrum is dominated by Tungsten because of its high mass: in equation 1.15 the differential cross-section depends on  $A^2$  in the hypothesis of equal coupling of DM with protons and neutrons. Moving to higher energies the form factors cause a steep drop in the rate and the strongest effect is due to Tungsten because of its form factor zeros. The rate due to the scattering off calcium and oxygen is no more present for energies higher than  $\sim 450$  keV and  $\sim 200$  keV respectively because of the maximum incoming dark matter velocity. Using equation 1.5 with  $\delta = 0$ ,  $v = 780$  km/s and  $\cos \theta_{lab} = 1$ , the maximum recoil energy for an elastic scattering can be obtained. The maximum recoil energy for scattering off Calcium is  $\sim 500$  keV while for scattering off Oxygen is  $\sim 200$  keV. Considering these values of the maximum recoil energy, it is clear that only the scattering off Tungsten can contribute to the recoil energy spectrum for higher energies while the sharp drop off present in the expected rate of Calcium and Oxygen is due to the DM velocity distribution and the kinematic of the process and not to the form factor.

Before moving to the experimental approaches there is an important feature of the DM rate that has to be briefly discussed: the annual modulation. As already discussed in the inelastic scattering (see subsection 1.3.2) the DM velocity distribution depends on both DM's and Earth's velocities. The initial kinetic energy of the incoming DM particle depends on the relative velocity between the DM particle and the detector. The Earth's motion around the Sun change this relative velocity during the year inducing a seasonal variation of the total event rate depending on whether the two velocities are maximally or minimally combined. A schematic picture of the velocity composition is shown in figure 1.8.

In the standard halo model the annual modulation has a fixed period of 1 year<sup>4</sup> and the two speeds add up maximally at the beginning of June [33]. However these values depends on the DM distribution in the halo as well as on the recoil energy.

### 1.4.2 Experimental approaches for direct dark matter searches

Since the incoming particle velocity is  $v/c \sim 10^{-3}$  the nuclear recoil energy is in the 0.1-100 keV range for DM masses from 100 GeV down to 1 GeV. For smaller DM masses, in the sub-GeV scale, the recoil energy would be below threshold for most of the experiments based on the detection of DM-nucleus scattering. To investigate this range of possible DM masses a better strategy is to search for DM scattering off bound electrons. For information about this class of experiments

---

<sup>4</sup>The density and intrinsic velocity distribution will change as the Solar System moves through substructures present in the galaxy. This results in variations in the recoil rate but, as the time scales involved are many orders of magnitude longer than a year, such temporal variation are neglected.

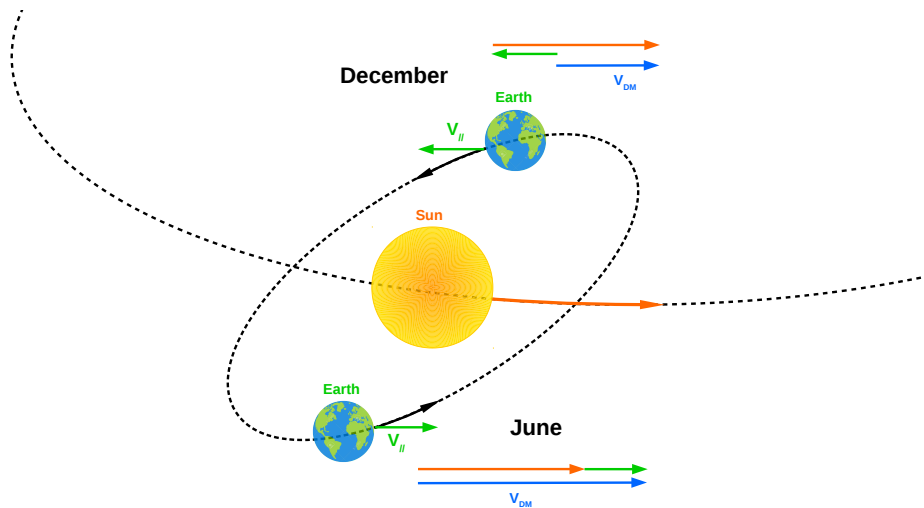


Figure 1.8: Schematic picture of the Earth motion around the Sun as well as the Sun motion around the galactic center. The composition of this two velocities give rise to the DM annual modulation rate.

we refer to [73] [41]. Focusing on the GeV-scale DM masses, a brief overview of the experimental techniques for direct detection follows.

All the direct detection experiments are designed to detect the small and rare signals due to DM interaction in the detector. The typical rates they have to deal with is evident from the expected energy spectrum of figure 1.6. Because of the low rate, the suppression of all the possible background is crucial. The cosmic and environmental radiation are abated by going deep underground and surrounding the experimental setup with shielding structures. Nevertheless, the intrinsic radioactivity of the detector components represents an irreducible source of background and therefore active discrimination is mandatory. The DM particle interaction with the detector can release part of its energy into three main channels: ionization, scintillation and lattice vibration. Detecting at least two of this channels allows the discrimination between nuclear and electron recoils.

**Solid-state cryogenic detectors** They consist of an absorber equipped with a thermometer to measure the temperature rise due to an energy deposition. Both thermometer and absorber are coupled to a heat bath to keep them at the correct working temperature. Operating below 1 K allows the reduction of thermal noise as well as a lower material specific heat and thermal conductivity. In this class of detectors most of the energy is deposited in phonons (lattice vibration) and only a minority in ionization and scintillation. Combined phonon and ionization measurement is currently implemented in SuperCDMS [74] and EDELWEISS [75]. These experiments use semiconductor crystal absorbers in which electron-hole pairs and phonons are produced in case of DM interaction with the crystal. The electron-hole pairs are separated and drifted to the surface with an electric field and then detected together with the phonon signal. Currently CRESST

[76] is the most sensitive DM experiment simultaneously detecting phonons and scintillation light. A detailed description of the experiment is written in the next chapter (2). All these three experiments are optimised for low-mass DM searches and can probe masses down to  $\sim 0.2$  GeV.

**Noble liquids detectors** Currently all the experiments of this class are large time projection chambers (TPCs). DM scattering events are measured in a central region confined by a field cage and usually filled with a liquid noble element target. Nowadays the most commonly used elements are Argon and Xenon<sup>5</sup>. The ionization electrons are drifted in the z direction to the anode with electrode grids and field shaping rings, where their magnitude and x-y location is measured. The associated scintillation signal generated by DM interaction is also measured and the time difference between the prompt-light signal and the later-arriving charge signal gives the event location in z for a known electron drift speed. Thanks to the two channel detection, a 3D imaging in the central volume is possible. This together with the separate measurements of charge and light and scintillation pulse shape allows background discrimination. Because of the large volume and mass easily achievable with this technique this class of detectors are optimized for high-mass DM searches. In the last decades the so-called dual-phase TPCs have been developed and optimized for direct dark matter searches. They consist of dual-phase liquid/vapour noble gas TPC whose key feature is the amplification of the signal thanks to charge avalanche in the gas phase. This results in a larger signal/noise ratio and in an improvement of the image quality. At present the best constraints on DM-nucleon interactions come from liquid xenon (LXe) experiments, like LUX [77], PandaX [78] and XENON [79], that probed DM masses down to  $\sim 6$  GeV. Liquid Argon (LAr) experiments like DarkSide [80] have a better background discrimination with respect to LXe experiments thanks to a powerful pulse shape discrimination (PSD). As a drawback this leads to a higher energy threshold.

**Room temperature scintillating detectors** Presently there are several DM experiment using high-purity NaI(Tl) crystals. DAMA/LIBRA, located at LNGS, is the only experiment that reported an annual modulation in the event rate with a statistical significance of  $12.9\sigma$  C.L [81]. It has the largest mass, 250 kg, and the largest exposure: 1.33 t y with an energy threshold of 1 keV and 2.46 t y with an energy threshold of 2 keV. Other experiments currently taking data to probe DAMA results are ANAIS [82] and COSINE-100 [83] while the SABRE experiment [84] is currently under construction. Finally the COSINUS project [85] is developing a cryogenic scintillating bolometer with undoped NaI crystals equipped with phonon and light read-out to improve the particle discrimination.

**Room temperature ionisation detectors** In the last years a DM detector realised with a silicon charged-coupled devices (CCDs) have been proposed with

---

<sup>5</sup>R&D on liquid helium and neon is ongoing.

the DAMIC experiment [86]. CCDs are characterised by low threshold, high energy resolution and high spatial resolution. Thanks to these features the position of the energy deposit can be reconstructed in 3D and the particle type can be identified by the recorded track pattern. Because of the low threshold and the usual small dimension this detectors are indicated for low-mass DM searches. On the other hand, there is the NEWS-G experiment [87] with spherical proportional counters filled with noble gas. This technology has two main advantages: low intrinsic electronic noise and high amplification gain, which both allow to reach energy thresholds of the order of single-electron detection. Moreover the typical design of this detector allow to use different light targets.

**Super-heated liquid detectors** These detectors are threshold devices with the impressive feature that the energy threshold can be determined by the two operating parameters: pressure and temperature. For a given pressure each temperature corresponds to a defined recoil energy threshold. Therefore the energy spectrum can be reconstructed by measuring the rate of bubble formation as a function of temperature. Setting the threshold allow to tune the energy region where to search for DM recoil events removing the background with lower energy. The PICO [88] and MOSCAB [89] collaborations are currently operating bubble chambers with fluorine to investigate the spin-dependent DM interaction.

**Directional detectors** This type of detector would unequivocally confirm the Galactic origin of a signal and could probe the region below the neutrino floor. Considering that nuclear recoils have a range which is about 10 times smaller than the one of Compton recoils of the same energy, gaseous detectors have an excellent intrinsic background rejection if they can measure the range of events precisely. Some of the directional detectors presently in operation are DRIFT [90], DMTPC [91], MIMAC [92] and NEWAGE [93]. Finally the NEWSdm collaboration [94] has proposed a new technique based on fine-grained nuclear emulsions: solid-state detectors with silver halide crystals uniformly dispersed in a gelatine film, where each crystal works as a sensor for charged particles. This nuclear emulsion would act both as target and tracking device. Due to the fine granularity and the high density a superior spatial resolution compared to gaseous detectors is achievable.

As discussed in section 1.3, for iDM detection the heavier the target nucleus, the wider is the kinematically accessible parameter space. Considering also the observed recoil energy window adopted for the analysis by the current experiments, almost all of them are not sensitive to higher mass splittings. Nevertheless, including larger nuclear recoil energies in future analyses will increase the accessible parameter space. However, because Tungsten is the heaviest element currently employed in dark matter searches, experiments like CRESST can probe the largest inelastic dark matter mass splitting.



## The CRESST experiment

CRESST (Cryogenic Rare Event Search with Superconducting Thermometers) is low-background rare event search whose main goal is the direct detection of dark matter. The CRESST facility is located at Laboratori Nazionali del Gran Sasso (LNGS), in Abruzzo, Italy.

In these last decades different underground laboratories have been excavated all over the world and they differ in size, in the support of technology available and in the way to access them. At the moment the LNGS laboratory is the largest underground laboratory: the underground complex consists of three huge experimental halls and bypass tunnels, for a total volume of about 180.000 m<sup>3</sup>. Access to experimental halls is horizontal and it is made easier by the highway tunnel<sup>1</sup>. The rock overburden in all directions of at least 1400 m, corresponding to 3800 meter of water equivalent.

For rare event search physics a low background environment is crucial. In the CRESST experiment this is realised both with shielding and a careful choice of all the materials surrounding the detectors. CRESST shielding is composed of several parts, each one designed against a specific type of background. A schematic drawing of the shielding and the cryostat is shown in figure 2.1.

### 2.1 Background and shielding

There are two main ways to reduce and possibly eliminate background depending on the position of the background source with respect to the detector. The environmental background such as atmospheric muons and natural radioactivity (with related products) is reduced with abatement systems: both active and passive shielding outside to the detector. On the contrary internal backgrounds due for example to the intrinsic radioactivity of the detector components cannot be treated with external shielding. A careful choice of the components material is mandatory but this will not remove all internal background. The residual background has to be reduced as much as possible during the analysis process.

---

<sup>1</sup>Other underground laboratories such as the Boulby Palmer Laboratory (UK), the Kamioka Observatory (JP) and the Canadian underground laboratory Snolab are located inside old mines and vertical elevators are the only possible access.

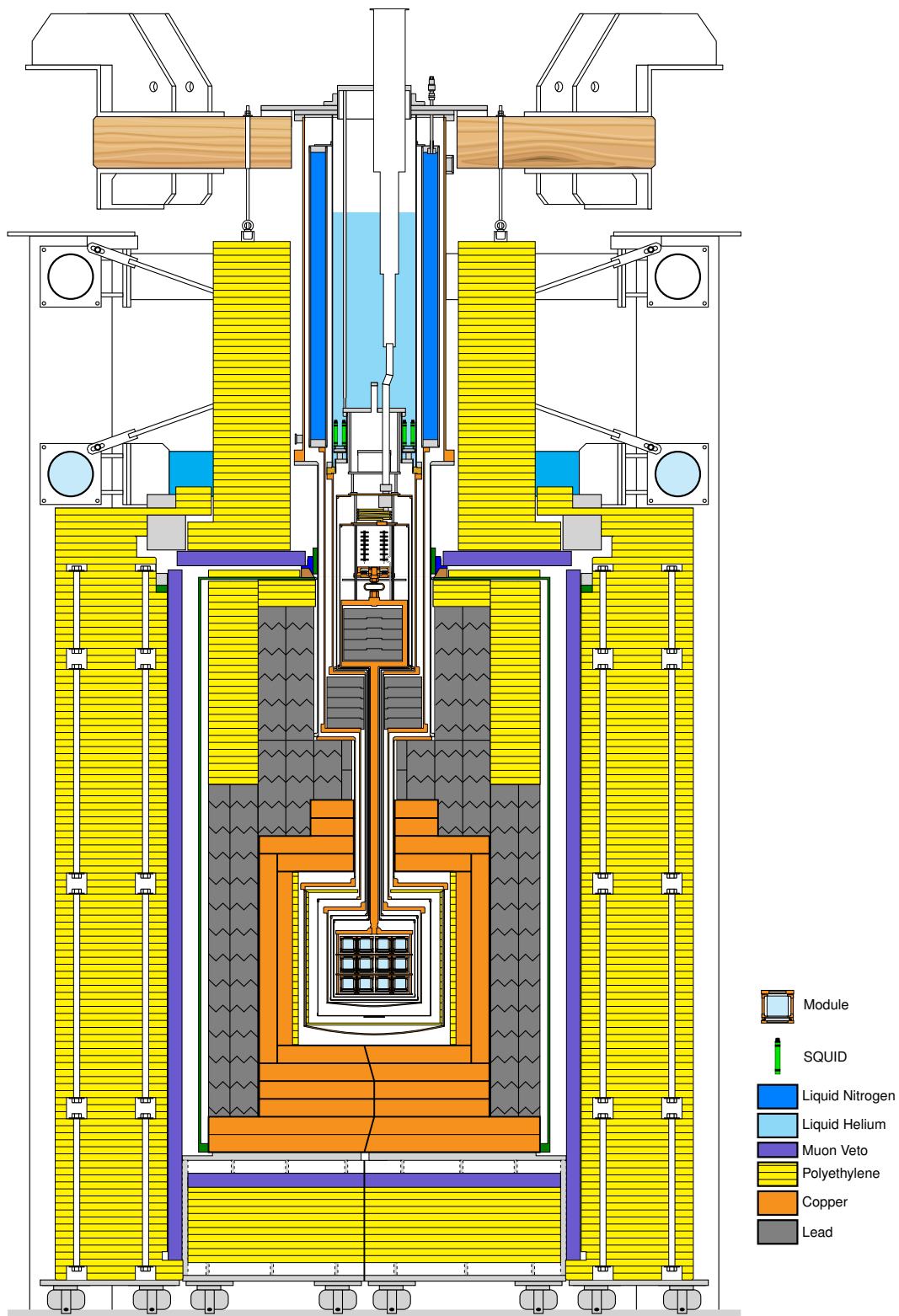


Figure 2.1: Schematic drawing of the CRESST experimental setup. In the center of the drawing the detector carousel is surrounded by the cryostat thermal shields of decreasing temperatures. It is connected via a copper cold finger to the cryostat structure, placed in the top center of the picture. The colors of the shielding are explained by the legend on the right.

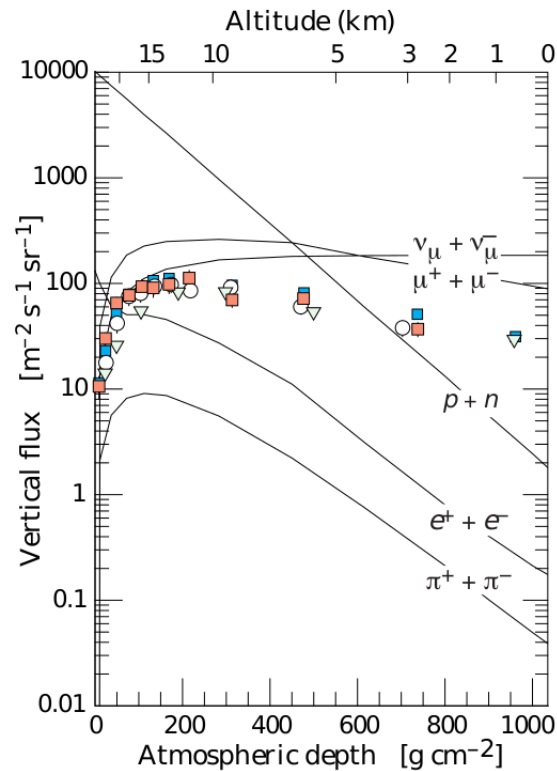


Figure 2.2: Estimated vertical fluxes of cosmic rays in the atmosphere with  $E > 1$  GeV. The points show measurements of negative muons with  $E_\mu > 1$  GeV. [41]

**Muons** Primary cosmic radiation is mainly made of protons and alpha particles and when they enter the Earth's atmosphere they collide with atoms and molecules, mainly oxygen and nitrogen. The interaction produces a cascade of lighter particles, a so-called air shower, which include x-rays, muons, protons, alpha particles, pions, electrons, and neutrons. Atmospheric muons are the most abundant charged particles arriving at sea level and the only ones able to penetrate deeply underground. The reason relies on their small energy loss in the whole atmosphere ( $\sim 2$  GeV), the relatively long lifetime and the fairly small interaction cross section. At sea level the muon flux with  $E_\mu > 1$  GeV through a horizontal area amounts to roughly one particle per  $\text{cm}^2$  and per minute (see figure 2.2). The muon flux inside the LNGS underground laboratory was measured to be  $(3.41 \pm 0.01) \cdot 10^{-4} \text{ m}^{-2} \text{ s}^{-1}$  by the Borexino experiment [95], indicating a muon flux reduction of  $10^{-6}$  thanks to the natural shielding of the Gran Sasso massif. Despite the considerable suppression, remaining muons have to be considered. Interacting with the surrounding material they will produce neutrons that would not only contribute to the background but also mimic the dark matter signal inducing nuclear recoils in the target material. Thus 20 panels of plastic scintillator, each one equipped with PMT, have been installed as muon veto around the CRESST experiment. The total coverage reaches  $\sim 98.7\%$  of the solid angle of the detector, taking into account the hole on the top needed

for the cryostat structure.

**Natural radioactivity** Another significant source of background is the natural radioactivity. Main contributors are the products of the  $^{238}\text{U}$  and  $^{232}\text{Th}$  decay chains and the natural isotope  $^{40}\text{K}$ , naturally present in rocks and materials and producing  $e^-/\gamma$  radiation with energy up to 2.6 MeV. Of course also  $\alpha$  particles are produced in the decay chains but they are not a significant source of background. They are mono-energetic, relatively high energetic ( $\sim$  MeV) and characterized by a short range (few tens of  $\mu\text{m}$ ) which is several orders of magnitude lower than distance they should travel to reach the detector<sup>2</sup>. To reduce environmental background massive shields are required. Materials with high atomic number and high density are best suited because of their high stopping power for  $\gamma$  radiation. Considering that lead satisfy all these prerequisites, a 20 cm low background lead layer (24 ton) has been installed as CRESST shielding against natural radioactivity. As a drawback, lead has an intrinsic radioactivity due to the isotope  $^{210}\text{Pb}$  that after the emission of  $\alpha$ s,  $\beta$ s and  $\gamma$ s will eventually decay into the stable isotope  $^{206}\text{Pb}$ . To shield the detector against the intrinsic radioactivity of lead a 14 cm copper layer (10 ton) has been added between lead and the detector. Considering copper has a large cross-section for neutron capture and it suffers the production of  $^{60}\text{Co}$  when exposed to cosmic rays, it is important to keep its exposure to cosmic radiation as little as possible during production and storage. Apart from that, copper has good thermal properties and high pure copper can be easy produced with current technologies. Consequently it is used for all the innermost parts of the experiment.

**Neutrons** Neutrons are the most dangerous background for direct dark matter search experiments because they mimic dark matter signal: both dark matter and neutrons enter the detectors undetected and eventually produce a signal of nuclear recoil. To screen the detector from the natural neutron stream a shielding of Polyethylene, 40 cm thick, is present in the outer part of the shielding. Polyethylene is a chemical compound with a high number of light nuclei, and this makes it extremely suited to slow down and eventually stop neutrons. From a kinematic point of view the the energy transfer is more efficient for comparable masses. Note that neutrons are not shielded in the usual way: in general they are moderated so that they cannot produce detectable signals inside the detector. Considering that neutrons can be produced also in the lead and copper shielding through  $\alpha$ -n-reactions as well as by muons (which might be missed by the muon veto), an additional layer of Polyethylene has been added inside the copper shielding with a total thickness ranging between 46 mm and 156 mm<sup>3</sup>.

<sup>2</sup>This is no longer true if the  $\alpha$  particles are produced in the internal region of the detector. In this case their background has to be removed with the analysis (see subsection 2.3.5).

<sup>3</sup>The inner Polyethylene shielding consists of two pieces. The innermost is a cylinder 33 mm thick and it is located inside the OVC (Outer Vacuum Chamber). Between the copper shielding and the OVC there is the “middle” Polyethylene shield. Its shape is a cube with a cylindrical hole in the middle for the detector and its thickness goes from 13 mm to 123 mm.

Containers filled with Polyethylene or water (depending on technical reasons) are used for less accessible positions.

**Radon** Another critical component of the natural radioactivity is  $^{222}\text{Rn}$ , a radioisotope produced by the  $^{238}\text{U}$  decay chain and naturally present as gas in rocks. Radon half-life is 3.82 days and this time is sufficient to have radon diffused into the environment. Its decay chains contains  $\alpha$ s and  $\beta$ s that will eventually produce also  $\gamma$ s via bremsstrahlung or nuclear reactions. The measured level of  $^{222}\text{Rn}$  in the underground laboratory is  $\sim 50 \text{ Bq m}^{-3}$  [96]. Radon is a serious source of background since its gaseous state, combined with its sufficiently long half-life, allows it to enter any tiny slit of the experimental setup reaching easily the detector. If Radon decays while in proximity of the detector, its decay products will contaminate the surface. To avoid such contamination, an air-tight box, called radon-box, installed between the muon veto and the lead shielding, is constantly flushed and kept in over-pressure with Nitrogen. For the same reason, all components of the detector are etched and stored under Nitrogen atmosphere before installation.

## 2.2 CRESST Cryostat

CRESST is a cryogenic experiment working at a temperature of  $\sim 10 \text{ mK}$ . The operating temperature is reached with a commercial dilution refrigerator circulating a mixture of two isotopes of helium:  $^3\text{He}$  and  $^4\text{He}$  (Oxford Instrument). The cooling power is provided by the heat of mixing the Helium-3 and Helium-4 isotopes. Below  $\sim 870 \text{ mK}$  the mixture undergoes a spontaneous phase separation forming a  $^3\text{He}$ -rich phase (the concentrated phase) and a  $^3\text{He}$ -poor phase (the dilute phase).

The  $^3\text{He}$  is the working fluid that circulates through the refrigerator thanks to vacuum pumps at room temperature. While entering the cryostat it is purified and pre-cooled in multiple stages until it reaches the mixing chamber, the coldest area of the refrigerator. Inside it  $^3\text{He}$ - $^4\text{He}$  mixture is located, with the two phases (concentrated and diluted) are in equilibrium and separated by a phase boundary. Because of the different concentration,  $^3\text{He}$  flows from the concentrated phase into the dilute one through the phase boundary. The heat necessary for the dilution is the useful cooling power of the refrigerator, as the process of moving the  $^3\text{He}$  through the phase boundary is endothermic and removes heat from the mixing chamber environment. Then the  $^3\text{He}$  leaves the mixing chamber in the dilute phase and, after few stages of warming, the vacuum pumps at room temperature feed it back into the cryostat completing the cycle. For more detailed information see e.g. Ref. [97].

Liquid nitrogen vapor and liquid helium are needed for operating the cryostat thus they have to be refilled three times per week. During refilling and also shortly after detectors are not running stably so data taking is switched off for few hours for each refill and this make up the major contribution to the dead time.



Figure 2.3: CRESST carousel.

All the materials used for the experiment have been carefully selected to obtain an experimental set-up as radio-pure as possible. Of course it was not possible to require the same level of purity of the detector as for the cryostat. Nonetheless, the cryostat structure has a particular design that has the precise intent of minimizing the background (see figure 2.1). The detectors are mounted on a copper structure, called carousel, which is located in a low background cold box. A copper rod 1.5 m long, referred to as cold finger, acts both as holder and thermal coupling with the mixing chamber. Moreover the carousel has no line of sight to non-radiopure materials thanks to an additional 20 cm thick high purity lead shield (Plombum lead with a  $^{210}\text{Pb}$  activity of only 3.6 Bq/kg) placed between the mixing chamber and the cold finger. This shield, combined with another one at liquid nitrogen temperature surrounding the cold finger, serves to block thermal radiation coming from the dilution refrigerator from entering the experimental volume. The cold box consists of five thermal shields: an outer vacuum chamber (OVC) at ambient temperature, a first thermal shield connected to the liquid nitrogen dewar of the cryostat, an inner vacuum chamber (IVC) anchored at liquid helium temperature and two additional radiation shields at 600 mK and 50 mK. All the thermal shields, the carousel and the cold finger are made of radiopure copper, which has been etched and electro-polished to remove any kind of surface contaminations and to reduce the probability of re-contamination. Low temperature detectors are very sensitive to mechanical vibration. To attenuate vibrations coming from the environment the whole cryostat lies on a 20 cm thick wooden plate resting on air dampers with no mechanical connection to the shielding. The vibrations due to the cryostat have been abated by mounting the carousel onto a spring-loaded plate directly fixed to the cold finger. To prevent electromagnetic radiation created by external sources from interfering with sensitive read-out electronics, a Faraday cage surrounds the complete apparatus. A

clean environment for mounting and dismounting detectors is guaranteed by a class-100 clean room installed inside the Faraday cage below the wooden plate.

## 2.3 CRESST detector

### 2.3.1 Cryogenic detector

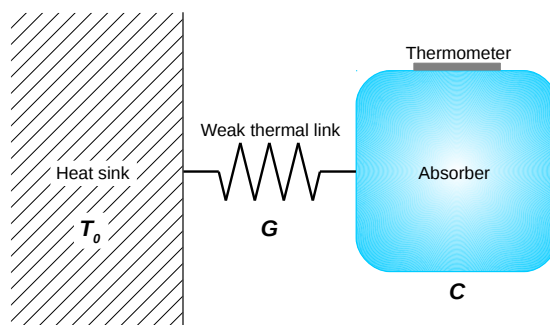


Figure 2.4: Basic scheme of a simple cryogenic detector.

The heart of the CRESST experiment is of course its cryogenic detector. A cryogenic detector is in general composed of three parts. An absorber (or thermal mass) that contains the event and absorbs the incident power and thermalizes the energy, a perfectly coupled thermometer that measures the temperature increase of the absorber and a weak thermal link to a heat sink that brings the absorber temperature back to some defined value in the absence of a signal. A schematic drawing of a basic cryogenic detector is shown in figure 2.4. The absorber with the perfectly coupled thermometer can be characterized by the heat capacity  $C$ , the weak thermal link by its thermal conductivity  $G$  and the heat sink by its temperature  $T_0$ . In an ideal cryogenic detector an incoming particle instantaneously releases an amount of energy  $\Delta E$  into the absorber. This rises the temperature of the absorber by a quantity  $\Delta T = \Delta E/C$  measured by the thermometer. The absorber then relaxes back to the equilibrium temperature of the heat sink through the weak thermal link with a time constant  $\tau = C/G$ . In case of a steady power input  $P$ , the temperature rise will be  $\Delta T = P/G$ . A more elaborate description of the detector concept and a detailed explanation of the thermal response of the thermometer for cryogenic calorimeters as used in CRESST can be found in Ref. [98]. To maximise the detector sensitivity the heat capacity of the system has to be as small as possible. At low temperature the heat capacity of a metal has the form  $AT + BT^3$  where the linear term is due to the electronic excitation and the cubic term is due to lattice vibrations. In insulating crystalline solids the heat capacity is dominated by the lattice specific heat. Considering the temperature dependence of the two contributions, an insulating material is preferable to lower the heat capacity as much as possible with decreasing temperatures. At low temperatures the heat capacity due to the

excitation of phonons can be very well described by the Debye-model [99] [100]:

$$c_{ph} = \frac{12\pi^4}{5} R \left( \frac{T}{\Theta_D} \right)^3 \quad (2.1)$$

where  $c_{ph}$  is the lattice specific heat,  $R$  is the ideal gas constant and  $\Theta_D$  is the Debye temperature, a constant that depends only on the material of the lattice. The main reason why CRESST is a *cryogenic* experiment resides in the  $T^3$  dependence of the crystal specific heat. At temperature of the order of mK the lattice heat capacity is very small and therefor insulating crystal solids are very suitable as absorbers for massive calorimeters.

### 2.3.2 The CRESST-III detector

The CRESST experiment has gone through several stages, each one corresponding to an upgrade of the detector. At present CRESST is in its 3rd stage.

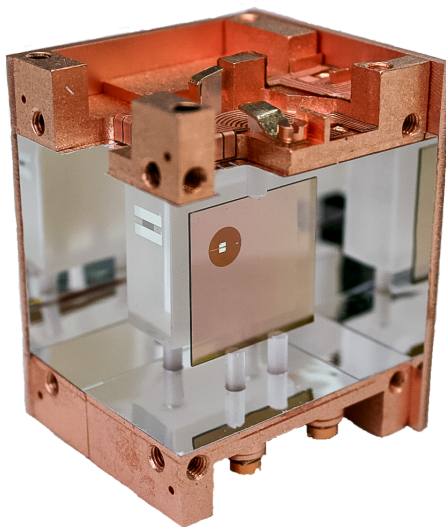


Figure 2.5: CRESST-III module. The copper housing internally covered with the reflecting scintillating foil is partially open. The phonon and light detectors, both equipped with a TES and kept in place with  $\text{CaWO}_4$  sticks are visible.

The CRESST-III detector is composed of two independent detectors called respectively *phonon detector* and *light detector*. The phonon detector (PD) is a cryogenic calorimeter whose main absorber is realised with a 24 gr  $\text{CaWO}_4$  crystal, some of which were highly pure crystals grown within the collaboration by the Technische Universität München (TUM). The light detector (LD) consists of a Silicon On Sapphire (SOS) plate. Both the detectors are equipped with special thermometers described further on in this section. A pure copper cubic housing hosts the phonon and light detectors. The inside of the copper housing is completely covered with a reflecting and scintillating foil (Radiant Mirror Film VM2002 by 3M). The two detectors are kept in place by 6  $\text{CaWO}_4$  sticks (3

sticks for each detector) so that all the component inside the module are active. Finally the sticks holding the PD are equipped with thermometers. A picture of the CRESST-III detector is shown in figure 2.5. Figure 2.8 illustrates a schematic drawing of a CRESST module with all the elements described above.

### 2.3.3 Transition Edge Sensor

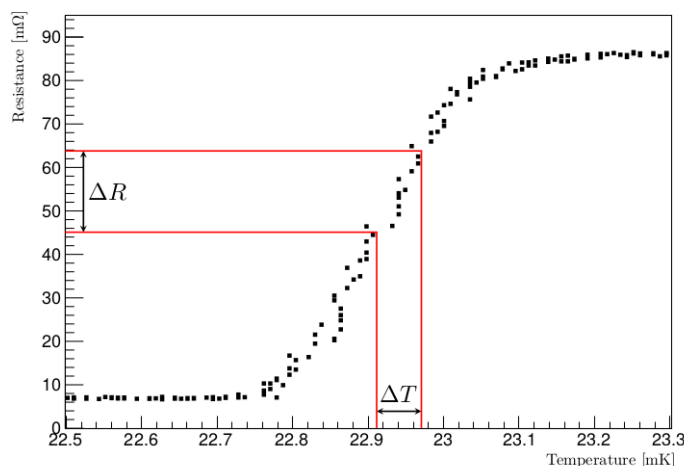


Figure 2.6: Typical transition curve for CRESST thermometers.

The special thermometer used to measure the temperature rise of the detectors are *Transition Edge Sensors* (TES). A TES is a superconducting thin film operated in its transition between the normal-conducting and the super-conducting phase. Thanks to the steepness of the transition tiny temperature rises are detectable. The point where the detector is stabilized is referred to as *operating point* or *working point*.

The working temperature has to be the lowest possible in order to minimize the heat capacity of the detector and this makes tungsten the best choice for CRESST thermometers. Its transition temperature  $T_C^W \simeq 15$  mK is convenient for cryogenic operations and offers a good sensitivity [101]. An example of a typical transition curve of tungsten TES used in CRESST detectors is shown in figure 2.6. From this curve it is possible to appreciate the extremely good sensitivity of these devices: a temperature rise of some tens of  $\mu\text{K}$  corresponds to an increase of the sensor resistance of few tens of  $\text{m}\Omega$ . At the same time it is manifest of the highly non-linear behaviour of this kind of sensor. Because of this a slightly different operating point would produce a very different detector response. Accurate temperature stabilization and constant monitoring are thus fundamental to obtain reliable information during data-taking.

A scheme of the TES structure used in CRESST-III detectors is shown in figure 2.7. The tungsten film, 200 nm thin, is directly evaporated on the target substrate: the silicon-on-sapphire plate for the light detector and the  $\text{CaWO}_4$

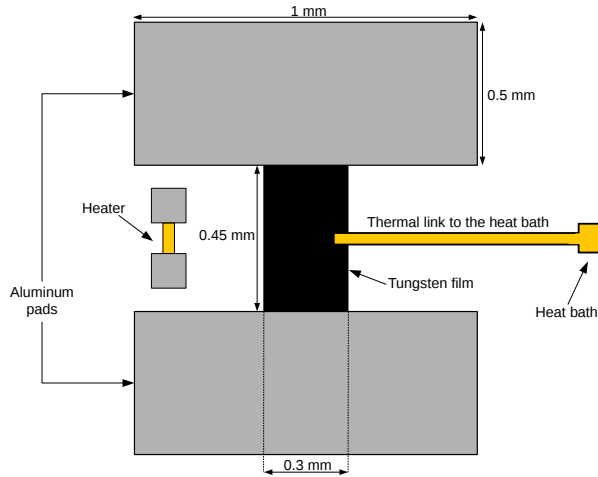


Figure 2.7: TES design used in CRESST-III detectors.

crystal for both the phonon detector and the sticks. Additional structures are needed for a successful operation of CRESST detectors. To improve the collection efficiency of phonons produced in the substrate the dimension of the sensor coupled to the absorber surface should be increased. Enlarging the dimensions of the tungsten film would rise the heat capacity of the sensor as well, leading to a worsening in the detector sensitivity. Thus two aluminum films have been deposited instead touching the TES. Aluminum critical temperature is  $\simeq 1.2$  K [102] meaning that it is in the superconducting phase at the TES working temperature, i.e. the tungsten transition temperature, and thus its contribution to the sensor heat capacity is substantially null<sup>4</sup>. At the same time the two aluminum films allow a proper bonding of the wires needed to apply a bias current. A long thin gold stripe thermally links the tungsten film to the heat bath needed to relax the sensor back to the equilibrium temperature. The heat bath is then bonded with a golden wire to the copper holding structure to keep the heat bath thermally in equilibrium with the mixing chamber temperature at  $\sim 5$  mK. The mixing chamber temperature is well below the operating temperature for CRESST detectors and indeed this allows for a precise stabilization of each TES. Finally, to stabilize the sensor at a precise operating point in its transition within few  $\mu\text{K}$  a heater has been installed close to the TES. It is a separated normal-conducting structure made of aluminum films and an underlying gold film.

### 2.3.4 Working principle

The main absorber constitutes the target of the incoming particles. During the interaction with the crystal a certain amount of energy is deposited in the crystal. More than 90% of this energy is converted in thermal excitation causing

<sup>4</sup>Below the superconducting critical temperature  $T_C$  the linear electronic contribution to the heat capacity is replaced by a term of the form  $\exp(-\Delta/k_B T)$ , with  $\Delta \simeq k_b T_C$

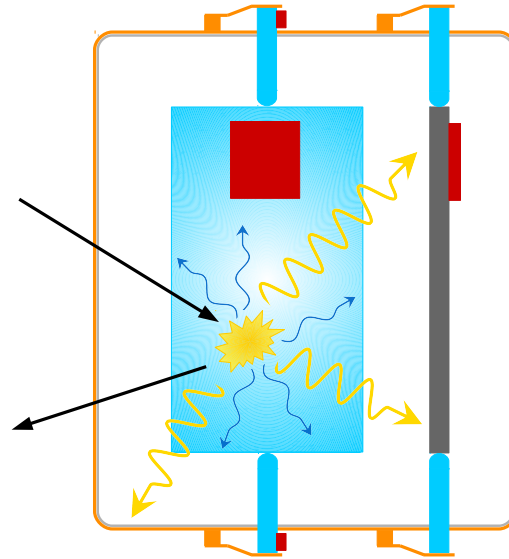


Figure 2.8: CRESST-III basic scheme.  $\text{CaWO}_4$  sticks hold both the phonon and light detector. TESs are depicted in dark red. Interacting particle is represented with black arrows. The phonons and photons produced in the interaction are pictured as blue and yellow squiggly arrows respectively.

an increase in the crystal temperature. The resulting heat/phonon signal is measured by the thermometer coupled with the crystal. A small fraction of the energy deposited in the crystal is instead converted into scintillation light. The photons emitted by the crystal are reflected by the foil until they reach the light detector. The SOS has a high absorption for  $\text{CaWO}_4$  scintillation light that allows an extremely efficient collection of the incident photons. As a consequence, the temperature of the light detector rises and the corresponding light signal is recorded by the thermometer. A schematic representation of the CRESST-III detector working principle is shown in figure 2.8.

Despite the fact that massive external shields are a powerful protection against environmental natural radioactivity, the detector cannot be considered background-free. In fact the detector itself is a possible source of background due to possible contaminations of the inner parts composing it. For this reason an active discrimination is essential. In CRESST-III detectors, this is realized with a 3-channels read-out. The phonon channel provides a precise measurement of the energy deposited in the crystal, which is approximately independent<sup>5</sup> of the interacting particle type. The light channel is fundamental for particle identification since the produced scintillation light strongly depends on the particle type: the scintillation efficiency is close to 100% for particles interacting electromagnetically while it is severely reduced for ions and practically zero for neutrons.

<sup>5</sup>The measured energy in the crystal is perfectly independent of the particle if the small fraction of the energy escaping in form of scintillation light is taken into account.

The sticks channel creates a veto against events not occurring in the main absorber but transmitted to it by mechanical connections.

The role of the foil is twofold. From one side its reflecting properties are crucial for an efficient collection of the scintillation light. On the other side, the foil itself is scintillating and therefore it can be used as an active veto. Together with the  $\text{CaWO}_4$  sticks, they make the housing fully active and this is crucial in order to tag events due to an eventual internal contamination.

### 2.3.5 Background discrimination

The key point for the particle identification and thus background discrimination is the scintillation light. The parameter that describes how the amount of produced light depends on the type of the interacting particle is called quenching factor (QF). It is defined as the ratio between the light produced by a particle of type X and the light produced by a  $\gamma$  at for an equal energy deposition into the absorber  $E_{dep}$ :

$$QF^X(E_{dep}) = \frac{\text{light produced by particle of type X when depositing } E_{dep}}{\text{light produced by } \gamma \text{ when depositing } E_{dep}}. \quad (2.2)$$

It is important to note that the quenching factor depends on the energy of the interacting particle and is not a fixed value applicable over the entire energy range. Despite this, it is possible to consider the quenching factor rather constant in the energy range in which the detector behaves linearly. Although quenching factors have been studied for many scintillating materials, and under different experimental conditions, there are no fundamental nor complete theory that allows the prediction of QFs: only semi-empirical models like the one proposed by Birks are available [103].

Looking at the scatter plot of the energy in the light channel versus the energy in the phonon channel, shown in figure 2.9, it is possible to appreciate the effect of the quenching for different particle types. For both the light and the phonon channel the energies are expressed in electron equivalent which means that an electron recoil of energy  $E$  results in measured energy equal to  $E$  in both light and phonon channel. The plot in figure 2.9(a) was obtained with a CRESST detector exposed to a  $^{57}\text{Co}$   $\gamma$ -source while for the plot in figure 2.9(b) the CRESST detector was exposed to a neutron source. In the first case, only the electron-gamma band is present and its slope is set to one by construction. If a neutron source is used instead of a  $\gamma$  source, two bands appear in the plot: the electron-gamma band and a new one, which corresponds to nuclear recoil events. The difference in the scintillation efficiency for gammas and neutrons is due to the different way in which they interact with solid materials. The scintillation light in fact is proportional to the specific energy loss ( $-dE/dx$ ) of the incident particle. Heavy charged particles (protons and  $\alpha$ s) slow down while moving in a medium and their specific energy loss increases according to the Bethe formula leading to the saturation of the luminescent centers [103] [104]. Consequently,

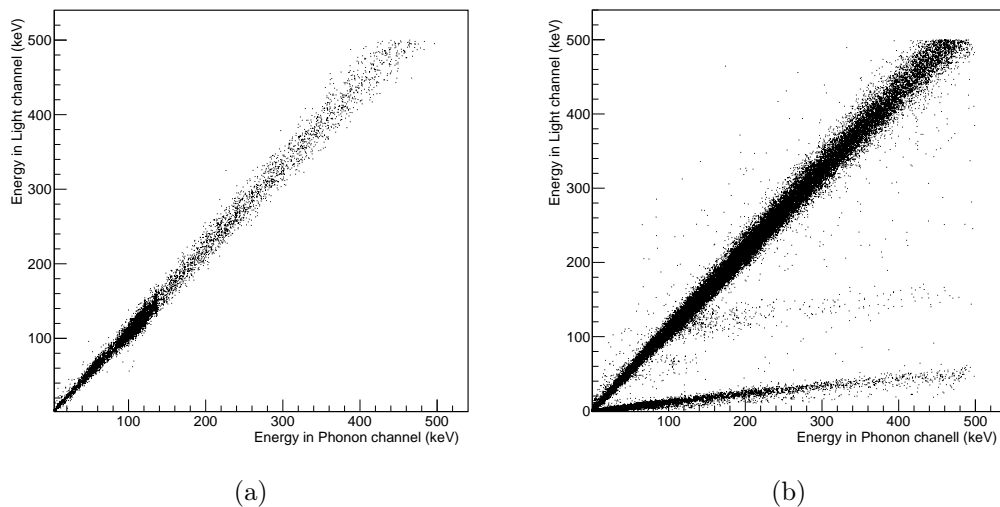


Figure 2.9: Scatter plot of the energy in the light channel versus the energy in the phonon channel of a CRESST module. Data presented in figure 2.9(a) correspond to a calibration with a  $^{57}\text{Co}$   $\gamma$ -source. In figure 2.9(b) AmBe-source neutron calibration data are shown.

the excess deposited energy is lost to competing processes. Fast electrons lose their energy at a lower rate with respect to heavy charged particles. Producing a lower ionization density along the track prevents the luminescent center from saturating. Both gammas and electrons interact electromagnetically (mainly via photoelectric effect and Compton scattering) causing the excitation of the electron levels of the crystal, that are directly responsible for the production of the scintillation light as they de-excite. The overall effect is that light charged particles (electrons, beta particles) on average produce more light per unit energy deposited than do heavy charged particles. Neutrons cannot interact in matter via the coulomb force and this allows them to travel through many centimeters without any type of interaction. The only reasonable interaction would be with a nucleus of the absorber material with two possible outcomes. The neutron may either totally disappear and be replaced by one or more secondary radiations or else the energy and direction of the neutron is changed significantly. That is the reason why in neutron calibration data (see figure 2.9(b)) both bands are present: electron and nuclear recoil bands.

In order to distinguish background events from signal events the knowledge of the QFs corresponding to the different background sources, is crucial. The QF of  $\alpha$ s has been determined with dedicated measurements performed at the LNGS test-cryostat during a study of all the backgrounds in the CRESST dark matter search detectors used for Run32 [105]. Because of the limited resolution of the detector, QFs of scattering off O, Ca and W nuclei cannot be determined with CRESST data. A dedicated measurement in a low-temperature scattering facility for the determination of the QFs of O-, Ca- and W-recoils in  $\text{CaWO}_4$  crystals had been carried out at the tandem accelerator Maier-Leibnitz-Laboratorium (MLL)

Particle type	$QF^{-1}$
e/ $\gamma$	1.00
$\alpha$	5.85
O	$8.03 \pm 0.32$
Ca	$15.2 \pm 1.0$
W	$51.0 \pm 5.7$

Table 2.1: Inverse values of quenching factors for different particle type. The value for e/ $\gamma$  particle is set to one by definition. The  $\alpha$ -QF had been measured at the LNGS test-cryostat [105] while the O-, Ca- and W-QFs had been measured at the Maier-Leibnitz-Laboratorium (MLL) at the Technical University of Munich [106]. The errors reported in the measurements performed at MLL facility were obtained performing the measurements on several detectors.

at the Technical University of Munich [106]. In table 2.1, the QFs obtained from these measurements are reported.

The background discrimination is performed with the light yield variable, defined as the ratio between the energy measured in the light channel ( $E_l$ ) and the energy measured in the phonon channel ( $E_p$ ):

$$\text{Light Yield} = \frac{E_l}{E_p} \quad (2.3)$$

Expressing the energies measured in both light and phonon channel with electron equivalent units, the electron-gamma band have a light yield of unity while all the other types of events exhibit a lower value of light yield. Because of the energy dependence of the quenching factor, the light yield of the electron-gamma band could present some deviation in regions in which the detector is no longer linear. In figure 2.10 the light yield-energy plane for a CRESST detector is shown. The highly populated band at light yield  $\simeq 1$  is attributed to e/ $\gamma$  background and the corresponding expected band is drawn in blue. At light yield less than 0.5, the expected bands for  $\alpha$ -interaction and recoil off Oxygen, Calcium and Tungsten are drawn respectively in orange, red, green and violet. For each band the dashed line corresponds to the mean value while the boundaries are chosen so that the 80% of the events of a certain type is expected to be within such boundaries. The population at  $\sim 100$  keV and with light yield of about 0.6 is due to internal radon contamination.

Radon occurs naturally in minute quantities as an intermediate step in the normal radioactive decay chains through which thorium and uranium slowly decay into lead and various other short-lived radioactive elements. Different from all the other intermediate elements in the aforementioned decay chains, radon is under normal conditions, gaseous and thus it can outgas from natural sources, such as uranium-containing minerals. Unlike the gaseous radon itself, radon daughters are solids and stick to surfaces, such as dust particles in the air, becoming a dangerous source of background. Considering the half-life of all the

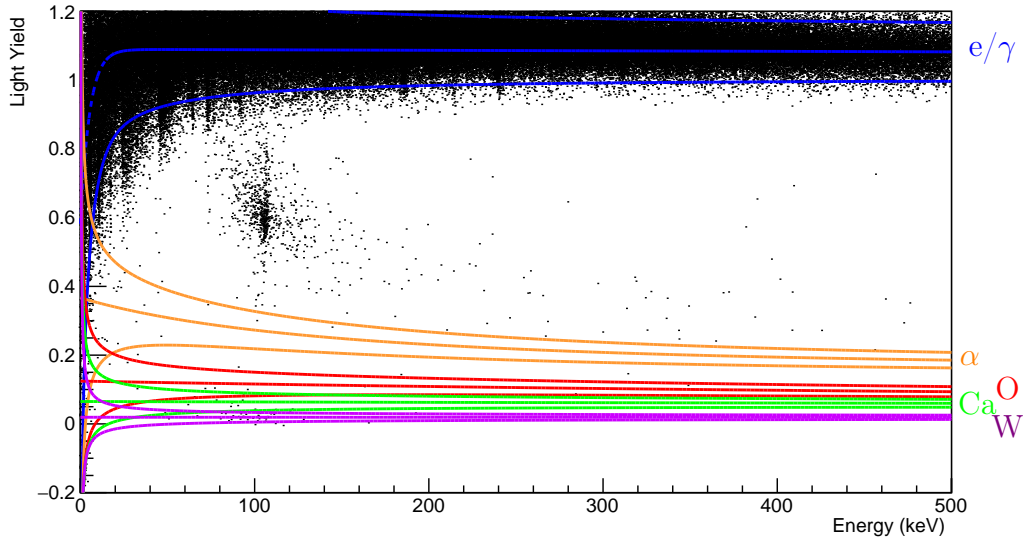
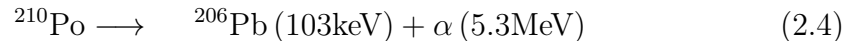


Figure 2.10: Data of a CRESST detector in the light yield - energy plane. The highly populated band at light yield  $\simeq 1$  is attributed to  $e/\gamma$  background and the corresponding expected band is drawn in blue. The expected bands for  $\alpha$ -interaction and recoil off Oxygen, Calcium and Tungsten are down respectively in orange, red, green and violet. For each band the dashed line corresponds to the mean value while the boundaries are chosen so that the 80% of the events of a certain type is expected to be within such boundaries. The population at  $\sim 100$  keV, and with light yield of about 0.6, is due to internal radon contamination.

isotopes produced in the radioactive decay chains, only one is really serious: Rn-222 produced in the U-238 chain with a half-life of 3.8235 days [107]. A scheme of the U-238 decay chain is reproduced in figure 2.11. All the other isotopes produced naturally have a half-life too short and they are not able to come out of the rocks before decaying in the next step of the radioactive decay chain.

Because of the relatively short half-life of the following daughters, the decay chain temporally stops at Pb-210, that has a half-life of 22.20 years [107]. The next two steps of the chain are  $\beta$ -decays and thus easy-to-tag thanks to consistent amount of light produced by the electron emitted in the decay. The next step of the chain is the crucial one for which a fully active housing is mandatory. After the two  $\beta$ -decays described above, Po-210 is produced and it decays with a half-life of 138.376 days [107] according to the following reaction:



The energy of the Pb-206 nucleus will be deposited in the CRESST-III module as a phonon signal. For what concerns the  $\alpha$  particle, the eventually produced signal depends on the surrounding materials. If the housing would not be fully active, the  $\alpha$  could be absorbed by passive material. In this case the event would be reported as a phonon-only event which would perfectly mimic a nuclear recoil event from dark matter interaction. In case of a fully active housing, the  $\alpha$  will

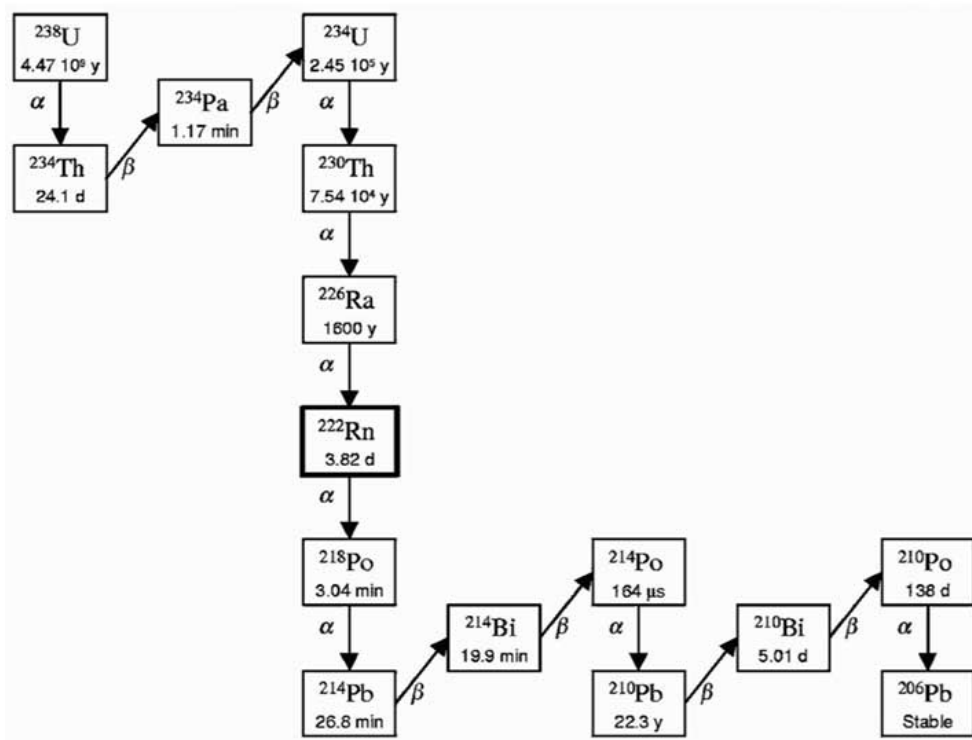


Figure 2.11: Scheme of the Uranium-238 decay chain.

produce a remarkable amount of light allowing the tagging and removal of this insidious background.

The effect of the fully active housing realised thanks to the reflective and scintillating foil can be appreciated by looking at the plot in figure 2.10: the population due to radon contamination is well separated from the nuclear recoil bands. At the same time it can be noticed that the population is not as narrow as one would have expected for a mono-energetic particle (see equation 2.4). The reason lies in the fact that there are two possible sources of radon contamination: the surrounding material and the crystal. In both cases if the decay occurs sufficiently close to surfaces the full energy of 103 keV is detected. However, if polonium stuck on the surrounding material, the Pb-recoil has to get out before entering the crystal and thus it will deposit less energy in the phonon detector. On the other hand, if polonium stuck on the crystal, the phonon channel will measure the energy deposition of the Pb-recoil plus a fraction of the alpha particle energy while it is exiting the crystal. The two possible cases are schematically represented in figure 2.12.

Using the bands shown in figure 2.10, a proper event-by-event discrimination is possible until bands do not overlap. The width of the bands depends on the energy resolution of light detector which is worse with respect to the one of the phonon detector. The overlap of the bands depends on the bands' width as well as on the light output of the detector. A higher light output or a better energy resolution of the LD results in more narrow bands. There is an additional

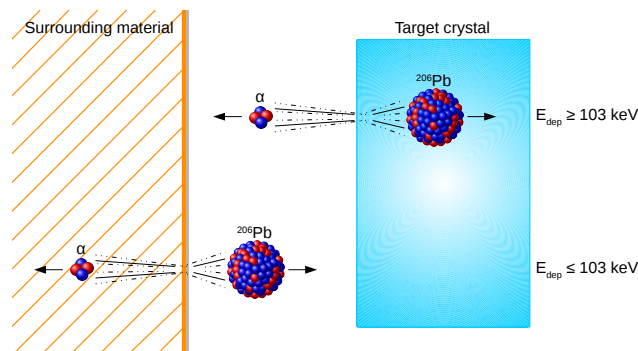


Figure 2.12: Illustration of  $^{210}\text{Po}$  decays occurring either in surrounding material or close to the surface of the target crystal.

effect that concurs in the bands overlapping: the non-linearity of the detector response at low energy causes the downward bending of the  $e^-/\gamma$  band at low energies (investigated in Ref. [108, 109]) increasing the overlapping of the bands. A detailed description of the band structure is given in chapter 4.

## 2.4 Inelastic dark matter search with CRESST

The current stage of the CRESST experiment has a detector design optimized to explore the low mass dark matter particle regime in the hypothesis of elastic scattering with the target. In section 1.3 the inelastic dark matter scenario has been described underlining that the “frontier” of the inelastic dark matter is when the dark matter is heavy ( $\mu \simeq m_N$ ). Moreover it has been shown that heavier target mass elements can access higher mass splittings thus heavy nuclei are more effective in setting constraints on highly inelastic dark matter. Since tungsten is the heaviest element currently employed in dark matter experiments, CRESST can probe the largest inelastic dark matter mass splittings. Considering that the inelastic framework is characterised by the existence of a minimum recoil energy in the detector and the suppression of the effective DM-nuclear scattering rate, CRESST-III detectors are not suited to explore the inelastic dark matter scenario. In light of this, data collected with CRESST-II phase 2 (Run 33) detectors are more suitable for probing inelastic dark matter. CRESST-II phase 2 detectors present a larger mass ( $\sim 300$  gr each) which provides two advantages for the iDM search. Firstly, larger mass leads to higher statistics which is always positive, especially for the iDM search given its typical rate suppression. Secondly, a detector with a larger main absorber has the linear region shifted to higher energies that is more appropriate for the iDM search. A more energetic incoming particle is necessary to saturate a larger volume of absorber. During this run 18 modules with different designs were operated.

Most of them had the so-called “standard design” while some other detectors had an upgraded design aimed to minimise the background contributions. A brief description of the modules design follows.

**Standard design** The main absorber, equipped with a TES, is kept in position by scintillating<sup>6</sup> holding clamps situated inside the detector housing. Two different methods were used to place the TES on the main absorber: it is directly evaporated onto the target crystal or onto a small  $\text{CaWO}_4$  carrier crystal which is in turn glued to the main absorber. The latter method was introduced to avoid exposing the target crystal to high temperatures during the evaporation process.

**Carrier design** No holding is touching the main absorber. A large carrier crystal of the same diameter of the main absorber crystal is glued to the main absorber that is kept in place inside the module by scintillating holding clamps that are touching only the carrier crystal. Thanks to the carrier crystal nothing is touching the main absorber apart from the glue. No TES is evaporated on the main absorber crystal. The carrier crystal is instead instrumented with a TES that will detect temperature rises happening both in the main absorber and in the carrier. Carrier events will be discriminated from target events via their faster rise time.

**Beaker design** A beaker-shaped light detector completely surrounds the target crystal. A large carrier crystal is used to hold the main absorber in place and at the same time as cap to close the beaker. Non-scintillating clamps are used to hold the carrier since in this configuration they do not have a line-of-sight to the target crystal. Also in this configuration events happening in the carrier can be identified by their faster rise time. An additional benefit of this design is an enhanced light collection efficiency.

**Sticks design**  $\text{CaWO}_4$  holding sticks, pressed by clamps outside the housing, are used in this configuration to keep the main absorber in place. In this configuration the main absorber is equipped with a TES.

## 2.5 Data acquisition

### 2.5.1 TES readout

As already discussed in section 2.3.4, the energy deposited in the detector induces a rise in the temperature absorber that in turn leads to an increment of the TES resistance. To keep the TES sensor at the desired working point (see subsection 2.3.3) a very small bias current is needed ( $\mathcal{O}(\mu\text{A})$ ) and consequently a device able to work with such tiny current is crucial. Circulating a too high bias current would heat the sensor bringing it in the normal-conducting phase, out of the transition, and therefore switching it off. To apply the bias current and then

<sup>6</sup>The holding clamps are scintillating due to a ParyleneC coating.

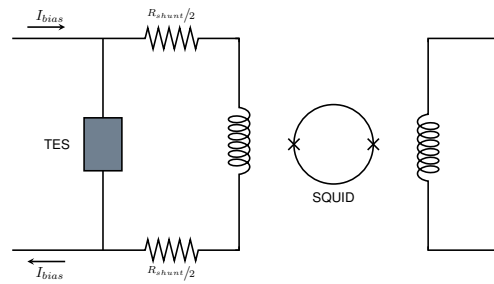


Figure 2.13: TES readout circuit.

measure the resistance change, the TES is connected in a parallel circuit to a coil in series with a resistance  $R_{shunt}$ . For symmetry reasons the resistance  $R_{shunt}$  is realised with two resistance of  $R_{shunt}/2$  value and equal to  $20\text{m}\Omega$  as shown in figure 2.13. The bias current  $I_{bias}$  is constant and adjusted individually for each sensor. A change in the TES resistance causes a change in the splitting of the current inside the circuit and thus a variation in the magnetic field flux generated by the coil. To measure such tiny variations with very small bias currents, Superconducting QUantum Interference Devices (SQUIDs) are used. Their output is a voltage signal proportional to the variation of the induced magnetic field. With this readout circuit the voltage signal recorded by the acquisition system is proportional to the energy deposited in the absorber.

### 2.5.2 TES response

In section 2.3.3 the TES working principle has been described: this device exploits a strongly temperature-dependent resistance only if it is operated in its transition between the normal-conducting and the super-conducting phase. From figure 2.6 it is evident that the sensor has a very short linear operating range. The more it approaches the edges of the transition the less linear the response is until it eventually gets out of the transition producing completely saturated pulses. In figure 2.14 typical pulses from the linear region, non-linear region and the normal-conducting region are shown. This type of devices presents an extremely good sensitivity at threshold which is fundamental for (very-)light dark matter searches. On the other side the small range and the resulting highly saturated pulse makes manifest the need for a method to “extend” the range of the detector. Considering the recoil energies characteristic of the inelastic dark matter framework, a wider detector range is mandatory. One of the main goals of the CRESST analysis process is to extend as much as possible the detector range, obtaining reliable reconstruction of saturated pulses. A detailed description of the analysis chain can be found in chapter 3.

### 2.5.3 Recorded pulses

After the SQUID electronics the voltage signal is split. One part is connected to a transient digitizer that records the signal in time samples of  $40\mu\text{s}$  typically.

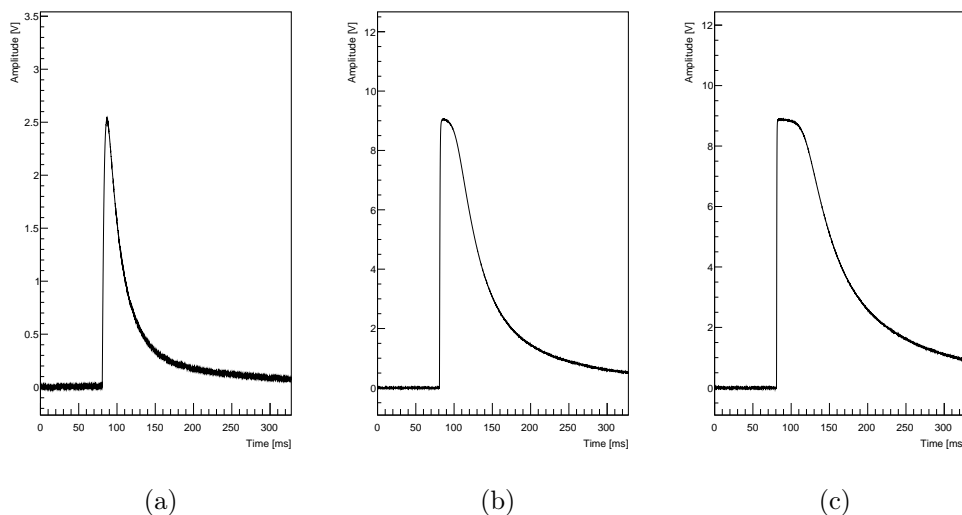


Figure 2.14: TES pulses from three different points of the transition curve: linear region 2.14(a), non-linear region 2.14(b) and normal-conducting region 2.14(c).

The second part of the signal is filtered, amplified and shaped to achieve a high trigger efficiency. After a trigger, the DAQ awaits the so-called post-trigger time before reading out the recorded samples before and after the trigger. The pre-trigger samples are fundamental to precisely determine the baseline and thus the amplitude of a pulse. After a pulse has fired a trigger, it is inhibited for all the time needed for readout plus a time interval equal to the pre-trigger. This avoids pulses very late or very early in the record, for which a precise amplitude, and therefore energy, reconstruction would be impossible. The time interval during which the trigger is inhibited is called “dead time” while the time interval with the trigger active is called “live time”. The sum of these two time intervals gives the “real time” during which the acquisition system is working. Eight transient digitizers are enclosed in one digitizer module. Detectors from the same detector module (phonon and light) are always read out together, even if only one of them triggered. For all other detector modules on the same digitizer module a trigger is required to toggle readout.

#### 2.5.4 Control and heater pulses

A precise stabilization of the TES in its working point is mandatory for a reliable amplitude and thus energy reconstruction. The base temperature of the cryostat is not stable over time because of events like construction works in the nearby experimental areas or earthquakes: they can induce short-term temperature rises and therefore the heating current of each TES has to be adjusted over time. The first step is to verify whether the sensor is in the correct operating point. This is performed injecting large pulses to bring the TES in its normal conducting state. In this situation the resulting pulse is highly saturated and its pulse height is a

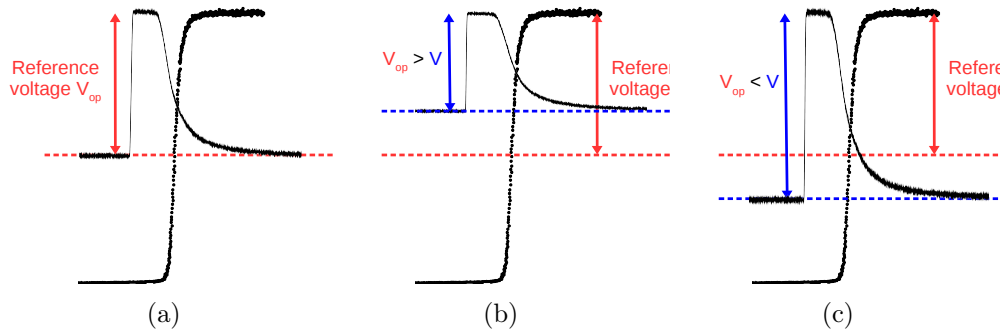


Figure 2.15: Schematic drawing of the TES stabilization mechanism.

direct measure of the distance in temperature between the normal conducting state and the current operating point (see figure 2.15(a)). These large pulses are called “control pulses” and are injected every 6 seconds. This measure of the current working point is used as a feedback to keep the TES at the correct temperature over time. If the pulse height is higher than the reference voltage (see figure 2.15(c)) the temperature of the TES has to be increased to bring the TES back to the correct working point. On the contrary if the pulse height is smaller than the reference one (see figure 2.15(b)) the temperature has to be decreased. Moreover, control pulses are saved to disk because with their timestamps it is possible to keep track of the time interval in which the TES was (not) in its correct operating point and thus whether its output is reliable (or not). The second step consists of injecting pulses of much smaller energies with the heater for two main purposes. Thanks to the well known injected amplitude, these “heater pulses” in fact allow correction for drift of the detector over time as well as for the small deviations from linearity.



## Raw data analysis

As already discussed in section 2.1 the massive shielding accounts for the environmental background but the internal background due to intrinsic radioactivity of the detector components must be removed during the analysis process. The main goal of the raw analysis described in this chapter is to remove events for which the energy reconstruction is problematic.

### 3.1 Data sets

As explained in section 2.4 the analysis presented in this work is performed on the data collected with CRESST-II phase 2 (Run33). During the Run33 three different data-sets were acquired and they will be presented in the following.

At the beginning of the run a  $\gamma$  calibration with a  $^{57}\text{Co}$  source was performed and the 122 keV line is used to fix the absolute energy scale. For what concerns the light detector, the amount of scintillation light detected in the light channel, due to the interaction of 122 keV electrons with the  $\text{CaWO}_4$  crystal, is defined as 122 keV $_{ee}$  (electron-equivalent). Therefore, the light yield of electron recoils of 122 keV is equal to 1 by definition.

At the end of the run a neutron calibration campaign with an AmBe source was accomplished in order to study the response of every individual detector module to neutron-induced nuclear recoils. More precisely, in Ref. [106] it was found that the value of the quenching factors (defined in section 2.3.5) can vary between different crystals ( $\mathcal{O}10\%$ ). Precise values of the quenching factors for different particles obtained with a dedicated measurement have been presented in 2.3.5. Even if this measurement allowed a much more precise determination of QFs, crystal-specific effects can only be determined in the actual measurement campaign with neutron calibration data. More detail can be found in 4.3.

In between the two calibration runs a long physics data taking was performed. For slightly more than two years the CRESST cryostat had been refilled and attentively monitored to allow the acquisition of the so-called “background data”. From this huge data set, information on iDM will be obtained.

In table 3.1 the real time periods and the live time<sup>1</sup> (expressed in days) of the

<sup>1</sup>The live time is the time during which the detector acquisition system is really available to record a possible signal (see subsection 2.5.3).

Data sets	Real time periods	Live time (days)
$\gamma$ calibration	19-25 July 2013	4.82050
neutron calibration	23 June - 15 July 2015	18.8930
background	30 July 2013 - 2 June 2015	$\sim 520^a$

Table 3.1: Real time periods of the three data sets with relative live time expressed in days.

<sup>a</sup> The precise live time is different for each detector because it depends on the number triggers and the consequent time interval for which the trigger is inhibited (see subsection 2.5.3).

three different data sets is reported.

## 3.2 Event types

During data taking of the three different campaigns, four distinct types of events were acquired by both the phonon and light detectors. As already explained in 2.3.4, an event detected by a CRESST module is defined by two coincident pulses coming one from the phonon detector and the other one from the light detector. For this reason both channels are always acquired regardless of which of the two actually triggered. A description of the event type acquired during data taking follows.

**Control pulses** are large pulses injected to the heater and necessary to monitor the TES and keep them in the correct working points; they are usually injected every few seconds.

**Test Pulses** are injected to the heater also. Unlike the control pulses, test pulses (TPs) have smaller and varying amplitude. With TPs a more precise energy calibration can be achieved and how this is obtained is described later in this chapter.

**Empty baselines** are acquired by the DAQ with a trigger artificially sent by the DAQ itself. They provide a precise measurement of the noise, in particular of possibly time-dependent noise conditions.

**Particle pulses** are all events causing a trigger. Most of them are due to energy depositions by particle interactions but the trigger can be fired by other effects, for example high fluctuations in the baseline noise.

## 3.3 Analysis chain

In this section the basic procedure of the analysis of all the pulses recorded by the DAQ is presented step-by-step.

1. Raw parameters evaluation. As described in 2.5.3, the acquisition chain samples the signal and stores the result together with some other information related to the signal, like the time stamp or the event type. In addition to such information, other parameters are calculated offline with simple algorithms such as a moving average over 50 samples. This system allows for a fast processing but the parameters often lack the required precision and additional steps are needed. In table 3.2 a list of the main parameters stored for each pulse is presented.
2. Template building and fit procedure. In order to improve the precision of the pulse parameters each pulse is fitted with a template. To build the template  $\gamma$  calibration data are needed therefore the detailed procedure of the template creation as well as the fit technique is described in section 3.5.
3. Correction of time-dependent effects. Because of the steepness of the TES transition, even a small change in temperature<sup>2</sup> can lead to a different pulse height. To monitor the TES response over time TPs of known amplitude are injected periodically in the heater (see subsection 2.5.4) and this procedure is carried out for each channel. For each injected test pulse amplitude (TPA) the corresponding fitted amplitude over time can be plotted as shown in figure 3.1. The analytical time-description of the TES response for each TP is obtained with a spline fit. A spline is a function defined piece-wise by different polynomials continuously connected to each other. The fit process consists of two steps. First of all, each point of figure 3.1 is convoluted in time with a normalised Gaussian distribution with sigma equal to 30 minutes. Secondly, the resulting points are connected with a cubic spline interpolation. The resulting analytical description, referred to as “temporal spline” from now on, corresponds to the red line in figure 3.1. In order to have a reliable description of the TES response for each TP, it is extremely important to remove eventual overlap of the distribution of fitted amplitude of different injected TP amplitude.
4. Energy conversion. With the analytical description of the TES response over time for all the injected TP amplitudes, the conversion of the fitted amplitude into equivalent TPA for each pulse can be done. Evaluating the temporal spline at a given time, namely the time-stamp of a given pulse, for all the injected TPA and performing a spline interpolation<sup>3</sup> of the obtained points the so-called “transfer function” is obtained for that specific time. Using this curve the fitted amplitude of the pulse is converted in equivalent TPA. Finally the Conversion factor from Pulse height to Energy (CPE)

---

<sup>2</sup>Temperature fluctuations of the order of tens of  $\mu\text{K}$  are small enough to not bring the TES out of its linear region and so not corrected by the control pulse feedback system.

<sup>3</sup>Here an interpolation is performed instead of a fit because the points obtained from the temporal spline evaluation give the TES response at a precise time for different injected amplitudes.

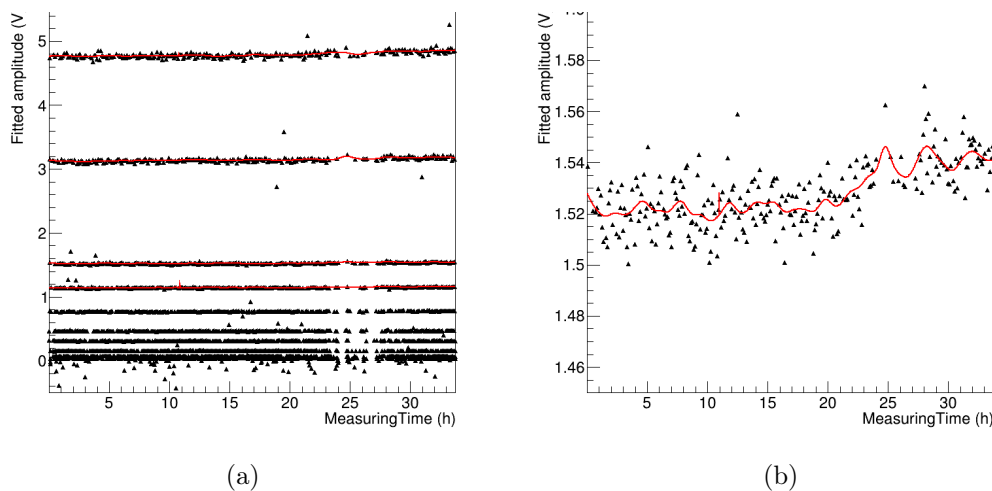


Figure 3.1: Fitted amplitudes of all the injected TPAs as a function of the MeasuringTime variable for a given file are shown with black dots. In red the analytical description of each TPA, resulting from a spline fit and referred to as “temporal spline”, is also shown only for the higher TPAs (figure 3.1(a)). The zoom for injected TPA = 2 V is shown on the right (figure 3.1(b)).

can be obtained using the prominent 122 keV peak in the energy spectrum expressed in terms of equivalent TPA. The final energy spectrum expressed both in equivalent TPA (bottom axis) and in energy (top axis) is shown in figure 3.2.

### 3.4 Stability and Rate Cut

Before going into detail of the analysis performed on each different data set, the stability cut and the rate cut have to be introduced. These two cuts are applied a priori on all the data and are used to remove events acquired with the TES out of its linear region (stability cut) or in situation of high noise and thus high trigger rate (rate cut).

#### 3.4.1 Stability Cut

As already described in section 3.2 during data taking, control pulses needed for the TESs stabilization, are acquired. The feedback system explained in subsection 2.5.4 reliably controls long-term drifts but it is not efficient for short-term deviation from the operating point. Such deviations are due mainly to mechanical vibrations that cause a dissipation of the heat that can induce a temperature rise in the TES. The mechanical vibrations can be induced both externally from the cryostat (trucks moving inside the laboratory, earthquakes etc.) and internally (1K-pot vibrations). Thus short-term instabilities have to be accounted for in the offline analysis. The basic idea is to define, individually for each de-

Parameter name	Abbreviation	Units	Description
MeasuringTime	-	h/d	Elapsed time since the beginning of the file.
CpuTimeSec	-	s	Absolute time of the event.
TestPulseAmplitude	TPA	V	Injected amplitude of TPs which is proportional to the injected energy.
PulseHeight	PH	V	It is evaluated as the difference between the highest value in the record and the baseline level. Both the pulse height and the baseline level are determined using a moving average over 50 samples.
PeakPosition	PP	ms	Position in the record corresponding to the maximum signal (pulse height).
BaseLineDiff	BLD	V	Difference between the baseline level before and after the pulse. The two baseline levels are calculated with a moving average over 50 points: first and last 50 points of the record respectively.
MinDerivativeBaseLine	MDBL	ms <sup>-1</sup>	Minimum value of the pulse derivative divided by the baseline RMS. The derivative is evaluated for each point of the pulse as the ratio between the voltage difference of two consecutive points and their time difference (i.e. the sampling time). The baseline RMS is the root mean square of the baseline calculated with the first 50 points of the recorded time window.
TriggerDelay	-	ms	Elapsed time since the trigger firing. Each detector of a module can trigger a readout and the first detector that triggers the digitizer module has zero trigger delay.

Table 3.2: Description of the raw parameters used for the analysis.

tector, an allowed deviation from the operating point. The distribution of the control pulses for the phonon channel of module VK31 is shown in figure 3.3. It is centered around the TES operating point and close to it the distribution can be approximately fitted with a Gaussian. For each detector the control pulses acceptance region was defined as  $\mu \pm 3\sigma$ , with  $\mu$  and  $\sigma$  being respectively the mean value and the standard deviation of the fitted Gaussian. The accepted region for the phonon channel of module VK31 corresponds to the shaded area in figure 3.3. An event is considered stable if it happens in a time interval enclosed between two stable control pulses. Consequently an event is flagged as unstable if *even just one* of the two control pulses is unstable. This check has to be performed for each event and for each TES.

### 3.4.2 Rate Cut

During some data taking periods, unusually high rates are present. Only a small fraction of these periods are removed by the stability cut thus the rate cut has been introduced. An increased rate in fact points to the presence of electronics disturbances, partially correlated to microphonics, that cause the trigger to fire. In figure 3.4 the number of events as a function of time is shown in 10 minutes width bin on the right with the relative projection of the y-axis on the left for module VK31. Time intervals with zero counts correspond to detector maintenance, during which the acquisition is stopped. A threshold in rate has been set

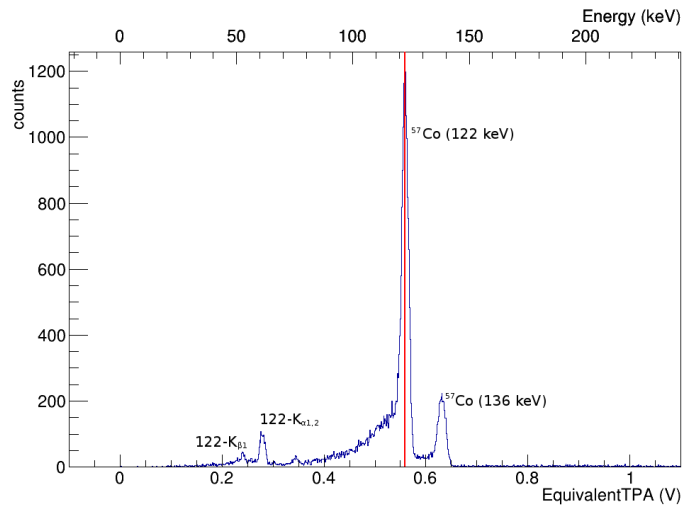


Figure 3.2: Final energy spectrum for  $\gamma$  calibration data expressed both in equivalent TPA (bottom axis) and in energy (top axis). The red line corresponds to the position of the 122 keV peak while the peak at  $\sim 0.63$  V corresponds to the 136 keV peak of  $^{57}\text{Co}$  source. The other peaks in the range  $[0.2 - 0.4]$  V correspond to the  $K_{\alpha 1}$ ,  $K_{\alpha 2}$ ,  $K_{\beta 1}$ ,  $K_{\beta 2}$  escape lines of tungsten X-rays. More precisely the small peaks at approximately 0.24 V and 0.28 V correspond to the escape peaks  $122\text{-}K_{\beta 1}$  and  $122\text{-}K_{\alpha 1,2}$  respectively [110].

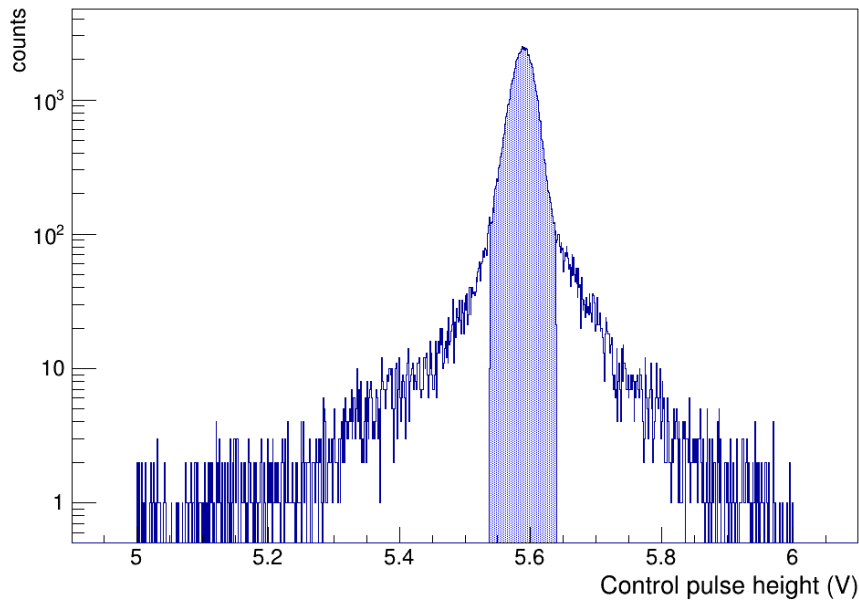


Figure 3.3: The distribution of the control pulses for the phonon channel of module VK31 during  $\gamma$  calibration data taking. The shaded area corresponds to the control pulses considered stable.

for each detector: events happening in time intervals in which the rate is higher than the decided threshold are removed from the following analysis by the rate cut.

## 3.5 Gamma calibration data

As discussed at the beginning of section 3.1 the main reason for the  $\gamma$  calibration is the calibration of the absolute energy scale. Nevertheless, this data set is best for the template creation as it provide lots of pulses with similar shape. Further details are given in the following subsections.

### 3.5.1 Template creation

To obtain a noise-free description of the pulse shape, a template is built for each channel by averaging over a large number of measured pulses corresponding to the same energy and coming from the linear region of the detector. In fact, the more similar in shape are the pulses used for create the template, the better is the effect of the averaging in cancelling out any randomly distributed noise components. Considering that pulses induced by a particle interaction have a different shape with respect to the ones obtained with a TP injected to the heater, different templates have to be produced for the two event types. Of course, the higher the number of pulses used for the averaging, the more enhanced is the noise reduction. For what concerns the TP template, the statistics are not an issue considering the high number of TPs injected for each amplitude during

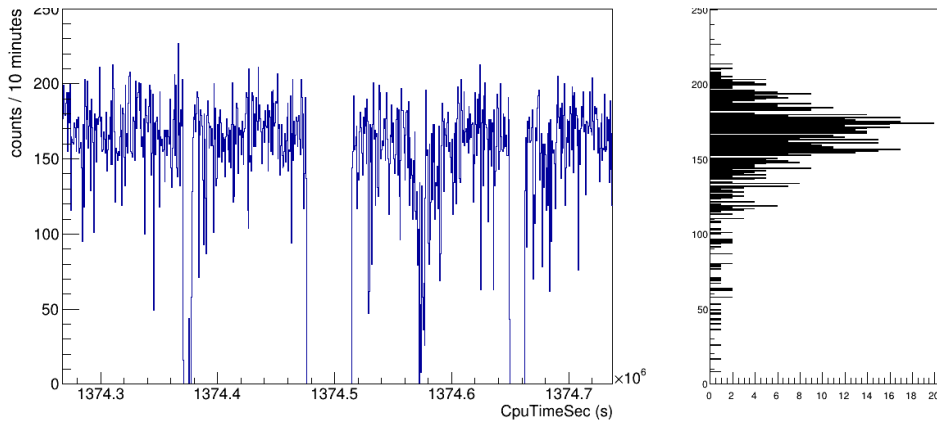


Figure 3.4: Left plot: number of events as a function of time in 10 minutes width bin. Right plot: relative projection on the y-axis. Plots obtained with  $\gamma$  calibration data of module VK31 phonon channel.

data taking. Regarding particle event types, pulses from the 122 keV  $\gamma$ -peak are used to build the template to maximise the noise reduction.

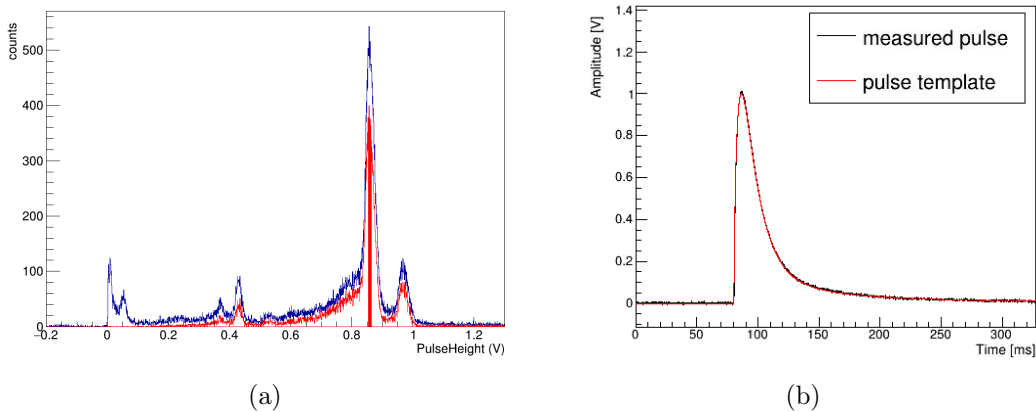


Figure 3.5: Effect of the selection on the PH distribution for the template creation and resulting template. In figure 3.5(a) the blue line corresponds to the PH distribution with no quality cuts applied. The PH spectrum obtained after the data quality cuts is shown with the red line. The template is then created with pulses from the narrow PH range filled in red. The resulting template is shown in 3.5(b) superimposed on one of the pulses used to build the template itself.

For both the event types, the sample of pulses employed for the template creation is obtained with a basic data quality selection<sup>4</sup> and then selecting a narrow PH range. In figure 3.5(a) the effect of the data quality selection on the PH distribution as well as the PH range selected for the template creation is

<sup>4</sup>The detailed description of the variables and the criteria used for the data quality selection is given in section 3.6

shown for the phonon channel of a CRESST module. On the right (figure 3.5(b)) the resulting template (red line) is drawn above one of the pulses used to build it.

### 3.5.2 Fit procedure and Truncation Limit

For each pulse a more precise estimation of the pulse height is obtained by fitting the template with an amplitude scale factor, baseline and time-shift as free fit parameters, where the time-shift is the time correction of the template to better align and fit the acquired pulse. To extend the linear range of the detector a truncated fit allows us to estimate the amplitude for pulses originating from non-linear or saturated region of the TES. The procedure consists of excluding the part of the pulse in which the non-linearity behaviour of the detector becomes evident and performing the fit only on the truncated pulse. The threshold level

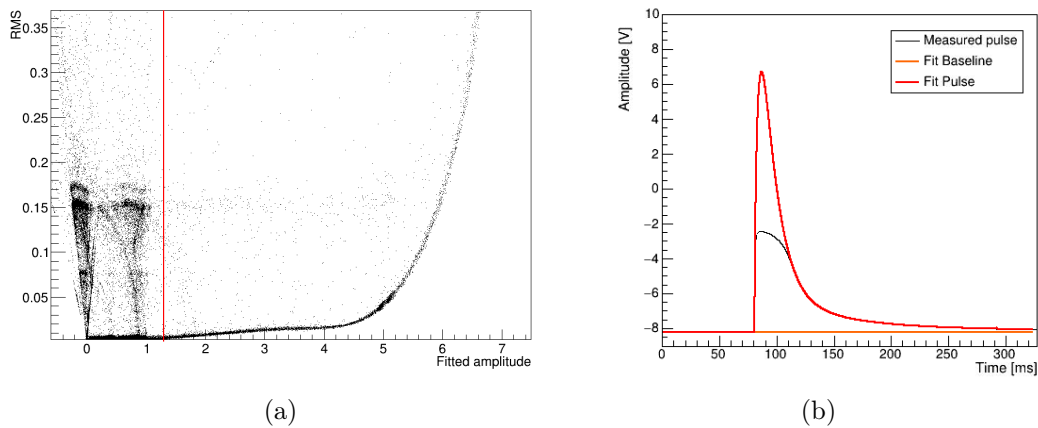


Figure 3.6: RMS of the non-truncated fit as a function of the fitted amplitude is shown in figure 3.6(a). In red the chosen TL is drawn. In figure 3.6(b) the result of the truncated fit of a non-linear pulse is shown.

above which the points of the pulse are not considered in the fit operation is called Truncation Limit (TL). To determine the TL value a first non-truncated fit is performed on all the  $\gamma$  calibration data set for each channel. The trend of the fit RMS, as a function of the fitted amplitude (see figure 3.6(a)), allows the identification of the region in which a simple scaling of the template well describes the detector response. As soon as the RMS starts to increase, it means the scaled template is no more an appropriate description for the measured pulses because non-linear effects take over. Therefore the TL is chosen as the maximum amplitude at which the scaling template fit does not produce an appreciable rise in the RMS value. The choice of the TL depends also on the type of analysis one has to make as the TL set the number of samples of the rising edge and the decaying tail considered by the fit to reconstruct the original pulse. With a low TL and huge pulses, only few samples will be available to determine the amplitude and the shape of the original pulses that might be misreconstructed.

In case of a high TL, it might happen that the fitted amplitude of pulses coming from a slightly non-linear region is not reliable as few samples corresponding to the non-linear region of the TES transition are below the TL and thus included in the fit procedure. Therefore the TL is one of the settings that must be optimized as a goal of the analysis. Since the linear response of the detector strongly depends on the TES transition, for each detector instrumented with a TES, the proper TL has to be found. For the same reason the truncated fit of TP and particle signals recorded by the same detector will be performed with the same TL. Once the TL has been defined for all the detectors, a second *truncated* fit is performed on all the  $\gamma$  calibration data set. In figure 3.6(b) the result of the truncated fit for a saturated pulse is shown. The black line corresponds to measured saturated pulse while the pulse reconstructed by the truncated fit procedure is depicted in red.

### 3.5.3 Conversion from Pulse height to Energy (CPE factor)

Before proceeding with the analysis chain described in 3.3, pulses with problematic fit has been removed using the RMS variable which corresponds to the RMS of the truncated fit. Then time-dependent effect due to small changes in the TES working point have been corrected with the temporal spline procedure. Finally the fitted amplitude has been converted into equivalent TP amplitude through the transfer function. The resulting spectrum for module VK31 is shown

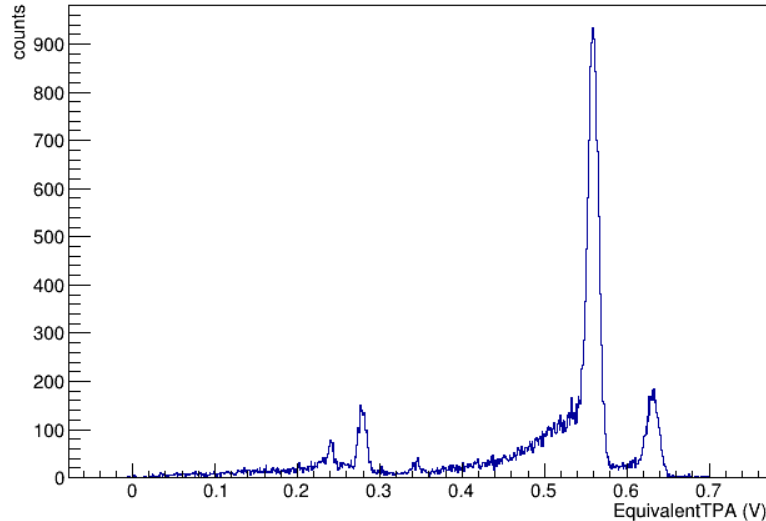


Figure 3.7: The EquivalentTPA spectrum for the phonon channel of module VK31 after data quality and RMS selections.

in figure 3.7. Using the 122 keV  $\gamma$  peak of the  $^{57}\text{Co}$  source, each phonon and light channel can be calibrated with its specific CPE factor.

In conclusion, with  $\gamma$  calibration data key elements for the analysis chain are obtained for all the detectors and will be used for the analysis of all the other data sets.

## 3.6 Background data

Background data have been acquired for almost 2 years collecting a gross exposure of  $\sim 160$  kg d for each detector. This data set is the one used for the proper dark matter search. In order to avoid any unwanted bias a blind analysis is performed on this data set. Namely all the selections are developed using only a small fraction of the entire data set, the so called “training set”, and then they are applied, with no modification, to the full data set. The amount of data used for the training is the result of a compromise: if it is too little the statistics are not sufficient to properly build the cuts; if it is too much the technique loses its motivating purpose. For this analysis the training set corresponds to  $\sim 20\%$  of the full data set and to make it really representative of the full data set the sub-sample is chosen randomly.

The main goal of this low level analysis is the selection of events/signals than can reasonably be considered the result of the interaction of a DM particle with the detector. Considering that a reliable energy reconstruction is crucial for a trustworthy high level analysis and that it is highly unlikely that a WIMP particle could interact more than once within the experimental volume, the cuts described in the following subsections are needed.

### 3.6.1 Data quality cuts

In order to guarantee a reliable energy reconstruction, pulses whose amplitudes cannot be determined properly by the truncated fit procedure have to be discarded. To clean the data set from these unwanted pulses, some basic data quality cuts are defined with the raw parameters described in table 3.2 and the RMS resulting from the template fit process.

**BaseLineDiff** The BLD parameter is calculated by subtracting the average of the voltage of the first 50 samples in the record from the average of the voltage of the last 50 samples. This cut consists of requiring that the baseline levels before and after the pulse are similar and it allows us to remove multiple invalid event classes. One of them corresponds to pulses which have not completely recovered inside the recorded time window. The higher the baseline level after the pulse, the lower the number of samples below the TL that are crucial for the amplitude scaling factor estimation. Then there are several other classes of events due to well-known artifacts and are discarded with this cut. The SQUID resets intervene if the SQUID output is outside the dynamic range of  $[-10;10]$  V restoring the baseline level to a predefined value. Flux quantum losses appear for pulses rising too fast for the SQUID to follow, resulting again in a change of baseline level. Decaying baselines are recorded by the DAQ after a very large energy deposition in the previous record, because the pulse did not yet relax back to equilibrium after the reactivation of the trigger.

**PeakPosition** The PP parameter as determined by the moving average over 50 samples is required to be in the correct position inside the recorded time window

considering the number of pre-trigger samples fixed by the acquisition system. The selection becomes less strict for small pulses considering that fluctuation of the noise might be misidentified as a pulse. In particular the PP cut is applied only on the phonon channel leaving the PP of the light channel free to “move”. The reason of this choice relies on the event type object of the analysis: a well-above-threshold phonon signal associated to a very small signal in the light channel. In fact for signals below threshold, the PP value is calculated on the noise fluctuations resulting in a random value.

**MinDerivativeBaseLine** The MDBL parameter is the minimum value of the pulse derivative divided by the RMS baseline, both determined with the moving average algorithm over 50 samples. This cut rejects pulses with an absolute value of MDBL too high. These values are caused by the presence of spike of various amplitudes that can compromise the fit results.

**TriggerDelay** The TriggerDelay parameter is the elapsed time since the trigger firing. For each pulse the TriggerDelay is equal to zero if that pulse had fired the trigger. It corresponds to a positive number for pulses above the trigger threshold that had not fired the trigger. Finally it is set to a negative value for pulses acquired even if below threshold. Considering that the event type object of the analysis is a well-above-threshold phonon signal associated to a very small signal in the light channel, also the TriggerDelay cut is applied only to the phonon channel, requiring a phonon signal at least always above threshold. More precisely, this cut is needed to remove events in which the trigger fired because of a positive noise fluctuation in the light channel and the random value of the PP variable for the phonon channel would pass the PP cut.

**RMS** The RMS parameter corresponds to the root mean square of the difference between the pulse and the fitted template samples divided by the number of total samples considered for the fit. In fact, in case of a truncated fit, only the points below the TL are considered for the fit as well as for the RMS evaluation. The RMS cut aims to remove pulses for which the scaled template is not representative of the original measured pulse.

In figure 3.8 a selection of invalid events removed with the data quality cuts is shown.

### 3.6.2 Carrier cut

For the modules with a carrier (see section 1.3) an additional cut has to be applied. In fact signals in the phonon channel can be produced by events happening in the main absorber as well as in the carrier. Due to the reduced dimension of the carrier crystal, and to the mechanical stress to which the carrier itself is subjected, events without associated light might occur. As these events are indistinguishable from nuclear recoils, they would be a serious background for dark matter searches and therefore such events have to be rejected. Moreover

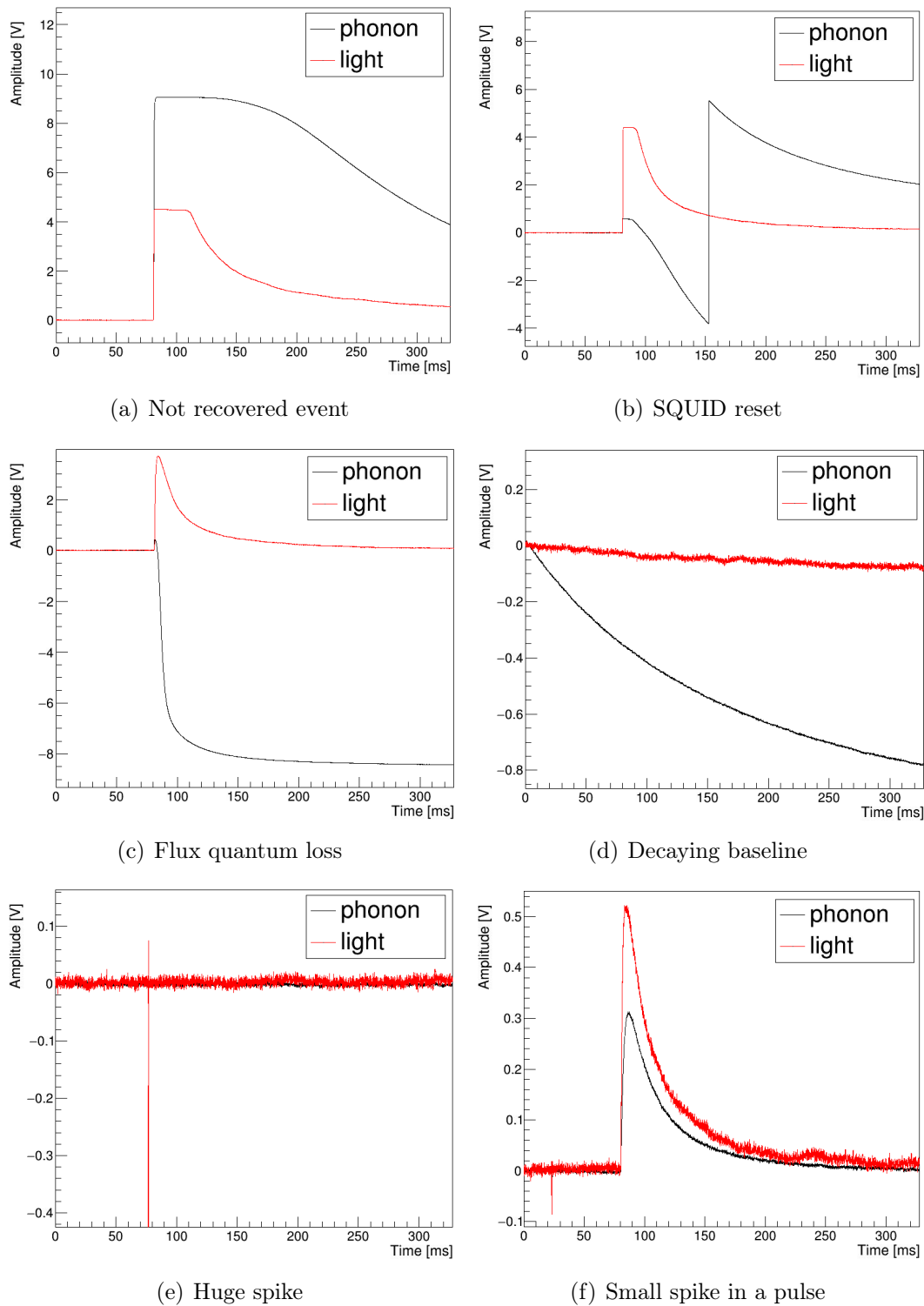


Figure 3.8: Examples of problematic events. In all these events either the phonon or light signal has some feature for which the reconstructed pulse would not be reliable. For the phonon signal in figure 3.8(a),3.8(b),3.8(c) and 3.8(d) the baseline level would not be reliable. For the light signal of figure 3.8(e) the spike would be misidentified as signal leading to a meaningless energy value. The small spike present in the light signal of figure 3.8(f) would worsen the baseline extrapolation and therefore the pulse fit.

the signal shape will be different depending on its origin: the smaller the carrier volume the faster the recorded pulse. Such a difference determines a wrong fitted amplitude estimation leading again to the need for these events to be removed from the data set.

To take full advantage of the different pulse shape for these events, each pulse is fitted twice, once with the standard template for absorber events and once with a template created from carrier events. Then the following parameter is evaluated:

$$\text{RMSratio} = \frac{\text{RMS}^a - \text{RMS}^c}{\text{RMS}^a + \text{RMS}^c} \quad (3.1)$$

where the  $\text{RMS}^a$  and  $\text{RMS}^c$  are the RMS resulting from the pulse fit performed with the *absorber* template and the *carrier* template respectively.

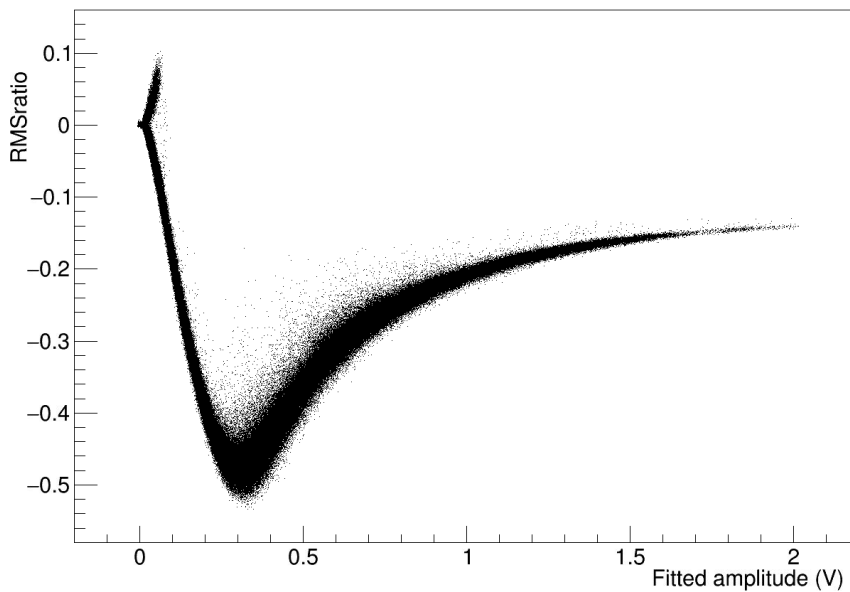


Figure 3.9: RMSratio parameter distribution as a function of the fitted amplitude for detector VK27.

The values of this new parameter will approach to  $-1$  for pulses originate by an absorber interaction while it will verge on  $+1$  if the fitted pulses correspond to carrier events. When the two RMS values are comparable  $\text{RMSratio} \simeq 0$ , meaning that both the templates are an equally good (or bad) description of the pulse and resulting in an overlap of absorber and carrier events. This effect arise when the pulse is small and the RMS is dominated by the influence of the baseline noise rather than by the impact of the pulse shape.

The values of this new parameter should approach to  $-1$  for pulses that originate by an absorber interaction while it should converge to  $+1$  if the fitted pulses correspond to carrier events. When the two RMS values are comparable  $\text{RMSratio} \simeq 0$ , meaning that both the templates are an equally good (or bad) description of the pulse and resulting in an overlap of absorber and carrier events. This effect arises in two cases: when the pulse is small and the RMS is dominated by the influence of the baseline noise rather than by the impact of the pulse

shape and when the pulse is higher than the truncation limit and the upper part of the pulse is not included in the fit procedure. Therefore the truncated fit procedure cause the RMSratio parameter to never reach the asymptotic values  $+1$  and  $-1$  as shown in figure 3.9, where the RMSratio parameter distribution as a function of the fitted amplitude is shown for detector VK27.

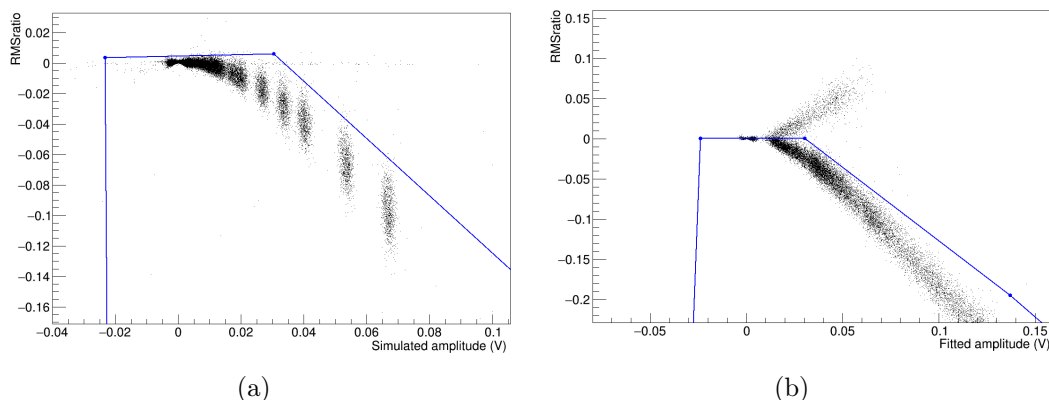


Figure 3.10: Distribution of the RMSratio variable as a function of the simulated amplitude for absorber events 3.10(a) and as a function of the fitted amplitude from the real data 3.10(b) for detector module VK27. In both plots the blue line is the graphical cut defined on the simulated events that selects only the absorber events.

To be able to study the RMSratio distribution of pure absorber events, simulated events were used. For the detailed description of the simulation process see section 3.8. The RMSratio cut defined with the simulated data to select only pure absorber events is then applied to the real (mixed) data allowing to remove the carrier events. The distribution of the RMSratio as a function of the simulated amplitude for absorber events of module VK27 is shown in figure 3.10(a) with the relative cut depicted by a blue line. Large values of the absolute value of the RMSratio parameter are not present in the simulated set. Considering that carrier events at higher amplitudes have been already removed by previous cuts, only events with amplitude  $< 0.1$  V have been simulated. Figure 3.10(b) is a zoom the low fitted amplitude region of figure 3.9 and shows the carrier events that are removed thanks to the RMSratio graphical selection. More precisely, the cut was initially built starting from the simulated amplitude distribution but then it was slightly lowered when applied on the real data. Applying the initial graphical in fact too many carrier events were surviving the selection. Therefore the top part of the cut was lowered to  $\text{RMSratio} = 0$  to increase the carrier events reduction and be more conservative. The value  $\text{RMSratio} = 0$  was chosen for the top part of the new graphical cut as this give a probability of 50% to reject/accept a carrier/absorber event due to noise fluctuations when approaching very low fitted amplitudes.

### 3.6.3 Coincidences cuts

The low interaction probability typical of dark matter particles leads us to discard events producing signals in more than one detector module. Similarly, signals coincident with muon veto hits are removed from the data set. Such rejections can be performed defining a time window in which coincident events are expected.

For what concerns muons, most of the triggers of the muon veto are due to natural radioactivity that cannot produce signals inside the detector volume. Therefore the majority of coincidences between the muon veto and a detector are random coincidences. Thus, the crucial point of this cut is the definition of a reasonable time window used to tag an event as real coincidence. Too long a time window would enormously reduce the exposure removing lots of good events because of random coincidences. On the contrary, if the time window is too short it cannot guarantee that all the real coincidences are rejected. The uncertainty due to the finite time resolution of the scintillation light signal in the muon veto panels is negligible with respect to the one of the cryogenic detector. Thus the value of the time window strongly depends on the precise determination of the time of the energy deposition in the cryogenic detectors. The detailed discussion on the time reconstruction presented in Ref. [111] leads to a muon coincidence window of  $\pm 2$  ms.

Regarding multiple detector modules signals, an analogous procedure was followed without any other consideration of the secondary pulse in the other detectors. A wider time window, equal to  $\pm 5$  ms, is used considering that the time of the energy deposition in *two* cryogenic detectors has to be determined.

### 3.6.4 Light Yield plot and $\eta$ factor

Once the process of event selection is completed, the final energy spectrum for both phonon and light channels can be produced following the procedure described in 3.3. The energy spectrum measured with the phonon detector for

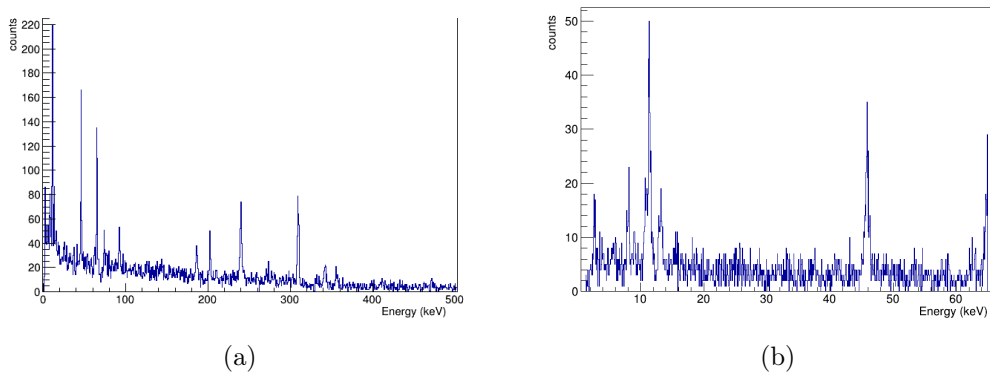


Figure 3.11: Energy spectrum measured with the phonon detector of module TUM29 with two different energy range: [0-500] keV in figure 3.11(a) and [0-65] keV in figure 3.11(b).

module TUM29 is shown in figure 3.11. Despite the absence of any source dur-

ing the collection of these data, some  $\gamma$  peaks are evident due to cosmogenic activation. Such  $\gamma$  peaks were studied for a TUM module<sup>5</sup> in Ref. [112]. Considering that the standard analysis process is optimised for low recoil energies, for all the channels the value of the CPE factor is corrected using the low-energy peak due to the cosmogenic activation of tungsten. Proton capture on  $^{182}\text{W}$  (and a successive decay) can result in  $^{179}\text{Ta}$  (via the reaction  $^{182}\text{W}(p, \alpha)^{179}\text{Ta}$ ) which decays via EC to  $^{179}\text{Hf}$  with a half-life of 665 d. The two peaks at 11.27 keV (L1-shell) and 10.74 keV (L2-shell) resulting from this process produce the observed peak at  $\sim 11$  keV (see figure 3.11(b)), that were used to perform an optimised low-energy calibration. The energy spectrum presented in figure 3.11 is obtained with the training set and due to the low statistics it is not possible to appreciate the two peaks separately.

As already presented in subsection 2.3.5, in order to proceed with the background discrimination the light yield variable has to be introduced:

$$\text{Light Yield} = \frac{E_l}{E_p} \quad (3.2)$$

where  $E_l$  and  $E_p$  are the energies detected by the light and the phonon channel respectively. The LY as a function of the phonon energy of events selected from the background training set is shown in figure 3.12(a). The peaks resulting from the cosmogenic activation processes are slightly tilted in the plane LY-Energy and this is the consequence of neglecting the amount of energy released in the light channel for the total incident energy estimation. In fact, since more than 90% of the total energy deposited inside the main absorber is converted into thermal excitation, the phonon signal is considered (in first approximation) a measure of the energy of the incoming particle (see subsection 2.3.4). However, this approximation leads to an underestimation of the real energy deposited in the crystal because the small fraction of the total energy emitted as scintillation light is neglected. Moreover the way the total energy deposited in the crystal is shared between the heat and light fluctuates making the two channels anti-correlated for a fixed incident energy. In the assumption of no energy losses, the total energy  $E$  deposited in the crystal is given by the sum of the energies deposited in the phonon and light channel. Introducing the scintillation efficiency  $\eta$ , that quantify the fraction of energy going into light production, the total energy  $E$  can be written as:

$$E = \eta E + (1 - \eta) E = \eta E_l + (1 - \eta) E_p \quad (3.3)$$

where the second equality is possible because of the adopted calibration procedure. In fact the calibration of the phonon (light) channel via the CPE factor implicitly assumes that a certain fraction of the total energy is deposited in the scintillation (heat) channel. Expressing  $E_l$  in terms of the LY variable the

---

<sup>5</sup>TUM modules are the ones for which the crystal has been grown in the laboratory of the Technische Universität München (TUM).

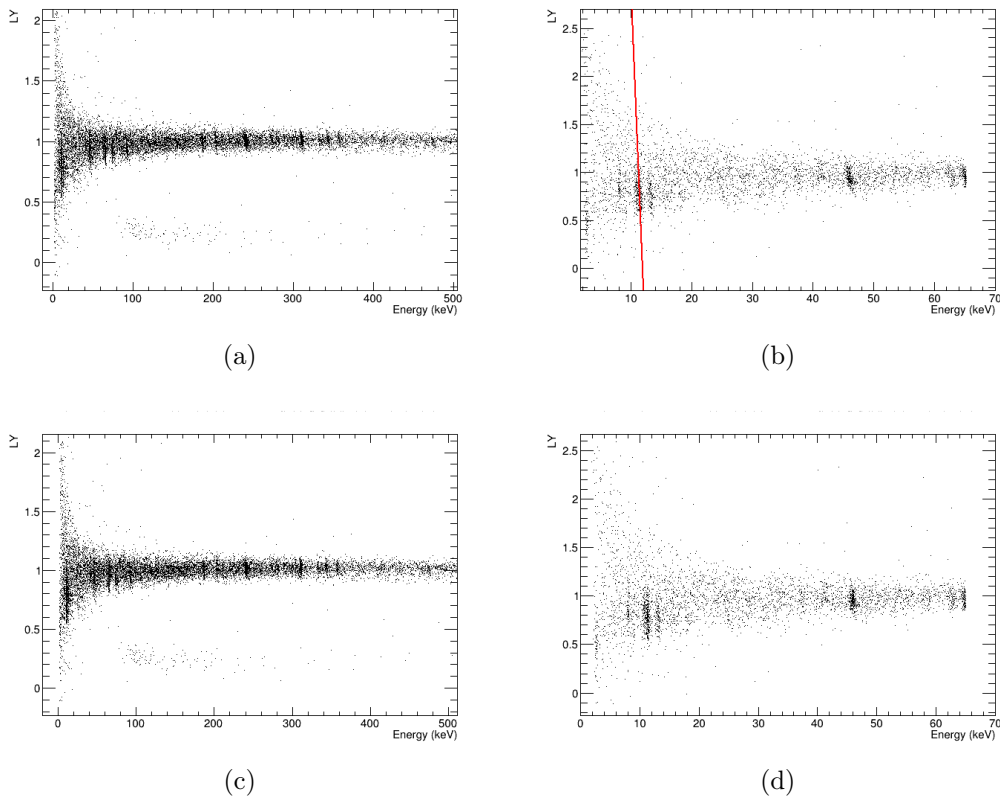


Figure 3.12: LY-energy plane obtained with training set of the phonon detector of module TUM29. The energy region needed for the iDM analysis is shown in figure 3.12(a). A zoom of the low energy region is shown in figure 3.12(b) where the red line correspond to the 11 keV  $\gamma$  line tilted. The effect of the iterative procedure involving the  $\eta$  parameter and the CPE factor redefinition is shown in figure 3.12(c) and 3.12(d) for the two energy region.

following formula is obtained:

$$E = [1 - \eta(1 - LY)] E_p \quad (3.4)$$

that allows to correct for the tilt. For each detector module the  $\eta$  parameter was determined minimising the width of the  $\gamma$  peak at 11 keV. In figure 3.12(b) the low energy region is presented with the line describing the tilt of the 11 keV  $\gamma$  line. To optimize the energy reconstruction at low energy, the standard analysis procedure uses the  $\eta$  corresponding to the tilt of such line to correct all the energies. Since the fine adjustment of the CPE factor and the  $\gamma$  lines tilt are closely linked to each other, the two process were repeated iteratively until their effect were no more appreciable. In figures 3.12(c) and 3.12(d) the LY plot was obtained after all these correction is shown. A residual tilt can be appreciated in the other  $\gamma$  lines present in the plots of figures 3.12(c) and 3.12(d) and this is due to the fact that the scintillation efficiency is dependent on the incident energy. Nonetheless, the effect of this dependence is very small in the energy

range considered for the standard analysis<sup>6</sup> and therefore a correction with a constant  $\eta$  factor is performed as standard procedure. To further improve the high energy analysis, an energy dependent eta factor should be implemented (see 6).

Besides the CPE factor low energy optimisation and the correction of the  $\gamma$  lines tilt, another feature of the  $\gamma$  lines can be noticed in the plot of figure 3.12(d): they are not centered with respect to the electron/ $\gamma$  band. The reason lies in the different interaction properties for  $\gamma$ s and electrons. Electrons interact directly with electrons of the target crystal while  $\gamma$ s have to produce electrons that in turn will interact with the electrons of the absorber. In this process the energy of the incident  $\gamma$  is shared among several electrons whose individual energy is lower than the total deposited energy. These low-energy electrons are affected by the non-proportionality effect [113, 114] leading to an overall light output for  $\gamma$ s lower than the one of electrons of the same energy.

### 3.7 Neutron calibration data

Neutrons induce both nuclear and electron/ $\gamma$  recoils thus populating both the bands in the LY-Energy plane. For this reason such data can be used to verify the effect of the event selection procedure illustrated in the previous sections. In

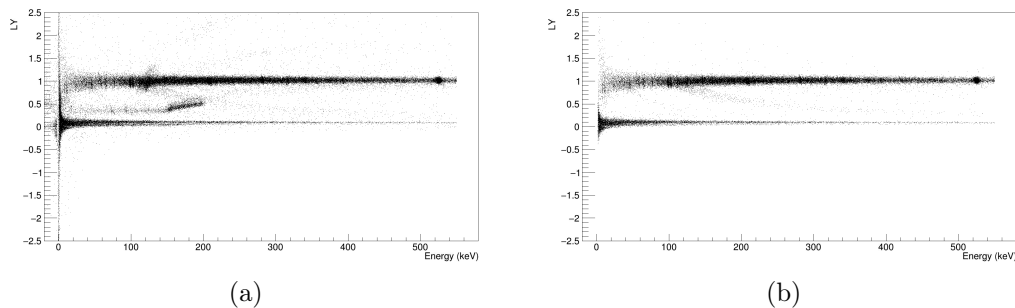


Figure 3.13: Effect of the raw data analysis on the neutron calibration data set. LY-energy plot with no cut and with all the cuts applied are shown in figure 3.13(a) and 3.13(b) respectively for module TUM29.

figure 3.13 the effect of the raw analysis can be appreciated for module TUM29. On the left, figure 3.13(a) shows the LY plot obtained with the raw data from the neutron calibration campaign performed with an AmBe source. On the right, figure 3.13(b), the LY plot obtained with the neutron calibration data that passed the event selection defined on the background training set is shown.

<sup>6</sup>The energy range for CRESST standard analysis was from threshold up to 40 keV up with CRESST-II detectors [3] and it was restricted from threshold up to 16 keV with CRESST-III detectors [76].

### 3.8 Cut Efficiency

Despite having verified the effect of the event selection procedure realized with the training set of the background data set applying it on the neutron calibration data, a proper estimation of the efficiency of these cuts is mandatory. The method adopted in this analysis for the cut efficiency determination was first used in Ref. [105] and consists of applying all the created cuts on a set of simulated signals. In this way the efficiency of a specific cut is provided by the ratio between the events surviving the cut and the simulated events. In order to obtain information on the energy dependence simulated pulses of different amplitudes are created superimposing empty baselines on the template of the event type to be simulated. Since empty baselines are affected by any possible artifact in the same manner as an event induced by a particle interaction, this method provides a profound basis for a precise determination of cut efficiencies.

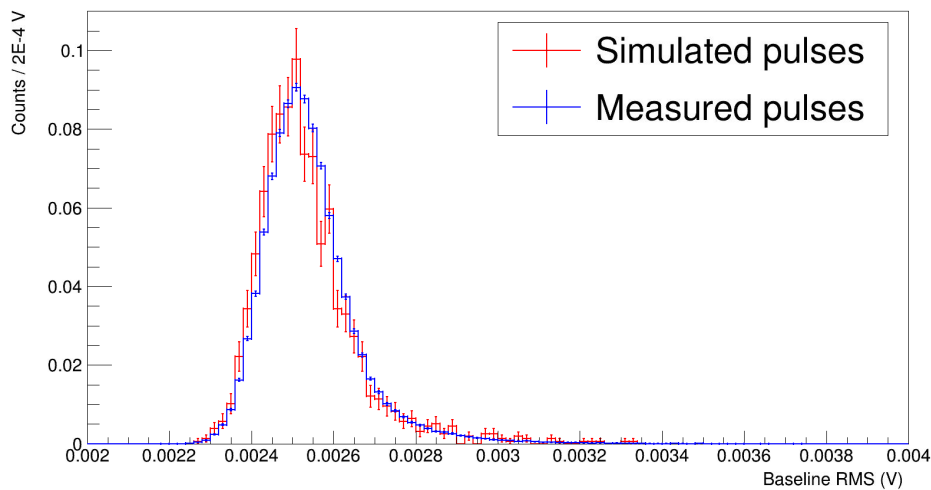


Figure 3.14: Normalised distribution of the baseline RMS for simulated pulses (red line) and measure pulses (blue line). The error bars associated to each bin correspond to the Poissonian error.

To verify the noise contribution of the simulated pulse introduced by the empty baselines is realistic, the baseline RMS of the simulated pulses has been compared with the one of the measure pulses. The baseline RMS correspond to the root mean square of the first 50 samples of the acquired time window. In figure 3.14 the normalised baseline RMS distributions for simulated pulses (red line) and measured pulses (blue line) surviving all the selections are presented. Poissonian error bars are associated to each bin. The distribution of the simulated pulses presents error bars larger than the measured pulses because of the statistics.

As the final goal of this analysis is to set an exclusion limit on the scattering cross-section, being conservative is a priority. Thus simulated events of recoils off tungsten are used for the cut efficiency determination. Tungsten in fact is the main target considered for probing the inelastic scenario. Additionally, tungsten has the smallest QF, namely recoils off tungsten will produce the smallest light

signal possible in the CRESST target for a given energy and therefore this class of events has the most critical cut efficiency.

Considering in first approximation a linear relation between the deposited energy and the resulting amplitude pulse, the proportionality factor is determined for each channel with a linear fit on the energy as a function of the fitted amplitude using the training set of the background data set. The simulated phonon pulse corresponding to a given deposited energy is created by scaling the template with the inverse proportionality factor and adding the result to the empty baseline. For the creation of the simulated light pulse, the quenching has to be considered: the template is scaled with the inverse of the product of the proportionality factor and the tungsten QF and then added to the empty baseline.

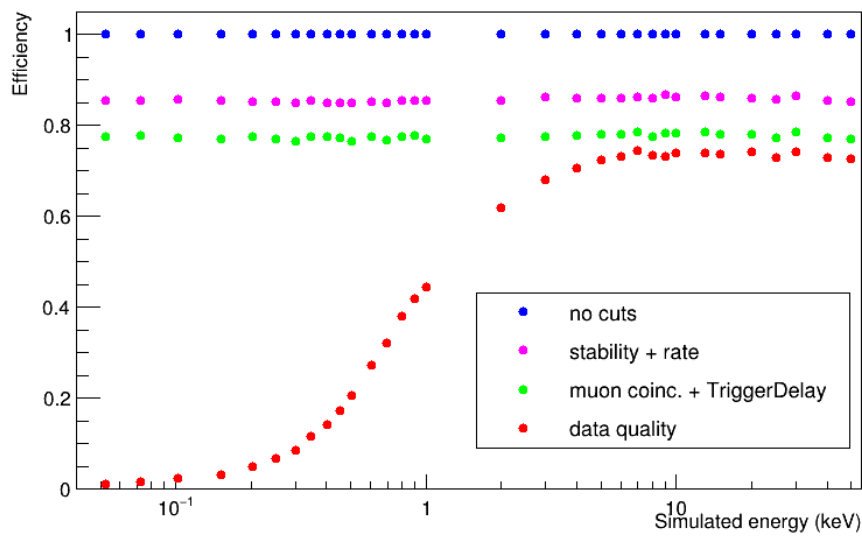


Figure 3.15: Cut efficiency plot for module TUM29. The efficiencies of some selections are shown with different colors, explained by the legend.

The efficiency of the various selections applied to the data are shown in figure 3.15. As expected the selections not relying on the pulse shape show no energy dependence. On the contrary a clear energy dependence is present for the data quality cuts: their efficiency gets lower for lower energies. For energies above  $\sim 10$  keV an approximately constant efficiency is shown.

### 3.9 Trigger Threshold

As already mentioned several times, CRESST standard analysis is optimised for the low-energy region for which a precise knowledge of the trigger threshold is crucial. Small pulses, closely spaced in amplitude, are injected in the TES heater to scan a voltage range around the set hardware threshold. The trigger efficiency for a given injected amplitude is then defined as the fraction of the injected heater pulses with that amplitude causing a trigger. To measure the trigger threshold efficiency as a function of the injected amplitudes for all the detector modules an

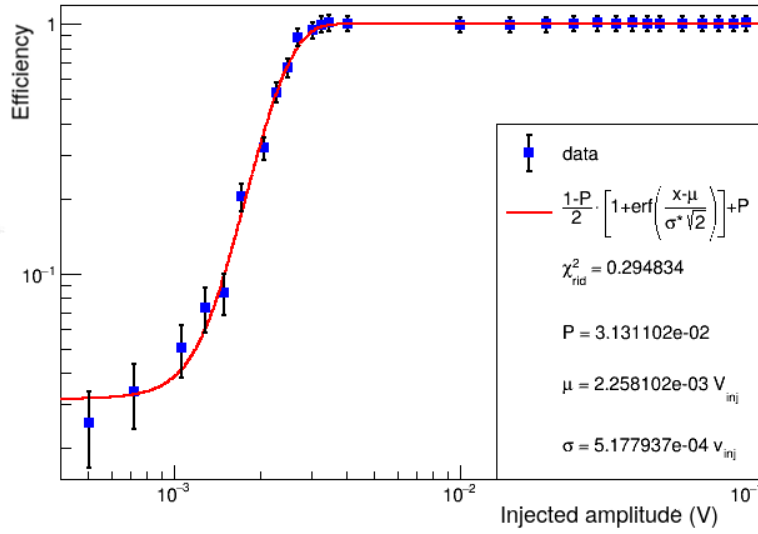


Figure 3.16: Trigger threshold efficiency for module VK34.

automatic process cycling the injected pulses periodically has been used. Therefore, in addition to the small pulses, also pulses of 10 V amplitude have been injected as a reference of the number of injected pulses considering that they will never be missed by the trigger. The probability for a given injected pulse to fire the trigger is binomial while the number of triggered events is Poissonian distributed. During the dedicated measurements for the trigger threshold determination only the number of triggered pulses has been recorded for each injected volt: no information about the real number of injected pulses for each amplitude has been stored. With these information, the trigger efficiency is obtained as the ratio of two measured values: the number of triggered pulses at a certain amplitude divided by the number of triggered pulses injected at 10 V. Consequently the error associated to the efficiency is given by the propagation of the error of the two Poissonian numbers and it is not binomial.

The theoretical description of the trigger efficiency as a function of injected amplitude for a real detector is given by the convolution of a step-function, corresponding to the ideal trigger, with a Gaussian function (of width  $\sigma$ ) accounting for the finite baseline noise. The resulting formula is:

$$f(A_{inj}) = \frac{1}{2} \cdot \left[ 1 + \operatorname{erf} \left( \frac{A_{inj} - Thr}{\sqrt{2}\sigma} \right) \right] \quad (3.5)$$

where  $A_{inj}$  is the injected amplitude,  $Thr$  is the threshold, defined as the amplitude where 50% of the injected pulses cause a trigger, erf denotes the Gaussian error function and  $\sigma$  is the resolution of the trigger. However random coincidences between an injected pulse firing the trigger and a particle interaction causing a trigger in a time window of 0,4 s are possible. Due to the trigger logic described in 2.5.3, the signal due to the coincident particle interaction will be recorded and flagged as injected pulse. The consequence of this is the presence of a pedestal  $P$  and the trigger efficiency formula has to account for it to have a

correct estimation of the efficiency. Imposing that the trigger efficiency function asymptotically approaches  $P$  for  $A_{inj} \ll Thr$  and to 1 for  $A_{inj} \gg Thr$  results in the following equation:

$$f(A_{inj}) = \frac{1 - P}{2} \cdot \left[ 1 + \operatorname{erf} \left( \frac{A_{inj} - Thr}{\sqrt{2}\sigma} \right) \right] + P. \quad (3.6)$$

Such equation has been used to perform a likelihood fit of the measured data with  $Thr$ ,  $\sigma$ ,  $P$  as free parameters. A dedicated measurement of the trigger threshold efficiency with the relative fit has been performed for all the detector modules. In figure 3.16 the measured trigger threshold efficiency plot and the associated fit are shown.



## Band fit

As already discussed in subsection 2.3.5 the LY variable is the key to discriminating between signal and background events. The description for the distribution of these events in the LY-energy plane is essential to proceed with such discrimination. However, due to analytical and numerical reasons, the parametrization of the bands, developed in Ref. [115], is performed in the Light-Energy plane. In this chapter the parametrization of these distributions is described and the final result of the likelihood fit of the bands optimised for the inelastic analysis is shown. The detailed description of the likelihood method will be given in the next chapter (5).

### 4.1 Energy resolution

The width of the bands is dominated by the resolution of the light detector but also the finite resolution of the phonon detector has some impact. It mainly depends on the finite baseline noise and therefore it is evaluated by fitting the distribution of the amplitudes of events from the lowest TP (TPA = 0.025 V) with a Gaussian. More precisely, the equivalent TPA amplitudes have been used for this procedure so that the width of the distribution should only be affected by the baseline noise. From the mean value  $\mu^{fit}$  and the standard deviation  $\sigma^{fit}$  obtained by the fit the baseline noise contribution to the energy resolution  $\sigma_{BLN}$  can be obtained with the following formula:

$$\sigma_{BLN}(keV) = CPE(keV/V) \cdot TPA(V) \cdot \frac{\sigma^{fit}(V)}{\mu^{fit}(V)}. \quad (4.1)$$

Regarding the light detector, its resolution does not depend only on the finite baseline noise and a more detailed discussion of the light resolution will be given in 4.2.2. Despite this, the finite baseline noise contribution to the light detector resolution can be obtained with the same method just presented for the phonon detector.

## 4.2 Electron/Gamma Band

Most of the events recorded during the background data taking are electrons and  $\gamma$ s originating from radioactive decays due to the irreducible intrinsic radioactivity of the detector components.

### 4.2.1 Mean line

Because of the calibration procedure extensively described in the previous chapter (3) the electron/ $\gamma$  band has a mean line at  $LY \simeq 1$  resulting in a linear relation between light (L) and energy (E). Two additional considerations are necessary to obtain a proper description of the mean line of the band. Firstly, the scintillator response as a function of the deposited energy is not perfectly linear and small deviations must be allowed. Secondly, at lower energies a saturation effect known as scintillator non-proportionality bends the electron band towards lower light yields [113] [116]. The resulting mean line of the electron band is parametrized by the following equation:

$$L_{e^-}(E) = (L_0 E + L_1 E^2) \left[ 1 - L_2 \exp\left(-\frac{E}{L_3}\right) \right]. \quad (4.2)$$

The  $L_0$  parameter is the proportionality factor and it is usually close to 1 by calibration. The  $L_1$  parameter accounts for small deviations from the linear behaviour. The term enclosed in square brackets describe the band bending due to the non-proportionality effect: the  $L_2$  parameter quantifies the strength of such an effect while the  $L_3$  parameter describes the curvature of the downward bending.

For what concerns the  $\gamma$  band mean line, the different behaviour of  $\gamma$ s with respect to electrons when interacting with the crystal has to be considered. As described in subsection 3.6.4,  $\gamma$ s produce multiple secondary electrons with individual energies lower than the initial photon and, due to the non-proportionality effect of the scintillation mechanism, the light output of  $\gamma$ s is lower than that of the electrons. The consequent slight quenching associated to the  $\gamma$  band is obtained by evaluating the electron mean line at a lower energy with the following equation:

$$L_\gamma(E) = L_{e^-}(E [Q_{\gamma,1} + EQ_{\gamma,2}]) \quad (4.3)$$

in which  $Q_{\gamma,1}$  and  $Q_{\gamma,2}$  are the parameters of the linear dependence of the  $\gamma$  quenching.

### 4.2.2 Width

As already discussed in section 4.1, both phonon and light detectors have a finite resolutions that determine the width of the bands. Since the phonon signal is stronger compared to the scintillation light signal, the resolution of the phonon detector usually is much better. Therefore, the width of the bands is described in terms of light using a Gaussian function whose mean value is given by equation

4.2 and 4.3. The width of the bands  $\sigma_L$  is due to 3 main effects [117]: uncertainties due to baseline noise in the light detector, fluctuations on the number of produced scintillation photons due to the finite energy required to produce a single photon, additional light energy dependent uncertainties. To consider all these effects, the total resolution of the light detector is described by the following equation:

$$\sigma_L(L) = \sqrt{\sigma_{L,0}^2 + S_1 L + S_2 L^2} \quad (4.4)$$

where  $\sigma_{L,0}$  is the baseline noise contribution to the light output uncertainty,  $S_1$  is the linear term accounting for the fluctuations on the number of produced scintillation photons and  $S_2$  is a quadratic term introduced to consider any other possible uncertainties.

Even if the contribution of the phonon detector resolution  $\sigma_P$  is small compared to that of the light detector, it cannot be neglected. A finite phonon resolution  $\sigma_P$  leads to an uncertainty on the reconstructed energy that would result in bands of finite width in the LY-energy plane even in case of an ideal light detector. Therefore, the following parametrization has been implemented for the total phonon detector resolution:

$$\sigma_P(E) = \sqrt{\sigma_{P,0}^2 + \sigma_{P,1} E}. \quad (4.5)$$

with  $\sigma_{P,0}$  and  $\sigma_{P,1}$  the two terms of a general linear dependence. Considering that the width of the band is described in terms of light, the phonon resolution does not directly affect it. To estimate the contribution of the phonon resolution it has to be scaled with the slope of the corresponding band at that point.

$$\sigma_x = \sqrt{\sigma_L(L) + \frac{dL_x}{dE}(E) \sigma_P(E)} \quad (4.6)$$

where  $L_x(E)$  is the mean line function of the corresponding band.

### 4.2.3 Excess light events

Another feature of the electron/ $\gamma$  band is represented by the the so-called ‘‘excess light events’’. These events appear mostly at low energies and show a light yield higher than the average one of electrons and gammas of the same energy. They might arise from electrons which produce additional scintillation light in the foil of the module housing before they are absorbed in the detector crystal [111]. The parametrization adopted to describe the distribution of these events, developed in Ref. [115], is the following:

$$\rho_{excess}(E, L) = A_{excess} \exp\left(-\frac{E}{\lambda_{excess}}\right) \cdot \left\{ \frac{1}{2\Delta_{excess}} \exp\left(-\frac{L}{\Delta_{excess}} + \frac{(\sigma_{L,e})^2}{2\Delta_{excess}^2}\right) \cdot \left[1 + \operatorname{erf}\left(\frac{L}{\sqrt{2}\sigma_{L,e}} - \frac{\sigma_{L,e}}{\sqrt{2}\Delta_{excess}}\right)\right] \right\} \quad (4.7)$$

where  $\sigma_{L,e}$  is the short version of the resolution of the detector at the mean line of the electron band  $\sigma_L [L_e(E)]$  and the explanation of the other symbols will follow in few lines. The derivation of this formula is completely empirical. To describe how the distribution of these events varies with energy an exponential function starting at zero energy and decreasing with increasing energies is used. The event distribution along the light axis is described by an exponential decay that starts at the mean line of the electron band and is convolved with a Gaussian function to account for the detector resolution. Therefore  $A_{excess}$  and  $\lambda_{excess}$  denote respectively the amplitude and the decay length of the exponential decrease along the energy axis and  $\Delta_{excess}$  is the decay length of the exponential decay along the light axis.

### 4.3 Nuclear recoil Band

As already introduced in subsection 2.3.5 nuclear recoils emit much less scintillation light than electromagnetic interactions of the same energy. CRESST targets contain three different atoms and therefore three nuclear recoil bands have to be considered. Compared to the electron/ $\gamma$  band, two are the main differences that characterize the nuclear recoil band shape. Firstly, they do not show any non-proportionality bending. Secondly, the dedicated measurement reported in Ref. [106] shown a clear energy dependence of the QFs. More precisely these measurements highlighted such that energy dependence is the same for each detector by a scaling factor, individual for each detector, is introduced. The consequent parametrization of the nuclear recoil band mean line uses the electron band mean line, without the non-proportionality correction, multiplied by the energy dependent quenching-factor and the detector scaling factor  $\epsilon$ . The resulting mean line can be written as:

$$L_x(E) = (L_0E + L_1E^2) \cdot \epsilon \cdot QF_x \cdot \left[ 1 + f_x \exp\left(-\frac{E}{\lambda_x}\right) \right]. \quad (4.8)$$

where  $x$  denote the chemical element of the corresponding band,  $L_0$  and  $L_1$  are the parameters of equation 4.2 and the three parameters  $QF_x$ ,  $f_x$  and  $\lambda_x$  describe the QF energy dependence. This description of the QFs energy dependence, developed in Ref. [115], is needed to use a quenching factor as basis of the energy dependent description of the band. The values of  $QF_x$ ,  $f_x$  and  $\lambda_x$  parameters have been measured [106] and are reported in table 4.1.

For these bands, the resolution of the detectors is applied in the same way as for the electron band, with the usual analytical derivation  $dL_x/dE$  as slope.

### 4.4 Energy spectra

In order to have a complete description of the distribution of signal and background events in the energy-light yield plane, a parametrization of the energy spectra  $dN/dE$  of all the events populating each band is required. A theoretical

Element	QF <sub>x</sub>	f <sub>x</sub>	λ <sub>x</sub>
O	0.0739 ± 0.000019	0.7088 ± 0.0008	567.1 ± 0.9
Ca	0.0556 ± 0.00073	0.1887 ± 0.0022	801.3 ± 18.8
W	0.0196 ± 0.0022	0	∞

Table 4.1: Measured values of the QF energy dependence parameters for Oxygen, Calcium and Tungsten [106].

description of the energy spectra has been adopted when possible while a phenomenological approach has been used for the others spectra. The theoretical derivation does not account for the finite energy resolution of the phonon detector  $\sigma_P$  thus a convolution with a Gaussian function of width equal to  $\sigma_P$  has to be done. For the phenomenological spectra instead in first approximation the convolution would not produce an appreciable effect. Finally, before performing the likelihood fit of the bands, the cut efficiency is applied to all spectra to account for the effect of the raw analysis.

The differential recoil rate of the excess light events has already been provided in subsection 4.2.3 therefore the spectra of the electron-, gamma- and neutron-backgrounds as well as a description for the dark matter signal and the signal of the neutron calibration have to be obtained.

#### 4.4.1 Electron rate

From the observed data the following formula has been derived for the energy spectrum of the electron band:

$$\frac{dN_e}{dE} = P_0 + P_1 E + F_e \exp\left(-\frac{E}{D_e}\right). \quad (4.9)$$

The linear term, whose parameters are  $P_0$  and  $P_1$ , well describes the observed data over a wide energy range. However, many detectors exhibit a sharp increase in events at the lower end of their detection range and the exponential decaying term, with  $F_e$  as amplitude and  $D_e$  as decay constant, has been introduced to account for this effect. The hypothesis that this increase in the rate of observed events at low energy may have originated from dark matter has been ruled out. In case of a dark matter signal, the energy dependence should be always the same for all the detectors, but this does not correspond to the observed data. In addition to the continuous spectrum described in equation 4.9, also the presence of possible peaks due to  $\beta + \gamma$  decays, has to be included in the electron rate parametrization. In first approximation, the  $\beta + \gamma$  peaks are described with the convolution of a triangular function  $\mathcal{T}$  with a normalised Gaussian function  $\mathcal{G}$ :

$$\frac{dN_{\beta\gamma,x}}{dE} = \mathcal{G}(E, \sigma_P(E)) * [C_{\beta\gamma,x} \mathcal{T}(E, E_{\beta\gamma,x}^0, Q_{\beta\gamma,x})] \quad (4.10)$$

where the  $x$  index denotes the individual  $\beta + \gamma$  peak, the  $*$  denotes the convolution operation,  $C_{\beta\gamma,x}$  is the number of events in the considered  $\beta\gamma$  peak,  $E_{\beta\gamma,x}^0$  is the

energy corresponding to the maximum of the peak and  $Q_{\beta\gamma,x}$  is the Q-value of the  $\beta + \gamma$  process. The width of the Gaussian function is equal to  $\sigma_P$  to account for the finite energy resolution of the phonon detector. The triangular function is normalised and its explicit expression follows:

$$\mathcal{T}(E, E_{\beta\gamma,x}^0, Q_{\beta\gamma,x}) = \frac{2}{E_{\beta\gamma,x}^0 Q_{\beta\gamma,x}} \begin{cases} E_{\beta\gamma,x}^0 - \frac{E_{\beta\gamma,x}^0}{Q_{\beta\gamma,x}} (E - E_{\beta\gamma,x}^0) & \text{if } E_{\beta\gamma,x}^0 < E < E_{\beta\gamma,x}^0 + Q_{\beta\gamma,x} \\ 0 & \text{otherwise} \end{cases} \quad (4.11)$$

with  $2/(E_{\beta\gamma,x}^0 Q_{\beta\gamma,x})$  normalization factor of the triangle.

#### 4.4.2 Gamma rate

Irreducible intrinsic radioactivity of the detector modules components leads to the presence of  $\gamma$  peaks in the total measured energy spectrum. The energy of these events should correspond to the characteristic energies of the associated radioactive decays with a possible small deviation from the theoretical value due to the resolution of the phonon detector. Therefore each peak is described with a Gaussian function with the peak position  $M_x$  as mean and the phonon resolution evaluated at that energy  $\sigma_P(M_x)$  as its width. The resulting parametrization of each  $\gamma$  peak is given by:

$$\frac{dN_{\gamma,x}}{dE} = \frac{C_{\gamma,x}}{\sqrt{2} * \pi \sigma_P(M_x)} \exp\left(-\frac{(E - M_x)^2}{2(\sigma_P(M_x))^2}\right) \quad (4.12)$$

where x denotes the individual  $\gamma$  peak decay and the parameter  $C_x$  accounts for the number of events populating such peak.

#### 4.4.3 Neutron rate

Both the rate of the neutron calibration signal and that of the neutron background are modeled as an exponentially decreasing function:

$$\frac{dN_{n,x}}{dE} = A_{n,x} \exp\left(-\frac{E}{E_{n,x}^{decay}}\right) \quad (4.13)$$

with  $A_{n,x}$  and  $E_{n,x}^{decay}$  being the amplitude and the decay constant relative to neutrons scattering off the x target nucleus. Since the number of expected neutron background events in the measured data is very small, usually less than 0.1 events per kg d of measurement data, it is not possible to determine the decay constant from the background data set. Therefore, the energy dependence is determined with the neutron calibration data and then it is used also for the background data. The very small statistics of the background data set allow this approximation, even if in principle the two energy spectra can be very different from each other. The background neutrons in fact are a mix of source-like and muon-induced neutrons while the neutron calibration data are produced by an

AmBe source. In the case of the amplitudes  $A_{n,x}$ , they are determined separately for each data set. To avoid an overestimation of the neutron background, the number of events is linked to the expected number of neutron events via a Poisson distribution. This measure has been adopted because an overestimation of the neutron background would reduce the number of events identified as dark matter interactions and lowering the exclusion limit.

#### 4.4.4 DM rate

The expected energy spectrum for inelastic dark matter is given by equation 1.9 while equation 1.17 gives the expected energy spectrum for the standard scenario of elastic dark matter. As discussed in subsection 1.3.1 only iDM interactions are considered for this analysis. However, both two expected spectra do not account for the performance of the real detector, in particular its energy resolution and threshold. The threshold of the detector in fact limits the smallest signal the detector can measure. The finite energy resolution introduces an uncertainty in the measured energy because of which, true energies below the threshold can also be detected. This is taken into account by numerically convolving the expected DM energy spectrum with a Gaussian function with a width equal to the detector energy resolution  $\sigma_P$ , and considering recoil energies down to six times the resolution  $\sigma_P$  away from the threshold. Since calculating the numerical convolution for every data and integration point is very time consuming, the dark matter spectra are pre-calculated for a number of points and then a spline interpolation of order 4 is used to approximate the spectrum. In total 1000 points are used in this interpolation and the density of points is higher for lower energies since the spectrum displays sharper features in that region.

### 4.5 Density Functions

Before proceeding with the likelihood fit of the bands, the distribution of functions  $\rho_x$  of the individual class of events has to be constructed. The distribution of the excess light events have already been introduced in 4.2.3. The distribution of all the other event classes consists of a normalized Gaussian function centered in the corresponding mean line  $L_x$  and with the width equal to  $\sigma_x$  multiplied by the associated energy spectrum  $dN_x/dE$ . In this way both the energy dependence of the emitted light and the expected number of events are described for each class of events and the resulting formula is:

$$\rho_x(E, L) = \frac{dN_x}{dE}(E) \cdot \frac{1}{\sqrt{2\pi}\sigma_x(E)} \cdot \exp\left(-\frac{[L - L_x(E)]^2}{2\sigma_x^2(E)}\right) \quad (4.14)$$

where  $x$  denote the event class of the density function. All the density functions needed to fully describe the events present in a light-energy plot are listed:

- $\rho_e$  for the electron background

- $\rho_\gamma$  for the  $\gamma$  background
- $\rho_{nb}^X$  for the neutron background scattering off nucleus  $X$
- $\rho_{ns}^X$  for the neutron signal scattering off nucleus  $X$  (neutron calibration data)
- $\rho_\chi^X$  for the DM signal scattering off nucleus  $X$

Using these density functions the two total density functions needed to describe events from neutron calibration data  $\rho_{ncal}$  and from background data  $\rho_{bck}$  can be obtained:

$$\rho_{ncal} = \rho_e + \rho_\gamma + \rho_{ns} \quad (4.15)$$

$$\rho_{bck} = \rho_e + \rho_\gamma + \rho_{nb} + \rho_\chi \quad (4.16)$$

where  $\rho_{ns} = \rho_{ns}^O + \rho_{ns}^{Ca} + \rho_{ns}^W$ ,  $\rho_{nb} = \rho_{nb}^O + \rho_{nb}^{Ca} + \rho_{nb}^W$ , and  $\rho_\chi = \rho_\chi^O + \rho_\chi^{Ca} + \rho_\chi^W$ . In principle the density functions of neutron background  $\rho_{nb}$  and dark matter  $\rho_\chi$  should also be included in the total density function for the neutron calibration data set  $\rho_{ncal}$  but its exposure is very small and therefore both  $\rho_{nb}$  and  $\rho_\chi$  contributions can be neglected. The description of the band structure is the same in both density functions but the amplitude of the neutron spectrum of course varies between the two.

In Ref. [115] it has also been proved that using both data sets and thus both density functions improve the quality of the fit significantly. In general in fact, the background data set is characterised by very few events in the nuclear recoil bands and this would make the estimation of the bands parameters more difficult and weak. On the contrary, including the neutron calibration data populates the nuclear recoil bands leading to a better estimate of their parameters. In addition, the overall statistical significance is increased allowing a faster convergence of the fit routine [115].

## 4.6 Band fit results

The likelihood fit method will be discussed in detail in chapter 5; however band parameter estimations are reported in this section. The main purpose of the analysis presented in this work is to obtain the exclusion limit for the inelastic dark matter cross section and to compare it with the results presented in Ref. [1]. Therefore the band fit procedure has been optimised for the inelastic analysis considering recoil energies in the range [30, 500] keV. Moreover, the band fit is performed on the full data set to increase the statistics as much as possible and thus the fit convergence.

In figure 4.1 the result of the band fit for detector module Verena on the background and neutron calibration data is shown both in the Light-Energy (figure 4.1(a)) and in the LY-Energy plane (figure 4.1(b)). With solid lines the mean lines of electron-,  $\gamma$ -, Oxygen-, Calcium- and Tungsten- recoil bands are drawn with black, purple, red, pink and green color respectively. With the same

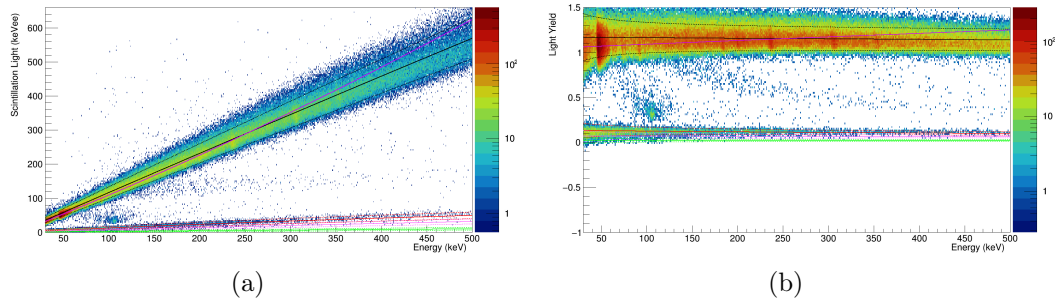


Figure 4.1: Results of the band fit for detector module Verena: on the left 4.1(a) in the Light-Energy plane while on the right 4.1(b) in the LY-Energy plane. Solid lines indicate the mean line of the band while the dashed lines indicate the 90% boundaries. The line colors denote the particle: black for electrons, purple for  $\gamma$ s, red for oxygen, pink for calcium and green for Tungsten. The number of events is indicated by the z axis.

color legend, the dashed lines outline for each band the 90% boundaries<sup>1</sup>, thus 80% of the events are expected in between. The number of events is indicated by the z axis.

There are two clear populations outside the band boundaries between the electron/ $\gamma$  band and the nuclear recoil band. The population at  $\sim 100$  keV is due to the Polonium decay from crystal surface contamination as already explained in subsection 2.3.5. The other population coming out of the electron/ $\gamma$  band at  $\sim 120$  keV corresponds to inelastic scattering of neutrons on Tungsten where the combination of a particle from the de-excitation of an excited W-energy level to the ground state and an elastic W-recoil is observed [106]. The most prominent inelastic excitation levels of the relevant W isotopes cluster between 100 keV and 120 keV. There are also less pronounced levels of W at lower and higher energies [118]. Such events are visible in the LY-Energy plane as curved bands below the electron-recoil band confirming its crystal origin. As treated in subsection 2.3.5 in fact, the distribution of this population means that the amount of energy detected by the phonon channel varies a lot suggesting the primary events happen inside the crystal.

Unfortunately the parametrization of these two population is not yet implemented in the fit software making them very dangerous for the goodness and the reliability of the fit results. The solution adopted for this analysis was to perform a first band fit with the both the neutron calibration and background data sets to estimate the parameters determining the band shapes, especially the  $\epsilon$  parameter for which the high statistics of the nuclear recoil band is crucial. After this fit, the  $\epsilon$  parameter was fixed and then a second band fit procedure was performed using only the background data set. From this second fit procedure a precise estimation of all the parameters describing both the band shapes and

<sup>1</sup>The boundary lines are set so that the upper (lower) boundary line split the events of the band in 90% below (above) and 10% above (below) the line.

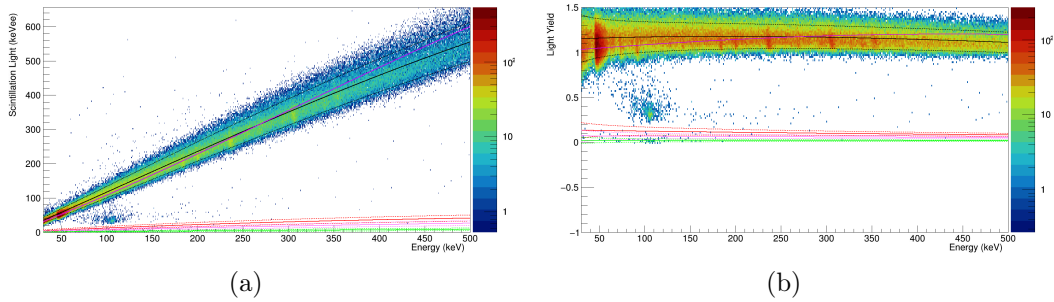


Figure 4.2: Result of the second band fit for detector module Verena with background data only. On the left 4.2(a) in the Light-Energy plane while on the right 4.2(b) in the LY-Energy plane. The legend is the same of figure 4.1.

the energy spectra is obtained.

In figure 4.2 the result of the second band fit performed only with the background data set is shown in the Light-Energy plane (figure 4.2(a)) and in the LY-Energy plane (figure 4.2(b)). The color legend is the same as figure 4.1.

The values of the parameters describing the bands shape obtained after both the likelihood fit (with and without the neutron calibration data) for detector module Verena are reported in table 4.2. The two parameters corresponding to the baseline noise of the light and phonon channels are marked with ( $\star$ ) because they are fixed and calculated as explained at the beginning of this chapter, in subsection 4.1. Despite this, they have been inserted in the table as they are key values for the shape of the bands. It is not very straightforward to associate an error to the parameters obtained by a likelihood fit. A possibility would be to use a Bayesian approach for which a Monte Carlo simulation is needed for each parameter resulting in a huge effort for which the standard analysis software is not ready. In addition this would not take into account the correlation between many parameters and would only cover the statistical uncertainty and not any systematics. Therefore all the numbers presented in table 4.2 have all the digits given by the output of the software used for the band fit and no error is reported. Despite the absence of the associated errors, the values of the parameters obtained including the neutron calibration in the fit are of the same order of magnitude of the ones obtained with only the background data set. The only significantly different parameter in the two cases is the  $L_3$  parameter that corresponds to decay constant of the non proportionality effect. This difference is mainly due to the huge difference in the statistics available for the two fit. In both cases the  $L_3$  parameter is very big and the  $L_2$  parameter very small meaning that the band bending is not very pronounced. Considering that this effect has been observed at low energies, the values of these parameters is in agreement with the considered data given the high energy range used for the fit. Summarising the general agreement between the two fit parameters and the fit results shown in figure 4.1 and 4.2 suggest that the adopted method has been appropriate.

Origin	Parameter	Value w/ NCal data	Value w/o NCal data
Electron band mean line	$L_0$	1.4558	1.53504
	$L_1$ (keV <sup>-1</sup> )	-8.06754e-5	-0.000658327
	$L_2$	0.196533	0.257597
	$L_3$ (keV)	100000.0	422.057
Gamma band mean line	$Q_{\gamma,1}$	0.896167	0.883973
	$Q_{\gamma,2}$ (keV <sup>-1</sup> )	0.000407667	0.000432054
Band width	$\sigma_{L,0}$ (keV)	0.281 (★)	0.281 (★)
	$S_1$ (keV <sub>ee</sub> )	0.896398	0.949102
	$S_2$	0.00525752	0.00463412
	$\sigma_{P,0}$ (keV)	0.103 (★)	0.103 (★)
	$\sigma_{P,1}$ (keV)	0.0145939	0.00941155
Excess light events	$A_{excess}$	2.93741	2.05405
	$\lambda_{excess}$ (keV)	376.927	324.012
	$\Delta_{excess}$ (keV <sub>ee</sub> )	236.324	203.519
Detector scaling factor	$\epsilon$	0.718116	0.718116

Table 4.2: Values of the band parameters for detector module Verena obtained by the likelihood fit with and without the neutron calibration data.



## Exclusion limit

### 5.1 Extended Likelihood function

The aim of a likelihood analysis is to build a complete, parametrized model including contributions from a potential signal and background.

The likelihood function of a set of parameters for a given model describes the plausibility that these parameters describe the given data. It is therefore strongly connected to the probability which describes the plausibility of an outcome for a given set of parameters. In probability theory this is called conditional probability and it is denoted with  $P(\mathbf{x} | \Theta)$ , where  $\mathbf{x}$  denotes the observed data and  $\Theta$  correspond to the set of parameters. With this notation the likelihood can be written as:

$$\mathcal{L}(\Theta | \mathbf{x}) = P(\mathbf{x} | \Theta) = \prod_{i=1}^N p(x_i | \Theta) \quad (5.1)$$

where  $N$  is the number of observed events and  $p(x_i | \Theta)$  is the probability density function associated to the data point  $x_i$  given the parameter set  $\Theta$ . The last equality is possible since the observed events are independent of each other. In this way the likelihood  $\mathcal{L}$  is the plausibility of  $\Theta$  for the given data set  $\mathbf{x}$ . Therefore the goal of a likelihood fit is to determine those values for the parameters  $\Theta$  which maximize the likelihood and, thus, provide the best possible agreement between the model and the measured data. It is important to underline that this procedure is possible if and only if  $p(x_i | \Theta)$  is normalised, otherwise the likelihood can increase indefinitely and the relative fit will never converge.

In some fields, however, normalised probability density functions are not available since the number of observed events is not fixed. Instead, it can fluctuate and it may even be relevant for the parameter estimation. In the CRESST analysis, for example, not only the shape of bands and spectra are important, but also the number of observed events is of course a relevant measurement. For this reason the description of measured data selected with the raw analysis is done in terms of density functions whose integrals over the acceptance region give the total number of expected events:

$$\mathcal{N}(\Theta) = \int_A \rho(\mathbf{x} | \Theta) d\mathbf{x} \quad (5.2)$$

where  $A$  denotes the acceptance region.

To deal with non-normalised density functions and their relative likelihood maximization, the so-called extended maximum likelihood (EML) must be used [119]. This extension of the likelihood formalism consists of including the number of expected events in the set of parameters used to maximize the likelihood. At the same time the EML allows a deviation between the number of expected events  $\mathcal{N}$  and the number of observed events  $N$ , since the latter will be subjected to the fluctuations of Poissonian statistics. Adding explicitly how the Poissonian statistics links  $\mathcal{N}$  and  $N$ , equation 5.1 become:

$$\mathcal{L}(\Theta | \mathbf{x}) = \frac{\mathcal{N}^N}{N!} e^{-\mathcal{N}} \prod_{i=1}^N p(x_i | \Theta) = \frac{e^{-\mathcal{N}}}{N!} \prod_{i=1}^N \mathcal{N} p(x_i | \Theta) = \frac{e^{-\mathcal{N}}}{N!} \prod_{i=1}^N \rho(x_i | \Theta) \quad (5.3)$$

where  $N$  is considered to be the outcome of a Poisson distribution with mean value equal to  $\mathcal{N}$ . The last equality results from considering that the non-normalised density function  $\rho(\mathbf{x} | \Theta)$  can always be seen as its integral (see equation 5.2) multiplied by a normalised standard probability. The factor  $N!$  is usually not present in the EML function as it accounts for the order of the points in the data set  $\mathbf{x}$  and this has no effect in the maximization of the likelihood. Therefore the final expression for the EML formula is:

$$\mathcal{L}^{ext}(\Theta | \mathbf{x}) = e^{-\mathcal{N}} \prod_{i=1}^N \rho(x_i | \Theta) \quad (5.4)$$

It is clear that the more the number of expected events deviates from the number of actual events in the data, the lower will be the value of the likelihood. In this way the number of expected events becomes to all effects a parameter that has to be adjusted to maximise the likelihood.

Finally the likelihood formalism allows to combine different data sets, a crucial point for experiments like CRESST, whose active volume consists of several almost independent detector modules. Combining data from different modules increases the exposure enlarging the accessible parameter space. The combination is performed by calculating the signal expectation as well as the expected background contribution for each individual data set obtaining a complete density function for each detector module. Then the total number of expected events  $\mathcal{N}^{tot}$  and the relative total likelihood function  $\mathcal{L}^{tot}$  are given by:

$$\mathcal{N}_{tot}(\Theta) = \sum_{d=1}^D \left[ \int_A \rho_d(\mathbf{x} | \Theta) d\mathbf{x} \right]$$

$$\mathcal{L}_{tot}^{ext}(\Theta | \mathbf{x}) = e^{-\mathcal{N}_{tot}(\Theta)} \prod_{d=1}^D \left[ \prod_{i=1}^N \rho_d(x_i | \Theta) \right]$$

### 5.1.1 Logarithmic Likelihood

In practice the likelihood fit is not performed by maximizing the likelihood  $\mathcal{L}^{ext}$ , but instead the quantity  $-\ln(\mathcal{L}^{ext})$  is minimized. Since the logarithm is a continuously increasing function, maximizing the logarithm of the likelihood is equivalent to maximizing the likelihood itself. Taking the negative logarithm turns the maximization into a minimization. This is indeed a practical advantage as optimizers in statistical packages usually work by minimizing the result of a function.

The main reason of this transformation is related to a basic property of the logarithm function itself: it can transform a product of densities into a sum. This property is extremely convenient for two main reasons. Firstly, the asymptotic properties of sums are easier to analyze by applying for example the Central Limit Theorem to the sum. Secondly, products are not numerically stable. In fact they tend to converge quickly to zero or to infinity, depending on whether the densities of the single observations are on average less than or greater than 1. On the contrary sums are more stable from a numerical point of view. This is extremely important as the maximum likelihood problem is often solved numerically on computers where limited machine precision does not allow one to distinguish a very small number from zero and a very large number from infinity.

### 5.1.2 Profile Likelihood

The set of parameters  $\Theta$  contains all the free parameters of the model presented in chapter 4. Among all of them there are three parameters that are the real goal of this analysis: the inelastic dark matter cross-section  $\sigma_\chi$ , the dark matter mass  $m_\chi$  and the dark matter mass splitting  $\delta$ . The other parameters that are not of primary interest are referred to as “nuisance” parameters and are indicated with  $\theta$  allowing us to write  $\Theta = (\sigma_\chi, m_\chi, \delta, \theta)$ . Under these conditions it is useful to reduce the dimensions of the parameter space by concentrating the likelihood function for a subset of parameters as this would reduce computational burden of the original maximization problem. The general procedure for the likelihood concentration consists in expressing the nuisance parameters as functions of the parameters of interest and replacing them in the likelihood function. The resulting likelihood, referred to as “profile likelihood”, allows us to reduce the computational burden of the original maximization problem, making it a powerful tool for next step of the analysis.

## 5.2 Calculating the exclusion limit

One of the most popular methods to build an exclusion limit employs the likelihood ratio as a test statistic. Due to the presence of nuisance parameters discussed in subsection 5.1.2, the profile likelihood ratio has been used as statistical test for this analysis. The purpose of this calculation is the exclusion limit for the iDM cross-section for a fixed value of  $m_\chi$  and  $\delta$  parameters. Then, changing the values of these two parameters, the curve of the cross-section exclusion

limit as a function of dark matter mass and splitting can be obtained. The test statistics expression is therefore:

$$\lambda(\sigma_\chi) = \frac{\mathcal{L}(\sigma_\chi, \hat{\boldsymbol{\theta}} | m_\chi, \delta, \mathbf{x})}{\mathcal{L}(\hat{\sigma}_\chi, \hat{\boldsymbol{\theta}} | m_\chi, \delta, \mathbf{x})} \quad (5.5)$$

where  $\hat{\sigma}_\chi$  and  $\hat{\boldsymbol{\theta}}$  are the values of the parameters that maximize the extended likelihood, from now on denoted with the  $\mathcal{L}$  for simplicity. The symbol  $\hat{\boldsymbol{\theta}}$  denotes the so-called profiled values of the nuisance parameters, that are the values that maximize the likelihood  $\mathcal{L}(\sigma_\chi, \boldsymbol{\theta} | m_\chi, \delta, \mathbf{x})$  for a specific value of  $\sigma_\chi$ . The test statistics associated to the profile likelihood ratio is defined as:

$$q_{\sigma_\chi} = \begin{cases} -2 \ln(\lambda(\sigma_\chi)) & \text{if } \hat{\sigma}_\chi > 0 \\ 0 & \text{if } \hat{\sigma}_\chi < 0 \end{cases} \quad (5.6)$$

where the case  $q_{\sigma_\chi} = 0$  if  $\hat{\sigma}_\chi < 0$  is needed to prevent the minimization process to find a negative value of the cross-section as best value. To quantify the level of agreement between the data and the hypothesized  $\sigma_\chi$ , the p-value for an observed value  $q_{\sigma_\chi, obs}$  is introduced:

$$p_{\sigma_\chi} = \int_{q_{\sigma_\chi, obs}}^{\infty} f(q_{\sigma_\chi, obs} | \sigma_\chi) dq_{\sigma_\chi} \quad (5.7)$$

where  $f(q_{\sigma_\chi, obs} | \sigma_\chi)$  is the probability density function of  $q_{\sigma_\chi, obs}$  assuming the value  $\sigma_\chi$  for the dark matter cross-section. By definition the p-value gives the probability of obtaining a value of  $q_{\sigma_\chi}$  equal to or larger than  $q_{\sigma_\chi, obs}$  in the assumption of dark matter cross-section equal to  $\sigma_\chi$ . The p-value then is usually converted into an equivalent significance  $Z$  defined so that a variable distributed according to a Gaussian with mean  $\mu$  and standard deviation  $Z$  and found at  $\mu + Z$  has an upper limit equal to the p-value itself. According to this definition the significance can be calculated with the following formula:

$$Z = \Phi^{-1}(1 - p) \quad (5.8)$$

where  $\Phi^{-1}$  is the inverse function of the cumulative distribution of the standard Gaussian.

The relation between the p-value and the observed  $q_{\sigma_\chi, obs}$ , and also with the significance  $Z$ , are illustrated in figure 5.1. In order to evaluate the p-value of equation 5.7 the distribution  $f(q_{\sigma_\chi, obs} | \sigma_\chi)$  is fundamental. As shown in Ref. [120] the approximate formula for such distribution can be derived using the results of Wald [121] and Wilks [122]. Thus, in the approximation of a single parameter of interest and large data sample size, the distribution of  $q_{\sigma_\chi}$  approaches a chi-square distribution for one degree of freedom<sup>1</sup>. Therefore the significance can be written as:

$$Z_{\sigma_\chi} = \sqrt{q_{\sigma_\chi, obs}}. \quad (5.9)$$

<sup>1</sup>The validity of this assumption has been verified in Ref. [115] but it should be verified also for the new fit considering the different data set and energy range used for this analysis.

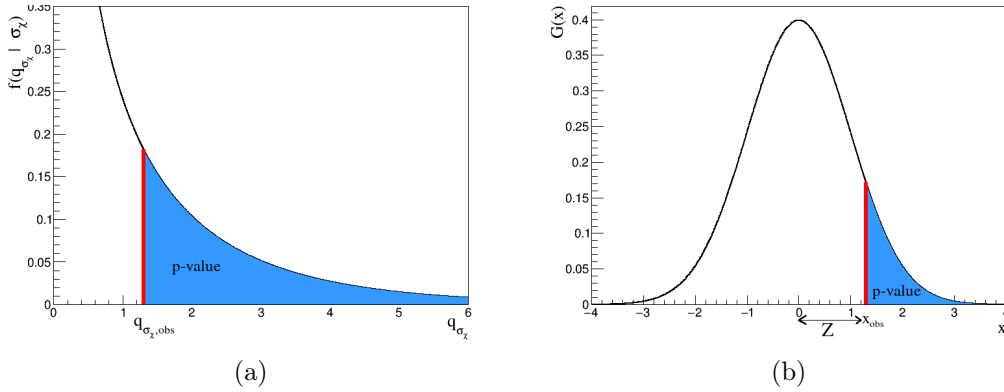


Figure 5.1: Illustration of the p-value obtained from an observed value of the test statistic  $q_{\sigma_\chi}$  5.1(a) and the relation between the p-value and the significance  $Z$  in the standard normal distribution.

Solving for  $\mathcal{L}(\sigma_\chi, \hat{\boldsymbol{\theta}} | m_\chi, \delta, \mathbf{x})$  it becomes:

$$\ln \left( \mathcal{L}(\sigma_\chi, \hat{\boldsymbol{\theta}} | m_\chi, \delta, \mathbf{x}) \right) = \ln \left( \mathcal{L}(\hat{\sigma}_\chi \hat{\boldsymbol{\theta}} | m_\chi, \delta, \mathbf{x}) \right) - \frac{Z^2}{2}. \quad (5.10)$$

Once the confidence level (CL) relative to the desired exclusion limit is decided, it can be converted into significance as  $p - value = 1 - CL$ . Then with equation 5.10 the value of the exclusion limit for  $\sigma_\chi$  corresponding to such confidence level can be obtained. A typical value for the confidence level is 90%, thus the p-value is equal to 0.1 and the significance is 1.282.

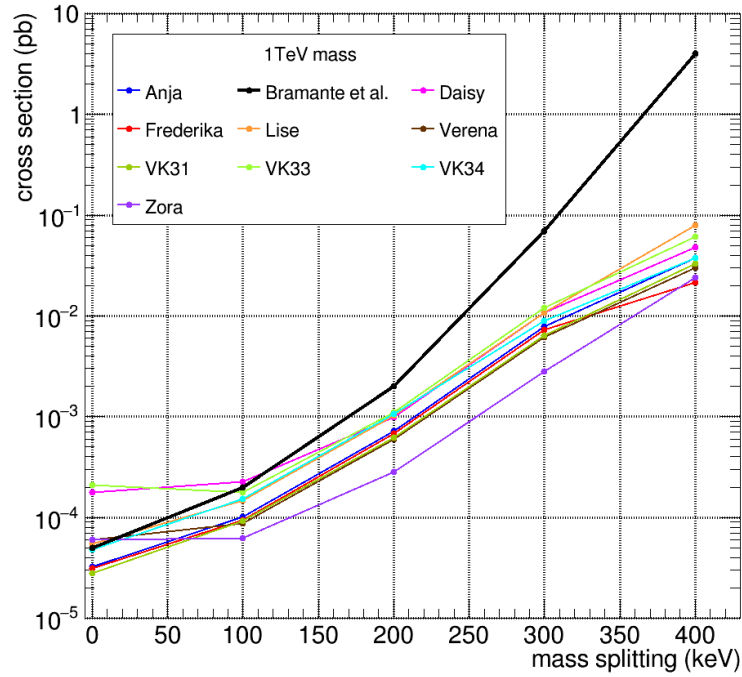
## 5.3 Results

The procedure described in the previous section for the exclusion limit calculation has been carried out for all the detectors of Run33. A subset of 9 detectors has been selected for the following analysis based on background, noise, and live-time of the detectors<sup>2</sup>. In appendix B detailed information for such detectors can be found: a table with detector design, energy resolution of the two channels and exposure, the energy spectrum, the band fit results in both Light-Energy plane and LY-Energy plane and the exclusion limits.

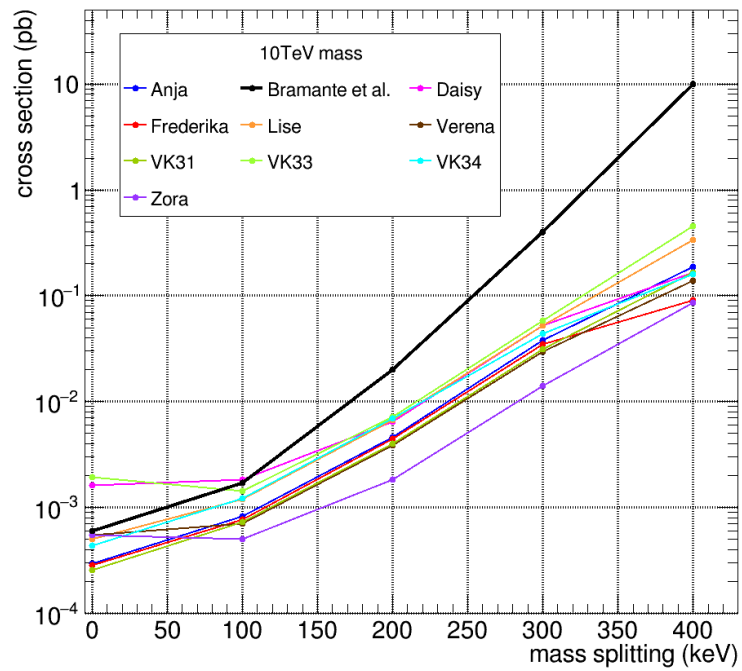
In figure 5.2 the iDM cross-section exclusion limit<sup>3</sup> as a function of the mass splitting  $\delta$  is shown for two dark matter masses:  $m_\chi = 1$  TeV and  $m_\chi = 10$  TeV in figure 5.2(a) and 5.2(b) respectively. The black line correspond to the limit obtained by Bramante et al. [1] with CRESST-II data [3] extending the energy window up to 500 keV in the hypothesis of zero background in the unpublished energy region and assuming integrated luminosities and event rates. First of all,

<sup>2</sup>Further 7 detectors are currently under study because of problems in the analysis procedure. They might be eventually included in this analysis after a dedicated re-analysis for which major modifications in the analysis software are needed.

<sup>3</sup>As discussed in subsection 1.3.1 only iDM interactions are considered for this analysis.



(a)



(b)

Figure 5.2: Cross-section exclusion limit for iDM of mass 1 TeV (figure 5.2(a)) and 10 TeV (figure 5.2(b)) for several CRESST-II modules.

it can be appreciated that for almost all the detector modules the limit resulting from this analysis is lower than the limit presented in Ref. [1] and this is mainly due to the larger exposure of the analysis presented in this work. To obtain the expected exclusion limit an exposure of 52 kg day has been used (see Ref. [1] and Ref. [3]). In particular for both the dark matter masses there is only one detector (Daisy) that presents a limit slightly higher than the one of Bramante et al. Thus, apart from Daisy, all the measured limits show an improvement with respect to the theoretical limit that increases with higher mass splittings reaching more than one order of magnitude for a mass splitting equal to 400 keV. At zero mass splitting, that is for elastic scattering, the measured limits do not show a general improvement with respect to the theoretical limit, but this analysis is optimized for high recoil energy from inelastic dark matter therefore this is not surprising.

The combined limit with three detectors is shown in figure 5.3 for both 1 TeV and 10 TeV dark matter mass together with the limits of the individual detectors. The detectors chosen for this first combined limit are Anja, Frederika and VK31 since they present a similar behaviour over all the mass splitting intervals. The combined limit thus obtained corresponds to a total exposure of almost 460 kg days.

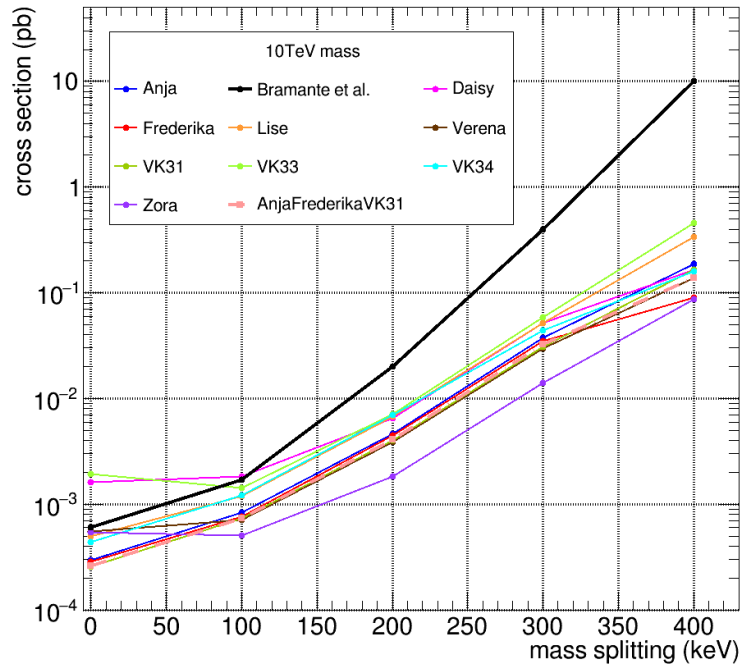
For both the dark matter masses considered, the exclusion limit obtained combining detectors Anja, Frederika and VK31 shows almost no improvement with respect to the limits of the corresponding individual detectors suggesting the presence of some background not considered in the likelihood.

In order to verify this hypothesis the exclusion limit has been calculated including also detector Zora, which exhibits the lower limit over almost all the mass splitting range considered. The resulting exclusion limit is shown in figure 5.4(a) and 5.4(b) for dark matter mass of 1 TeV and 10 TeV respectively. This exclusion limit, corresponding to a total exposure of more the 600 kg day, presents a small improvement with respect to the previous combined limit lying well above the exclusion limit obtained with detector Zora only.

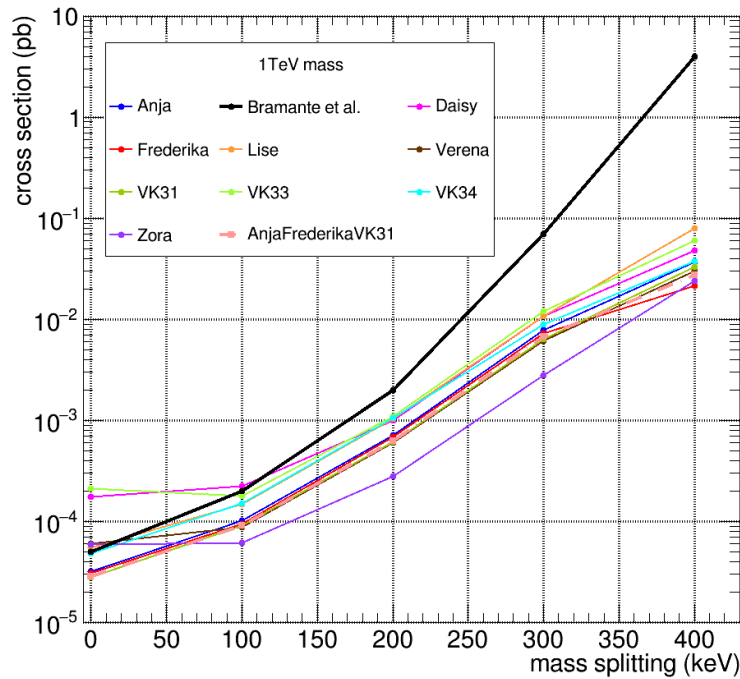
To understand what could be the source of the background not considered in the likelihood, the distribution of the events in the nuclear recoil bands was investigated for these four detectors. The LY-energy plots for detector Anja, Frederika, VK31 and Zora are shown in figure 5.5(a), 5.5(b), 5.5(c), 5.5(d) respectively. The population lying between the electron/ $\gamma$  band and the nuclear recoil bands at  $\sim 100$  keV is due to the decay of  $^{210}\text{Po}$  as already discussed in subsection 2.3.5. Polonium decay events are definitely evident for detectors Frederika and Zora but, thanks to the scintillating foil, they are located outside the nuclear recoil band as their LY is higher than 0.2. At roughly the same energy, however, all the detectors<sup>4</sup> present a clear population inside the tungsten recoil band. Considering the energy of this population, they might be events of polonium decay in which the  $\alpha$  particle is not detected by any active material

---

<sup>4</sup>Such population is present in all the analysed detector modules. Here the LY-energy plot is shown only for few detectors for brevity.

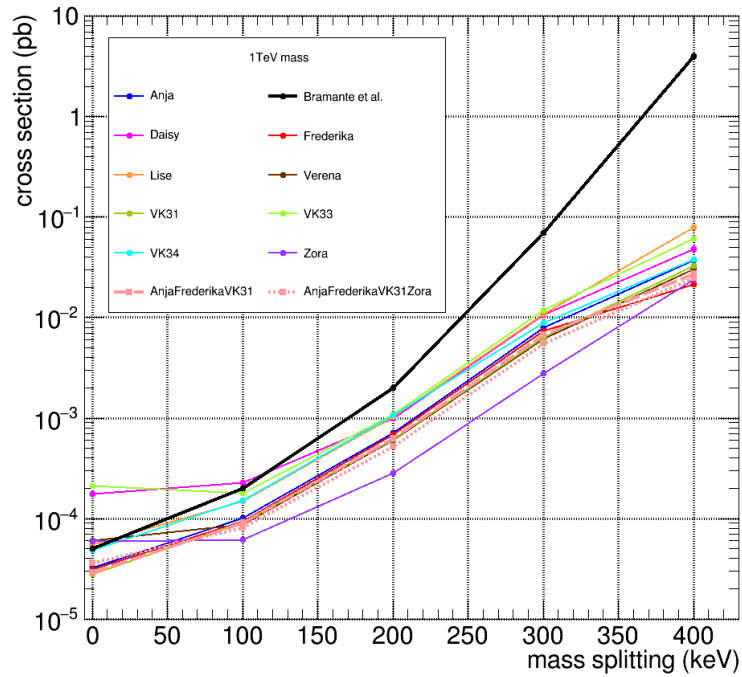


(a)

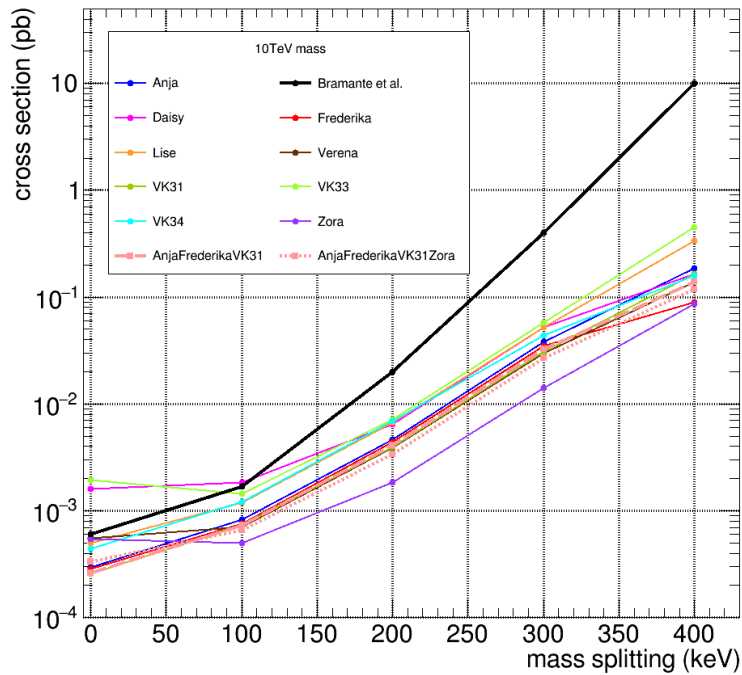


(b)

Figure 5.3: Cross-section exclusion limit for iDM of mass 1 TeV (figure 5.3(a)) and 10 TeV (figure 5.3(b)) derived from the combination of three modules (Anja, Frederika, VK31) in dashed line. The individual exclusion limits of the CRESST-II modules are also shown for comparison.

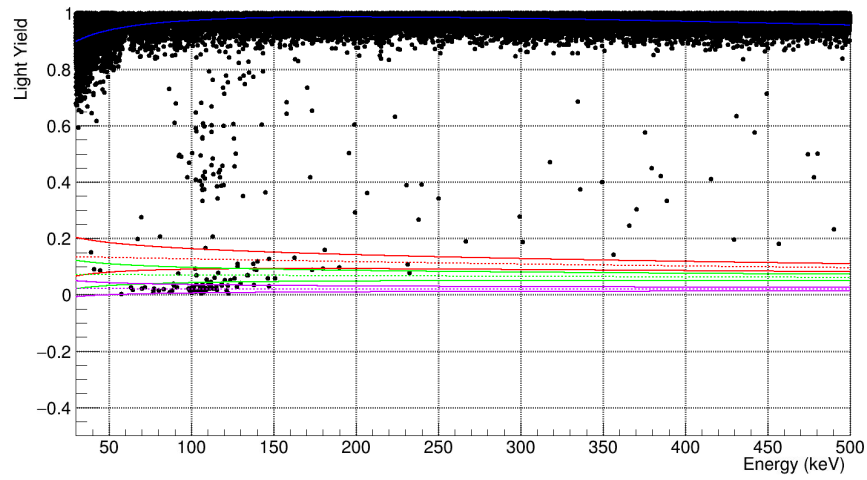


(a)

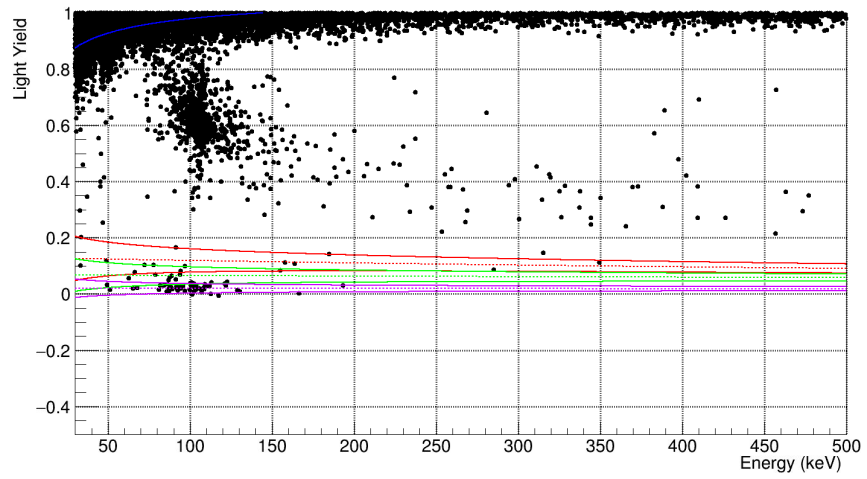


(b)

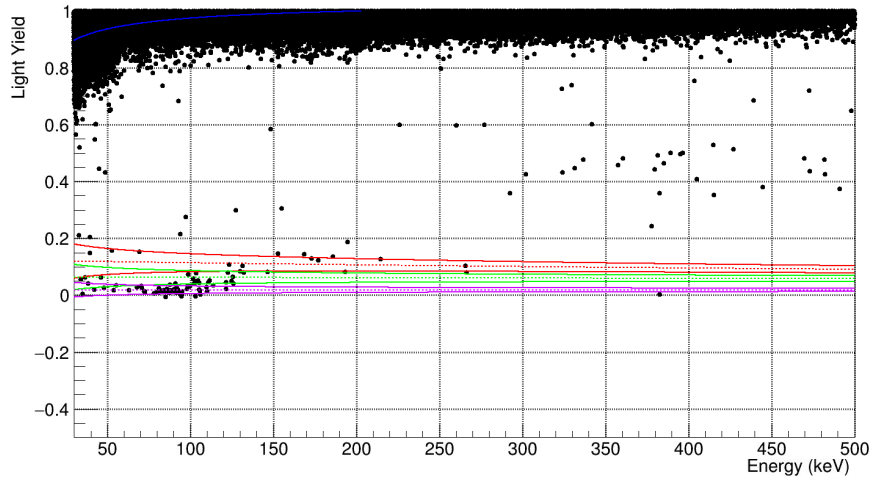
Figure 5.4: Cross-section exclusion limit for iDM of mass 1 TeV (figure 5.4(a)) and 10 TeV (figure 5.4(b)) derived from the combination of four modules (Anja, Frederika, VK31, Zora) compared with the combined exclusion limit shown in figure 5.3. The individual exclusion limits of the CRESST-II modules are also shown for comparison.



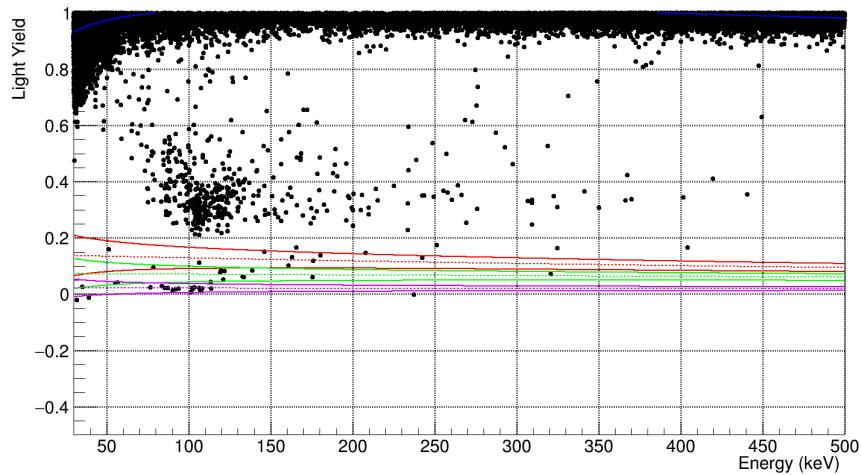
(a) Detector Anja



(b) Detector Frederika



(c) Detector VK31



(d) Detector Zora

Figure 5.5: LY-energy plot for Anja, Frederika, VK31 and Zora modules respectively in figure 5.5(a), 5.5(b), 5.5(c), 5.5(d). The events due to  $^{210}\text{Po}$  decay are clear especially in modules Frederika and Zora. A small population at  $\sim 100$  keV is also present in the tungsten recoil band of all the detectors. They are probably events of  $^{210}\text{Po}$  decay in which the  $\alpha$  particle is not detected by any active material.

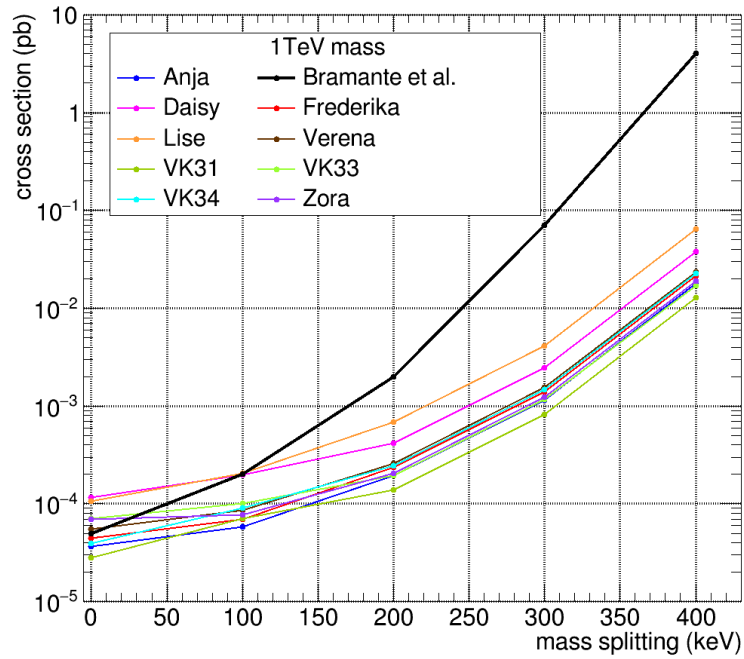
while the polonium recoil is detected as heat signal. Considering the design of the detector modules, the  $\alpha$  particle produced in such decays, if not detected, is absorbed by the clamps holding the crystal. Moreover, they are populating almost exclusively the tungsten recoil band and this is due to the similar mass number.

To verify whether this population is the background determining the small improvements of the combined limits, new exclusion limits have been calculated for all the detectors using a different energy region. In figure 5.6 the exclusion limits obtained for each single detector considering recoil energy in the interval [150 – 500] keV are shown together with the exclusion limit from [1]. The overall effect consists in the improvement of the exclusion limit for all the mass splittings and all the detectors: with  $m_\chi = 1$  TeV there is again one detector that has a limit higher than the theoretical one for mass splitting equal to 100 keV but with  $m_\chi = 10$  TeV the measured exclusion limit is lower than the theoretical one for all the detectors and for all the mass splitting considered.

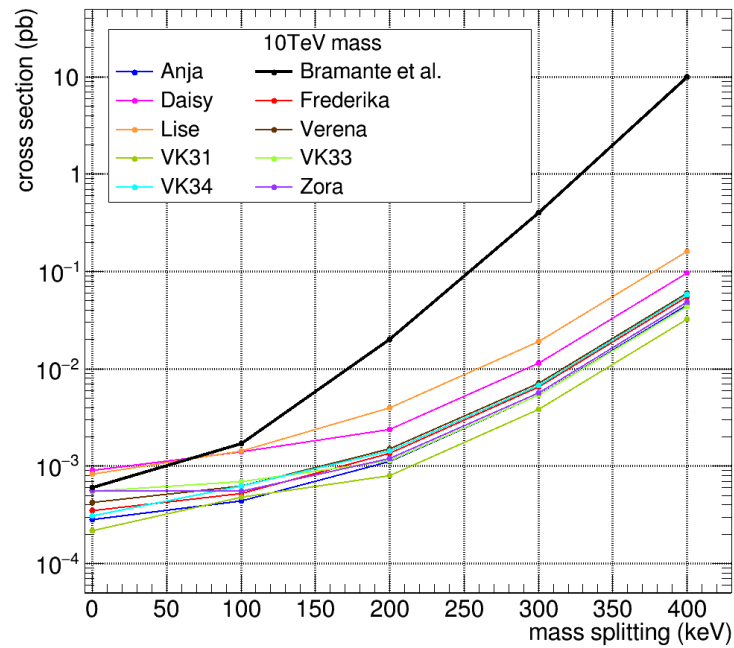
With these new values, the effect of combining multiple detectors has been investigated again. In figure 5.7 the combined detector exclusion limits obtained with Anja, Frederika, VK31, Zora, and then adding also detector VK33, are shown. Although the population at  $\sim 100$  keV has been removed, the combination of multiple detector modules is not improving the exclusion limit. Raising the lower limit has been the first attempt to investigate the effect of the population at  $\sim 100$  keV as high recoil energies are fundamental to probe the iDM cross-section. A dedicated study of the background contribution as well as the implementation of the density function for the polonium decay have to be done.

Despite all the problems encountered with the combination of results obtained with different detector modules, it would be interesting to compare the results of this work with the results of other experiments. However, lots of models have been developed in the last few decades involving inelastic dark matter particles with several possible interactions and candidates [57, 60]. Moreover, there is no standard scenario, nor common set of assumptions in these models regarding for example the velocity distribution and the energy density of dark matter, both elements that have relations to particle astrophysics and cosmology. Therefore one has to be extremely careful in comparing results of different experiments as they can be obtained with a dark matter model different with respect to the one adopted for the current analysis. The risk in fact is to compare cross-sections that cannot be directly related to each other because they are derived from completely different assumptions.

Therefore in figure 5.8 the results of this work has been compared with the expected exclusion limits presented in Ref. [1]. The results of this work correspond to the star-filled area: it includes all the exclusion limits presented in the previous plots of this chapter as for each mass splitting the maximum and the minimum cross-section have been used to build such area. The solid lines correspond to the expected exclusion limits for tungsten (red), xenon (blue) and iodine (green). Such exclusion limits are obtained with LUX, PandaX II,

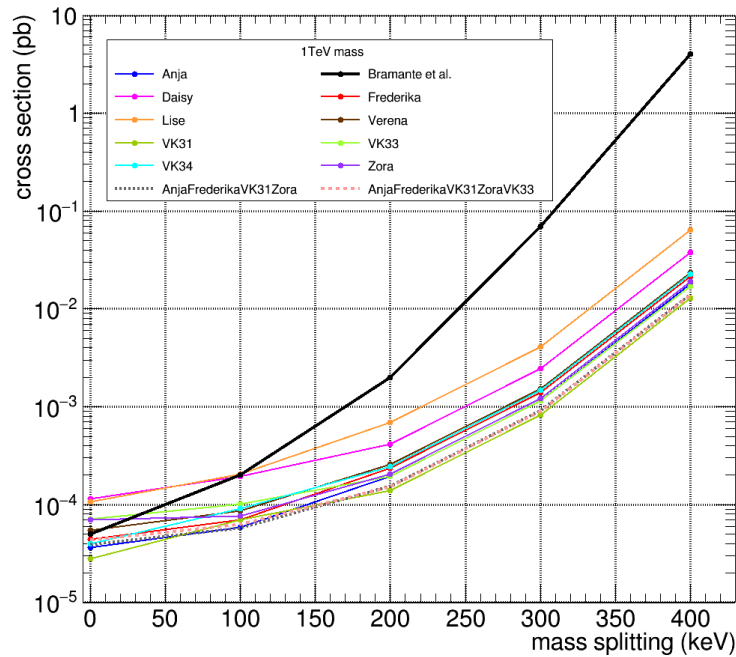


(a)

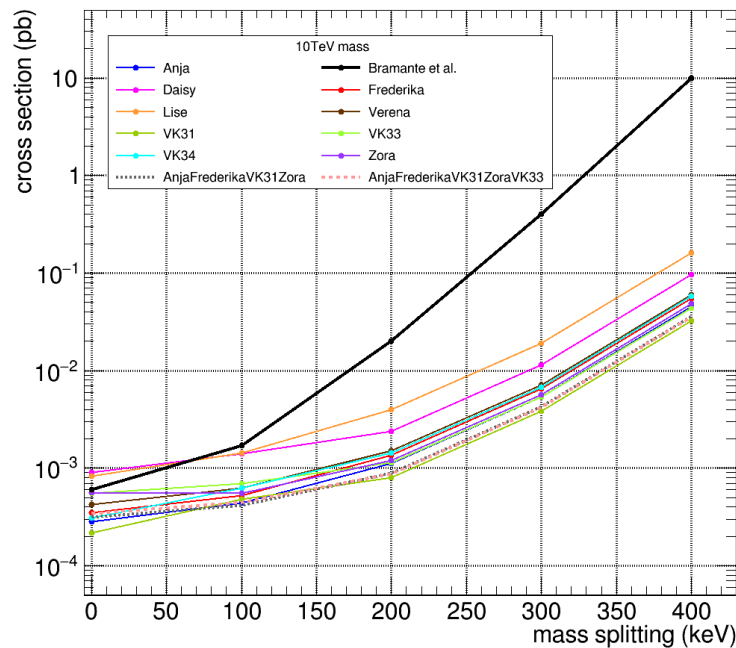


(b)

Figure 5.6: Cross-section exclusion limit for iDM of mass 1 TeV (figure 5.6(a)) and 10 TeV (figure 5.6(b)) for several CRESST-II modules obtained with recoil energy in the range  $[150 - 500]$  keV.

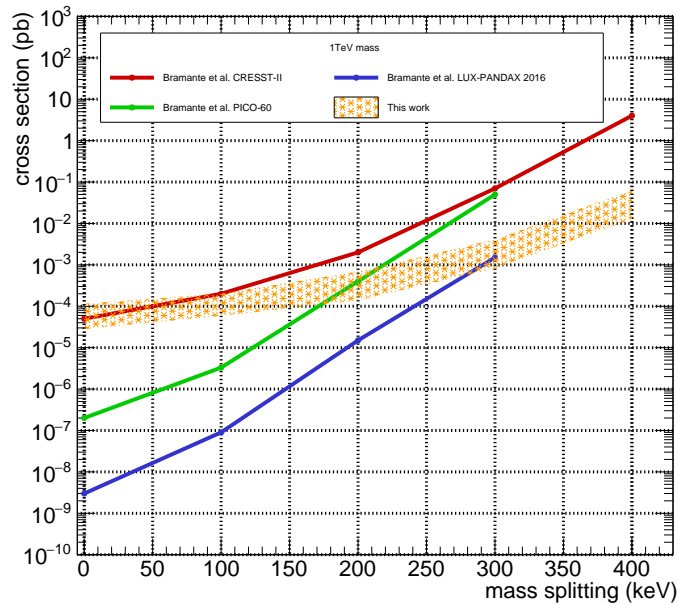


(a)

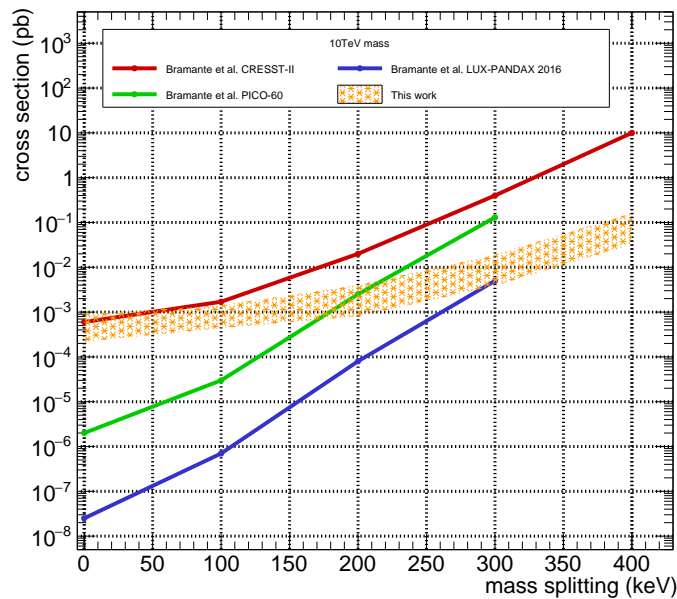


(b)

Figure 5.7: Cross-section exclusion limit for iDM of mass 1 TeV (figure 5.4(a)) and 10 TeV (figure 5.4(b)) derived from the combination of three and four modules (see legend) and considering recoil energy in the interval  $[150 - 500]$  keV. The individual exclusion limits of the CRESST-II modules obtained with the same recoil energies are also shown for comparison.



(a)



(b)

Figure 5.8: Cross-section exclusion limit for iDM of mass 1 TeV (figure 5.8(a)) and 10 TeV (figure 5.8(b)) resulting from this work (star-filled area) are compared with the expected exclusion limits obtained considering several target nuclei: tungsten (red line), xenon (blue line) and iodine (green line). These expected exclusion limits are obtained in Ref. [1] with LUX, PandaX II, PICO-60, and CRESST II data assuming integrated luminosities, event rates and nuclear masses and supposing zero background events in the high energy bins for LUX-PandaX and CRESST as no high-recoil data are publicly available.

---

PICO-60, and CRESST II data assuming integrated luminosities, event rates and nuclear masses. For LUX-PandaX and CRESST no high-recoil data are publicly available therefore the hypothesis of zero background events in the high energy bins has been adopted. Thanks to the larger exposure the exclusion limit of the analysis presented in this work is better than the one obtained with PICO-60 for mass splitting  $\gtrsim 200$  keV.

## Conclusions and outlook

In this work CRESST data have been analysed in the framework of the inelastic dark matter. The combination of the results from multiple detectors have been performed to exploit the total exposure of  $\sim 600$  keV day. The final limits for a dark matter mass of 1 TeV and 10 TeV and with a mass splitting going from 0 to 400 keV have been presented in section 5.3. The resulting limit is the best limit ever obtained within this framework with Tungsten as target material. For mass splitting  $>100$  keV the result of this work exceeds the limit evaluated by Bramante et al. [1] for Tungsten with CRESST data as well as the expected limit for Iodine obtained with PICO-60 data [1]. Moreover it reaches an improvement of almost 2 orders of magnitude with respect to the predicted one at mass splitting equal to 400 keV.

This work lays the foundations for future works on inelastic dark matter in CRESST. Future development aiming to improve the sensitivity for this type of events should embrace first of all an increase of the exposure including more detectors in the analysis. Secondly an improvement of the band fit software performances is necessary, especially for what concerns the description of the energy spectra.

As discussed in section 4.6, the presence of inelastic scattering of neutrons off Tungsten, whose spectrum is not included in the density functions of the band fit software, made it impossible to benefit of the higher statistics given by the [neutron calibration+background] data in the band fit procedure. Similarly, as discussed in section 5.3, due to the irreducible background of Polonium recoils not yet included in the density functions of the exclusion limit software, the energy range for the limit extrapolation had to be reduced. Moreover the  $\gamma$  lines tilt should be corrected with an energy dependent  $\eta$  factor to definitively remove the residual tilt present at high energy. Finally the energy spectra and density functions parametrization as well as the  $\eta$  factor have introduced some systematic uncertainties that must be considered and included for a complete analysis. In addition to the systematics, for an extensive and accurate analysis, the validity of the assumption that the test statistics discussed in 5.2 is  $\chi^2$  distributed must be verified with the given data and energy region.



# Appendices



A

## Inelastic dark matter rate derivation

As discussed in subsection 1.3.3 the DM scattering rate for a given recoil energy  $E_R$  and a detector mass  $M$  can be written as:

$$\frac{dR}{dE_R dM} = n_X N_T \int_{v_{min}}^{v_{max}} v f(\vec{v}, \vec{v}_e) \frac{d\sigma}{dE_R} d^3v \quad (\text{A.1})$$

where  $n_X = \rho_X/m_X$  is the local DM number density,  $N_T$  is the number of scattering targets per unit mass,  $v_{min}$  and  $v_{max}$  are respectively the minimum dark matter speed in the detector's rest frame and the maximum incoming DM speed in the Earth rest frame of reference,  $f(\vec{v}, \vec{v}_e)$  is the velocity distribution which depends on  $\vec{v}$  and  $\vec{v}_e$  being the DM and Earth velocity in the Galactic rest frame respectively and finally  $d\sigma/dE_R$  is the differential cross-section for dark matter scattering off a nucleus.

The considered velocity distribution is a Maxwellian with a sharp cutoff at the escape velocity and its expression is given by the equation:

$$f(\vec{v}, \vec{v}_e) = \frac{e^{-(v^2+v_e^2+2v v_e \cos \theta)/v_0^2}}{N(v_0, v_{esc})} \quad (\text{A.2})$$

where  $\theta$  is the angle between  $\vec{v}$  and  $\vec{v}_e$  and  $N(v_0, v_{esc})$  is the normalization factor given by equation 1.11.

In the hypothesis of equal coupling of DM with protons and neutrons the differential cross-section has the following expression:

$$\frac{d\sigma}{dE_R} = \frac{\sigma_n m_N}{v^2 2\mu_n^2} A^2 F_h^2(E_R). \quad (\text{A.3})$$

where  $\sigma_n$  and  $\mu_n$  are the dark matter-nucleon scattering cross-section and reduced mass,  $v$  is the DM velocity,  $m_N$  is the nucleus mass,  $A$  is the nuclear atomic mass and  $F_h$  corresponds to the Helm form factor (see equation 1.16).

Substituting the expressions for the velocity distribution and the differential cross-section, the formula for the DM scattering rate becomes:

$$\begin{aligned}
\frac{dR}{dE_R} &= n_X N_T \int_{v_{min}}^{v_{max}} v f(\vec{v}, \vec{v}_e) \frac{d\sigma}{dE_R} d^3v = \\
&= n_X N_T \int_{v_{min}}^{v_{max}} v \frac{e^{-(v^2+v_e^2+2vv_e\cos\theta)/v_0^2}}{N(v_0, v_{esc})} \frac{\sigma_n m_N}{v^2 2\mu_n^2} A^2 F^2(E_R) d^3v \quad (\text{A.4}) \\
&= \frac{n_X N_T}{N(v_0, v_{esc})} \frac{m_N}{2\mu_n^2} A^2 F^2(E_R) \sigma_n \int_{v_{min}}^{v_{max}} v e^{-(v^2+v_e^2+2vv_e\cos\theta)/v_0^2} \frac{1}{v^2} d^3v
\end{aligned}$$

The maximum DM velocity in the galactic rest frame correspond to the escape velocity of the galaxy itself while the maximum DM velocity in the Earth's rest frame is given by  $\vec{v}_{max} = \vec{v}_{esc} - \vec{v}_e$ . For finite  $v_{esc}$  the velocity integral depends on the relative order between  $v_{min}$  and  $v_{esc} - v_e$ :

$$\begin{aligned}
\int_{v_{min}}^{v_{max}} d^3v &= \int_{v_{min}}^{v_{max}} \int_{-1}^1 \int_0^{2\pi} v^2 dv d\cos\theta d\phi = \\
&= 2\pi \begin{cases} \int_{v_{min}}^{v_{esc}-v_e} v^2 dv \int_{-1}^1 d\cos\theta + \int_{v_{esc}-v_e}^{v_{esc}+v_e} v^2 dv \int_{-1}^{c^*} d\cos\theta & v_{min} < v_{esc} - v_e \\ \int_{v_{min}}^{v_{esc}+v_e} v^2 dv \int_{-1}^{c^*} d\cos\theta & v_{esc} - v_e < v_{min} < v_{esc} + v_e \end{cases} \quad (\text{A.5})
\end{aligned}$$

where  $c^* = \cos\theta^* = (v_{esc}^2 - v^2 - v_e^2)/(2vv_e)$  is the minimum angle possible for the scattering when  $v_{esc} - v_e < v_{min} < v_{esc} + v_e$ .

As first step, the two integrals over  $\cos(\theta)$  are evaluated:

$$\int_{-1}^1 e^{-(v^2+v_e^2+2vv_e\cos\theta)/v_0^2} d\cos\theta = -\frac{v_0^2}{2vv_e} \left[ e^{-\left(\frac{v+v_e}{v_0}\right)^2} - e^{-\left(\frac{v-v_e}{v_0}\right)^2} \right] \quad (\text{A.6})$$

$$\int_{-1}^{c^*} e^{-(v^2+v_e^2+2vv_e\cos\theta)/v_0^2} d\cos\theta = -\frac{v_0^2}{2vv_e} \left[ e^{-\left(\frac{v_{esc}}{v_0}\right)^2} - e^{-\left(\frac{v-v_e}{v_0}\right)^2} \right] \quad (\text{A.7})$$

After integrating over the angular part the 3D velocity integral become:

$$\int_{v_{min}}^{v_{max}} v e^{-(v^2+v_e^2+2vv_e \cos\theta)/v_0^2} \frac{1}{v^2} d^3v = 2\pi \left( -\frac{v_0^2}{2v_e} \right).$$

$$\left\{ \begin{array}{l} \int_{v_{min}}^{v_{esc}-v_e} \left[ e^{-\left(\frac{v+v_e}{v_0}\right)^2} - e^{-\left(\frac{v-v_e}{v_0}\right)^2} \right] dv + \int_{v_{esc}-v_e}^{v_{esc}+v_e} \left[ e^{-\left(\frac{v_{esc}}{v_0}\right)^2} - e^{-\left(\frac{v-v_e}{v_0}\right)^2} \right] dv \quad v_{min} < v_{esc} - v_e \\ \int_{v_{min}}^{v_{esc}+v_e} \left[ e^{-\left(\frac{v_{esc}}{v_0}\right)^2} - e^{-\left(\frac{v-v_e}{v_0}\right)^2} \right] dv \quad v_{esc} - v_e < v_{min} < v_{esc} + v_e \end{array} \right. \quad (A.8)$$

Therefore if  $v_{min} < v_{esc} - v_e$  the final result is:

$$\frac{dR}{dE_R} = \frac{n_X N_T}{N(v_0, v_{esc})} \frac{m_N}{2\mu_n^2} A^2 F^2 (E_R) \sigma_n 2\pi \left( -\frac{v_0^2}{2v_e} \right) \left\{ \int_{v_{min}}^{v_{esc}-v_e} e^{-\left(\frac{v+v_e}{v_0}\right)^2} dv + \right.$$

$$\left. + \int_{v_{min}}^{v_{esc}+v_e} e^{-\left(\frac{v-v_e}{v_0}\right)^2} dv + e^{-\left(\frac{v_{esc}}{v_0}\right)^2} (2v_e) \right\} \quad (A.9)$$

while in case of  $v_{esc} - v_e < v_{min} < v_{esc} + v_e$  the final result is:

$$\frac{dR}{dE_R} = \frac{n_X N_T}{N(v_0, v_{esc})} \frac{m_N}{2\mu_n^2} A^2 F^2 (E_R) \sigma_n 2\pi \left( -\frac{v_0^2}{2v_e} \right) \left\{ e^{-\left(\frac{v_{esc}}{v_0}\right)^2} (v_{esc} + v_e - v_{min}) + \right.$$

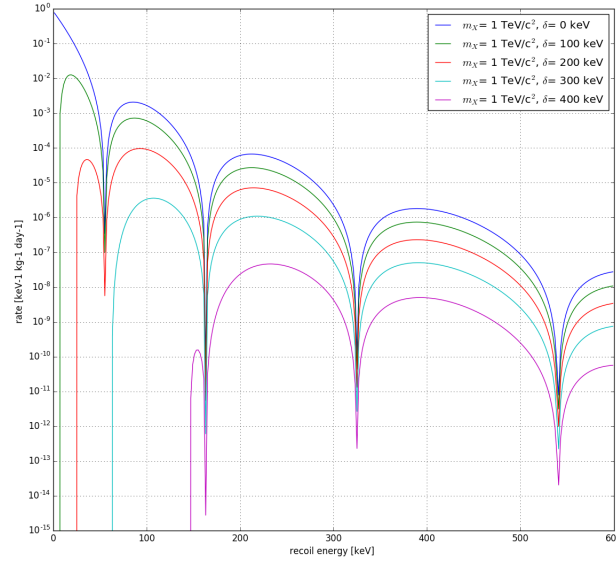
$$\left. + \int_{v_{min}}^{v_{esc}+v_e} e^{-\left(\frac{v-v_e}{v_0}\right)^2} dv \right\} \quad (A.10)$$

where:

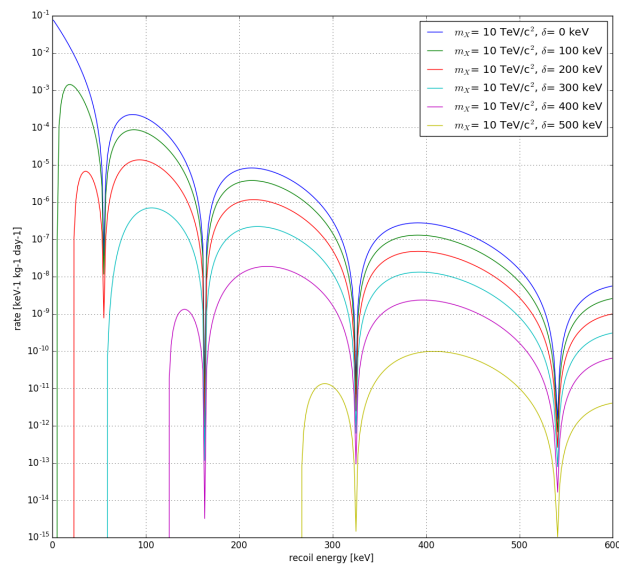
$$\int_{v_{min}}^{v_{esc}-v_e} e^{-\left(\frac{v+v_e}{v_0}\right)^2} dv = +\frac{1}{2}\sqrt{\pi} v_0 \left[ \operatorname{erf} \left( \frac{v_{esc}}{v_0} \right) - \operatorname{erf} \left( \frac{v_e + v_{min}}{v_0} \right) \right] \quad (A.11)$$

$$\int_{v_{min}}^{v_{esc}+v_e} e^{-\left(\frac{v-v_e}{v_0}\right)^2} dv = -\frac{1}{2}\sqrt{\pi} v_0 \left[ \operatorname{erf} \left( -\frac{v_{esc}}{v_0} \right) - \operatorname{erf} \left( \frac{v_e - v_{min}}{v_0} \right) \right] \quad (A.12)$$

To obtain the expected spectra presented in Ref. [1] the following values for the velocities  $v_{esc} = 533$  km/s,  $v_0 = 220$  km/s and  $v_e = 232$  km/s have to be considered. Assuming a DM density of  $0.3$  GeV/cm<sup>3</sup> and considering Tungsten as target material the spectra shown in figure A.1(a) and A.1(b) are obtained respectively for dark matter mass equal to  $m_\chi = 1$  TeV and  $m_\chi = 10$  TeV and using several values of mass splittings as indicated in the legend. Finally these spectra can be compared with the ones in figure 1.5.



(a)



(b)

Figure A.1: Expected spectra resulting from this calculation. Dark matter mass and splitting are indicated in the legend.



## Detector modules details

In this appendix detailed information for the 9 detectors selected for the analysis of chapter 5 are presented. For each detector the following information are illustrated:

1. a table containing the main characteristics of the detector (design, energy resolution for the phonon and light channel and exposure);
2. the energy spectrum after all the selections and the corrections described in chapter 3;
3. the L:E and LY:E plots with the band fit results obtained including neutron calibration data;
4. the L:E and LY:E plots with the band fit results obtained with only the background data;
5. the exclusion limit evaluated using the energy range [30, 500] keV for dark matter masses of 1 TeV and 10 TeV;
6. the elision limit evaluated using the energy range [150, 500] keV for dark matter masses of 1 TeV and 10 TeV.

All the exclusion limits are compared with the exclusion limits expected for 3 different target materials: Tungsten (red line, from CRESST-II data), Xenon (blue line, from LUX and PANDAX 2016 data), and Iodine (green line, from PICO-60 data). For further details regarding the expected limits, see Ref. [1].

## B.1 Detector Anja

Design	standard
$\sigma_P$	0.126 keV
$\sigma_L$	0.190 keV
Exposure	159.131 kg day

Table B.1: Detector information.

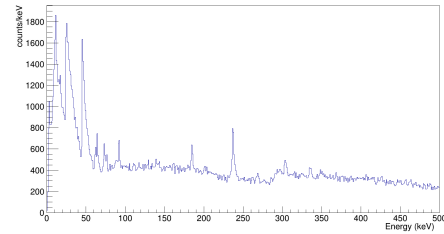


Figure B.1: Energy spectrum.

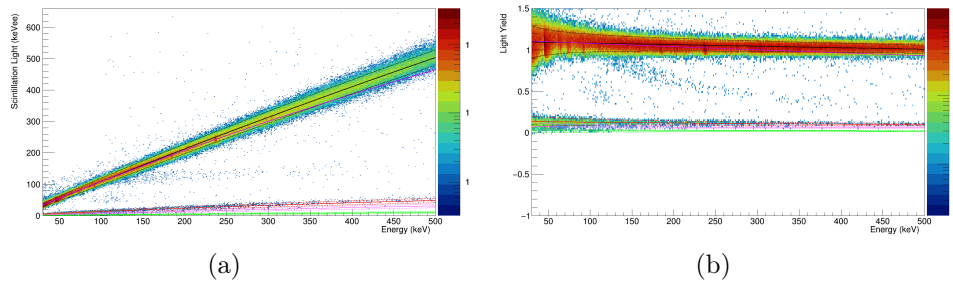


Figure B.2: Band fit result with neutron calibration dataset in the Light-Energy plane (figure B.2(a)) and in the LY-Energy plane (figure B.2(b)).

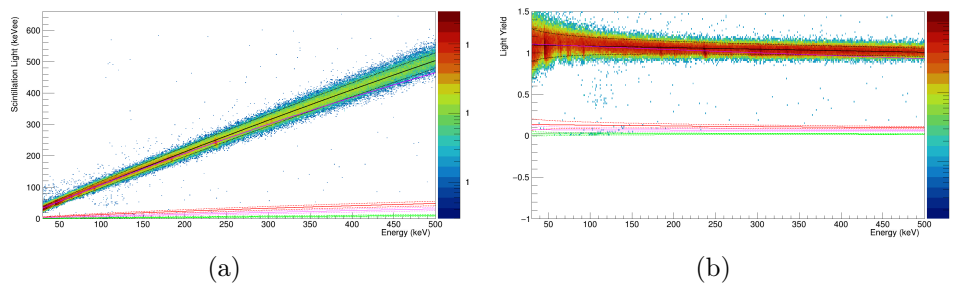


Figure B.3: Band fit result with background dataset in the Light-Energy plane (figure B.3(a)) and in the LY-Energy plane (figure B.3(b)).

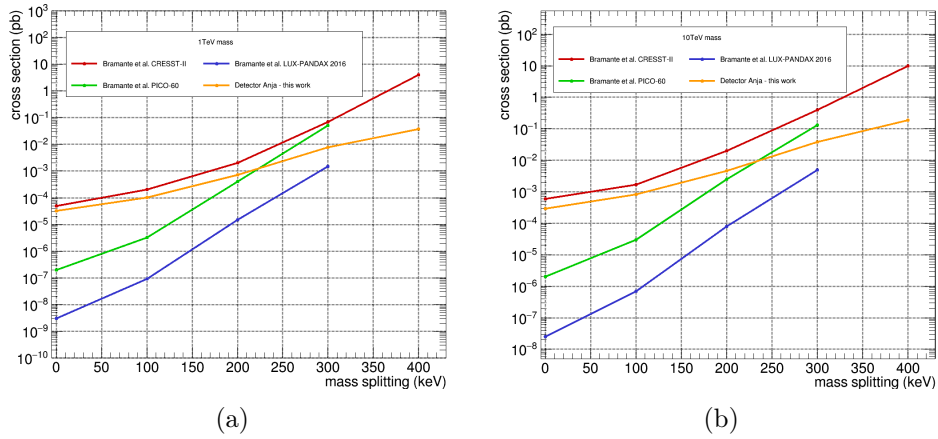


Figure B.4: Exclusion limit obtained using the energy region  $[30, 500]$  keV for a dark matter mass of 1 TeV (figure B.4(a)) and 10 TeV (figure B.4(b)).

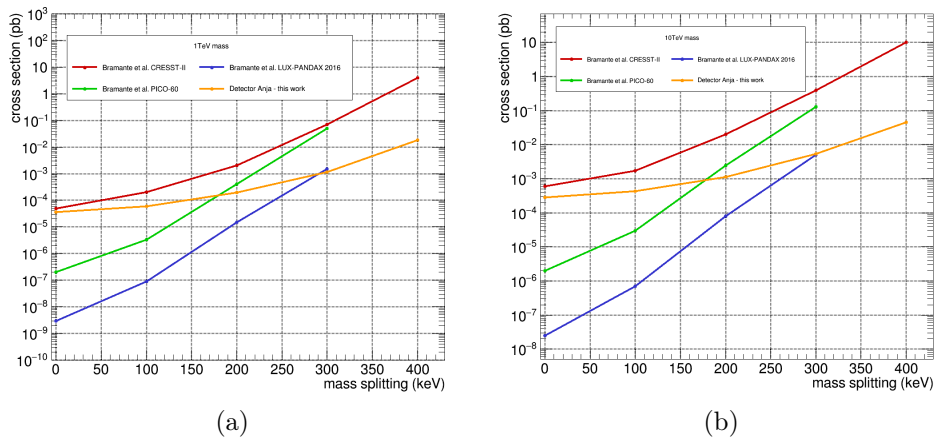


Figure B.5: Exclusion limit obtained using the energy region  $[150, 500]$  keV for a dark matter mass of 1 TeV (figure B.5(a)) and 10 TeV (figure B.5(b)).

## B.2 Detector Daisy

Design	standard
$\sigma_P$	0.0703 keV
$\sigma_L$	0.345 keV
Exposure	158.718 kg day

Table B.2: Detector information.

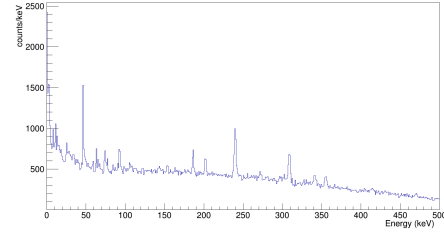
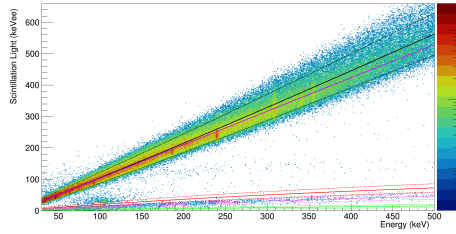
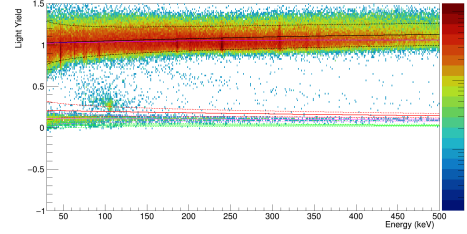


Figure B.6: Energy spectrum.

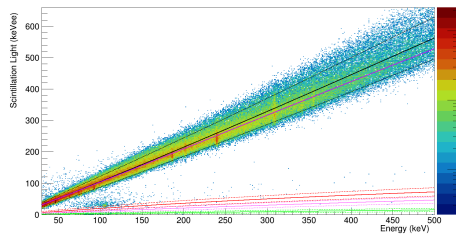


(a)

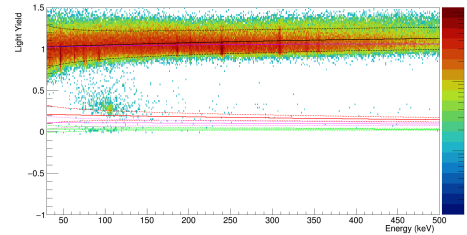


(b)

Figure B.7: Band fit result with neutron calibration dataset in the Light-Energy plane (figure B.7(a)) and in the LY-Energy plane (figure B.7(b)).



(a)



(b)

Figure B.8: Band fit result with background dataset in the Light-Energy plane (figure B.8(a)) and in the LY-Energy plane (figure B.8(b)).

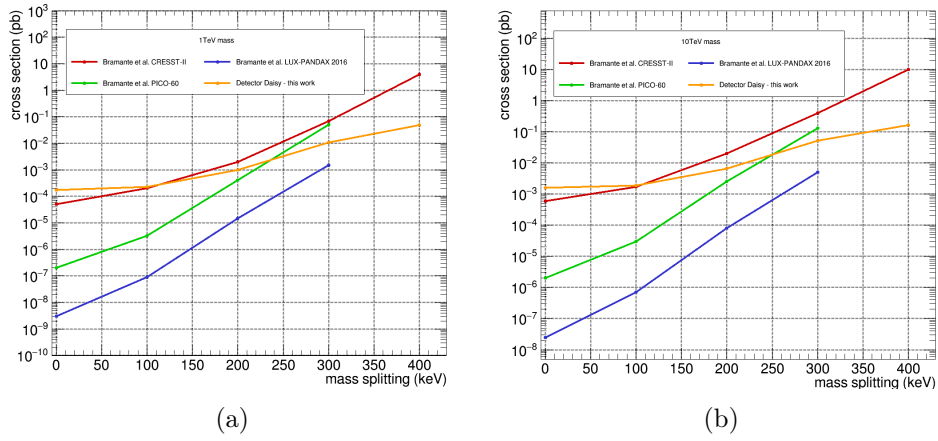


Figure B.9: Exclusion limit obtained using the energy region  $[30, 500]$  keV for a dark matter mass of 1 TeV (figure B.9(a)) and 10 TeV (figure B.9(b)).

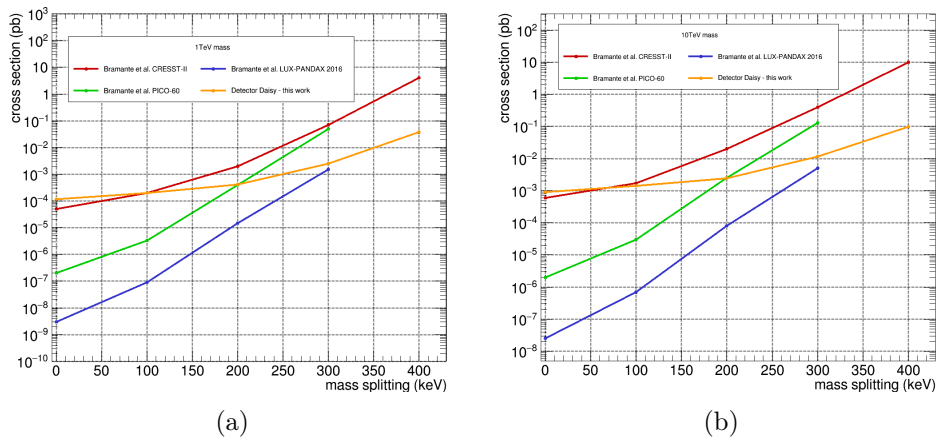


Figure B.10: Exclusion limit obtained using the energy region  $[150, 500]$  keV for a dark matter mass of 1 TeV (figure B.10(a)) and 10 TeV (figure B.10(b)).

### B.3 Detector Lise

Design	standard
$\sigma_P$	0.0598 keV
$\sigma_L$	3.23 keV
Exposure	158.672 kg day

Table B.3: Detector information.

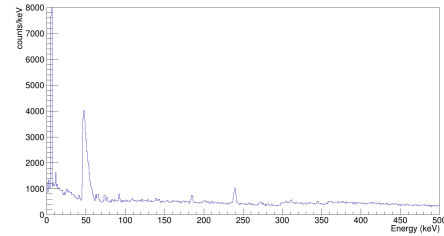


Figure B.11: Energy spectrum.

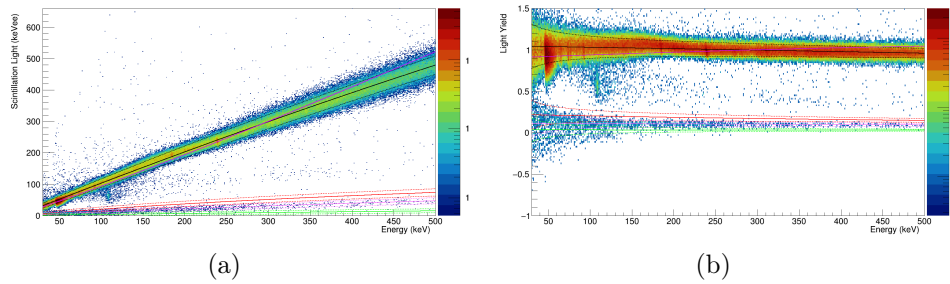


Figure B.12: Band fit result with neutron calibration dataset in the Light-Energy plane (figure B.12(a)) and in the LY-Energy plane (figure B.12(b)).

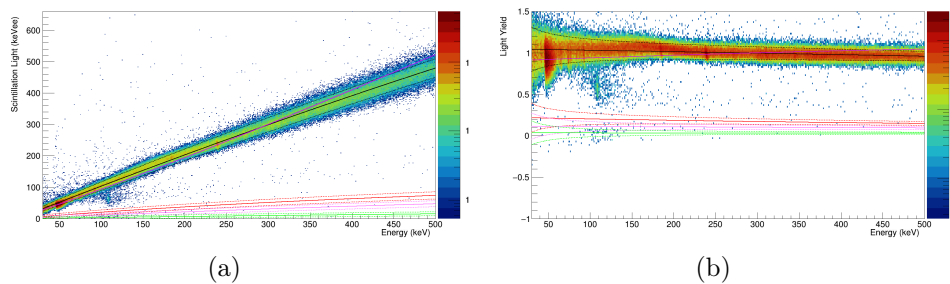


Figure B.13: Band fit result with background dataset in the Light-Energy plane (figure B.13(a)) and in the LY-Energy plane (figure B.13(b)).

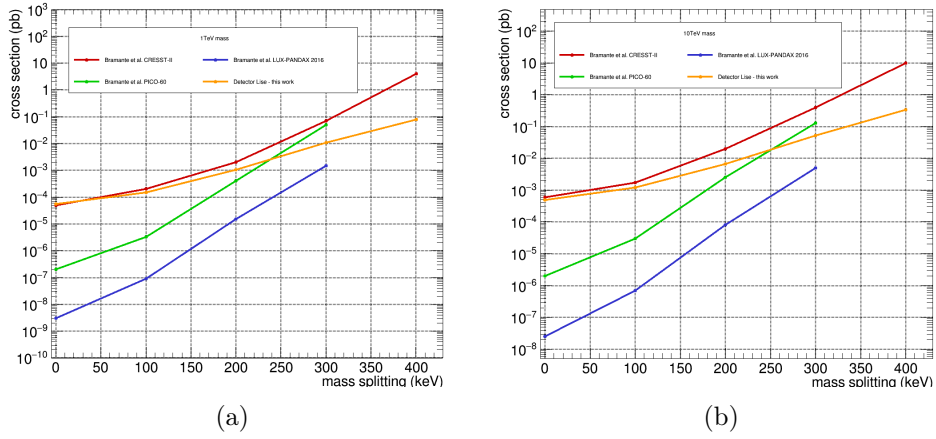


Figure B.14: Exclusion limit obtained using the energy region  $[30, 500]$  keV for a dark matter mass of 1 TeV (figure B.14(a)) and 10 TeV (figure B.14(b)).

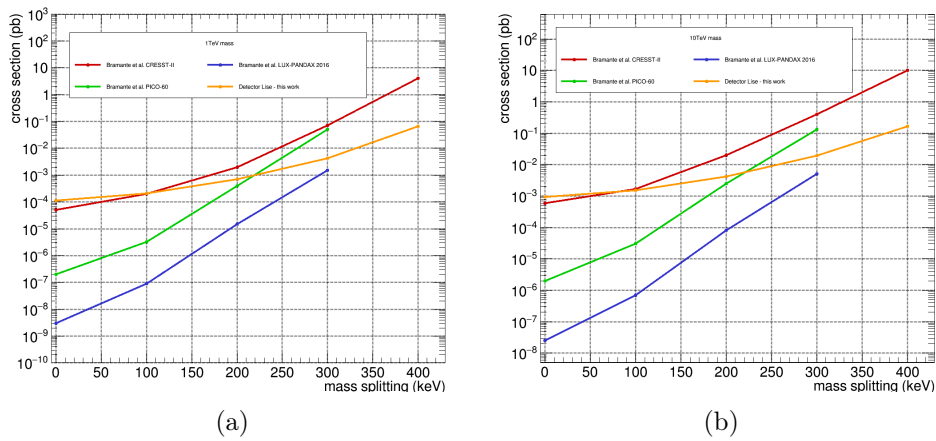


Figure B.15: Exclusion limit obtained using the energy region  $[150, 500]$  keV for a dark matter mass of 1 TeV (figure B.15(a)) and 10 TeV (figure B.15(b)).

## B.4 Detector VK31

Design	standard
$\sigma_P$	0.164 keV
$\sigma_L$	0.427 keV
Exposure	160.854 kg day

Table B.4: Detector information.

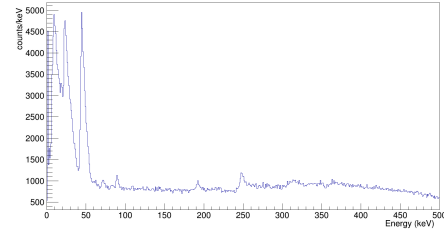
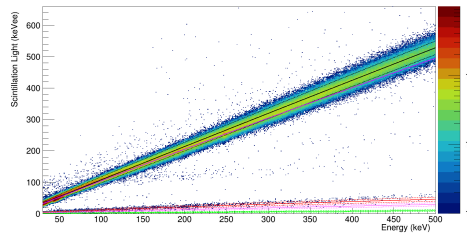
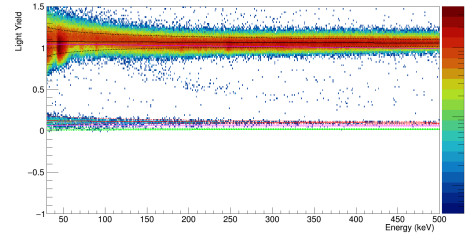


Figure B.16: Energy spectrum.

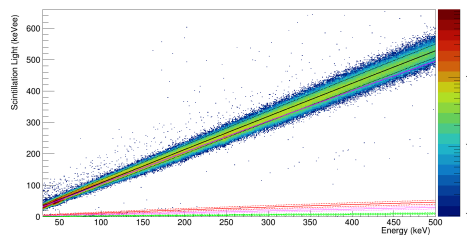


(a)

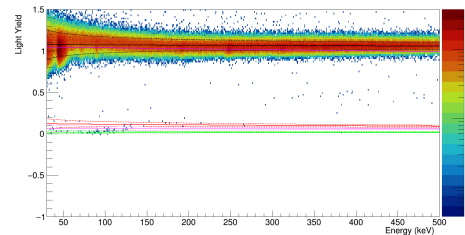


(b)

Figure B.17: Band fit result with neutron calibration dataset in the Light-Energy plane (figure B.17(a)) and in the LY-Energy plane (figure B.17(b)).



(a)



(b)

Figure B.18: Band fit result with background dataset in the Light-Energy plane (figure B.18(a)) and in the LY-Energy plane (figure B.18(b)).

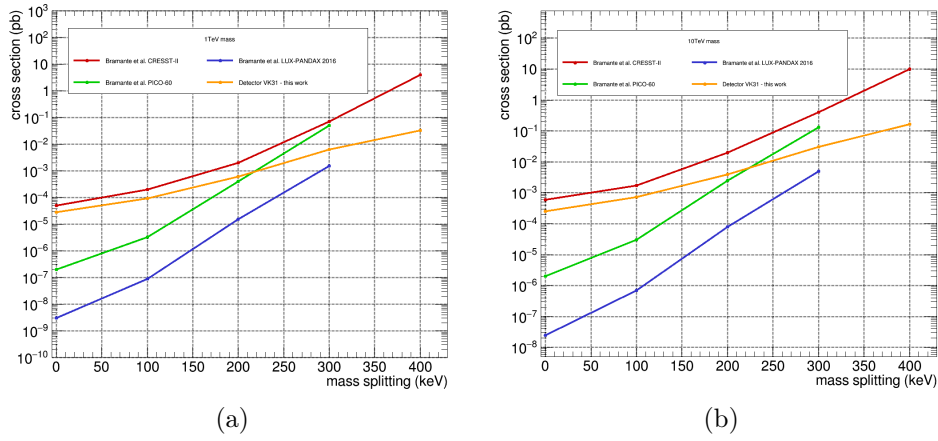


Figure B.19: Exclusion limit obtained using the energy region  $[30, 500]$  keV for a dark matter mass of 1 TeV (figure B.19(a)) and 10 TeV (figure B.19(b)).

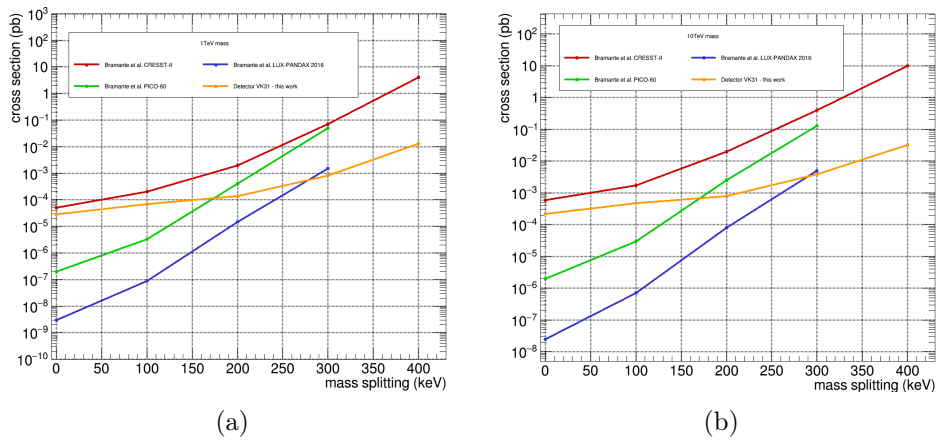


Figure B.20: Exclusion limit obtained using the energy region  $[150, 500]$  keV for a dark matter mass of 1 TeV (figure B.20(a)) and 10 TeV (figure B.20(b)).

## B.5 Detector VK34

Design	standard
$\sigma_P$	0.0981 keV
$\sigma_L$	0.164 keV
Exposure	162.949 kg day

Table B.5: Detector information.

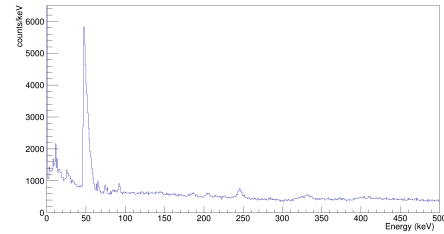


Figure B.21: Energy spectrum.

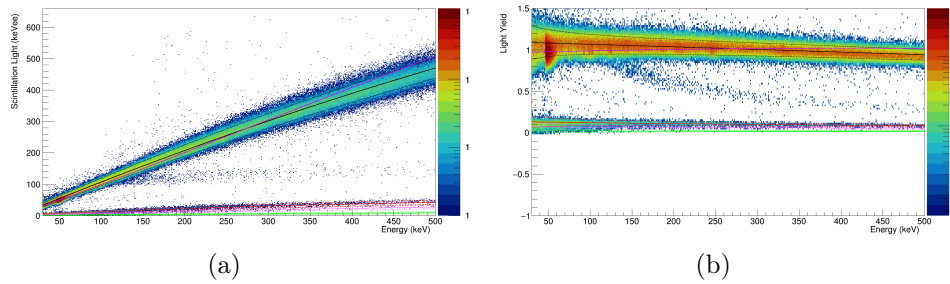


Figure B.22: Band fit result with neutron calibration dataset in the Light-Energy plane (figure B.22(a)) and in the LY-Energy plane (figure B.22(b)).

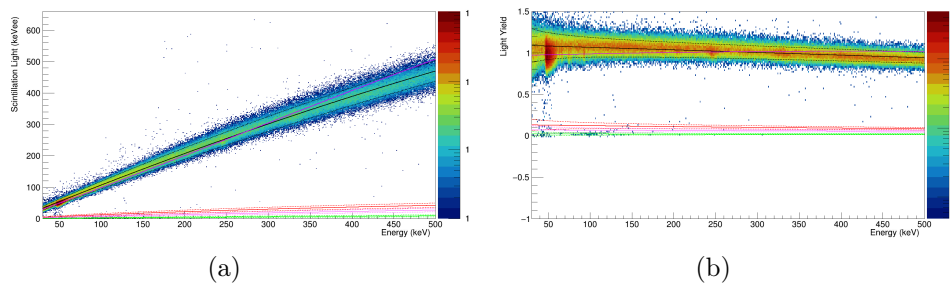


Figure B.23: Band fit result with background dataset in the Light-Energy plane (figure B.23(a)) and in the LY-Energy plane (figure B.23(b)).

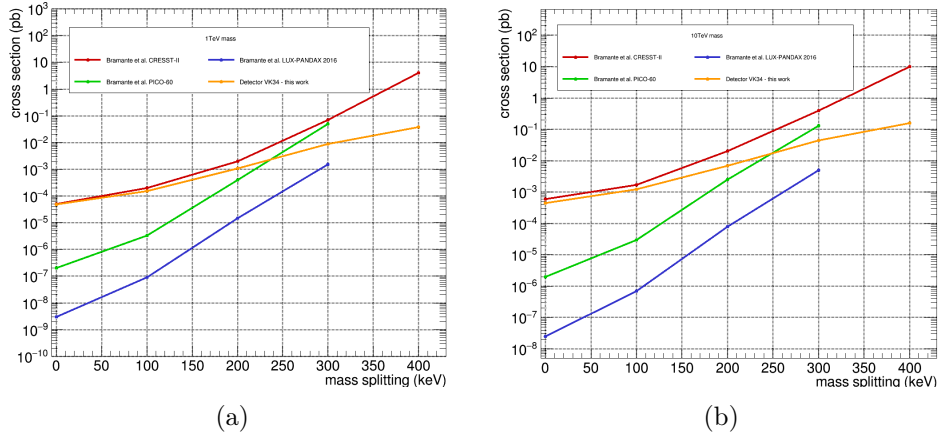


Figure B.24: Exclusion limit obtained using the energy region  $[30, 500]$  keV for a dark matter mass of 1 TeV (figure B.24(a)) and 10 TeV (figure B.24(b)).

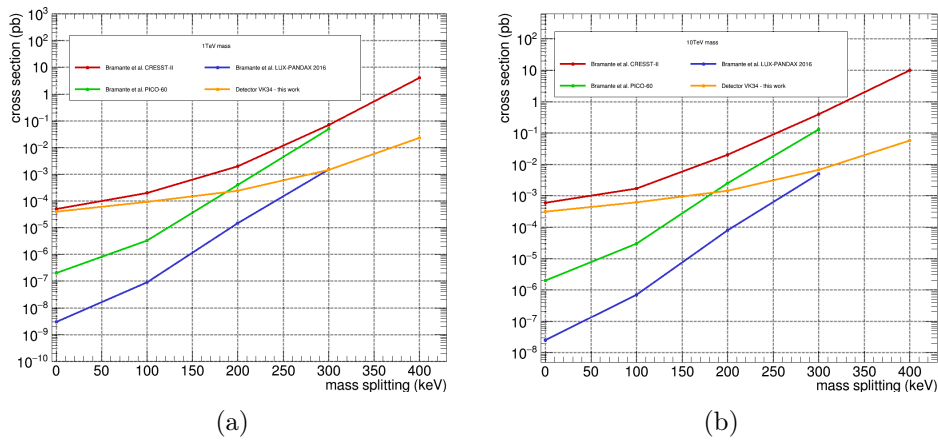


Figure B.25: Exclusion limit obtained using the energy region  $[150, 500]$  keV for a dark matter mass of 1 TeV (figure B.25(a)) and 10 TeV (figure B.25(b)).

## B.6 Detector Frederika

Design	standard
$\sigma_P$	0.109 keV
$\sigma_L$	0.236 keV
Exposure	137.01 kg day

Table B.6: Detector information.

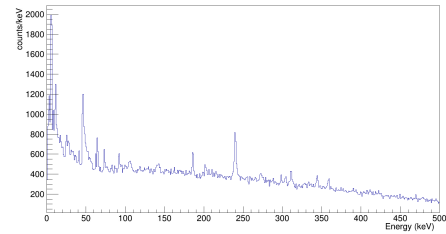


Figure B.26: Energy spectrum.

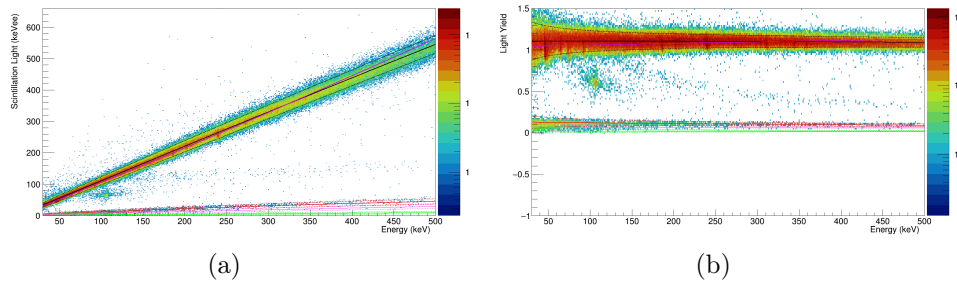


Figure B.27: Band fit result with neutron calibration dataset in the Light-Energy plane (figure B.27(a)) and in the LY-Energy plane (figure B.27(b)).

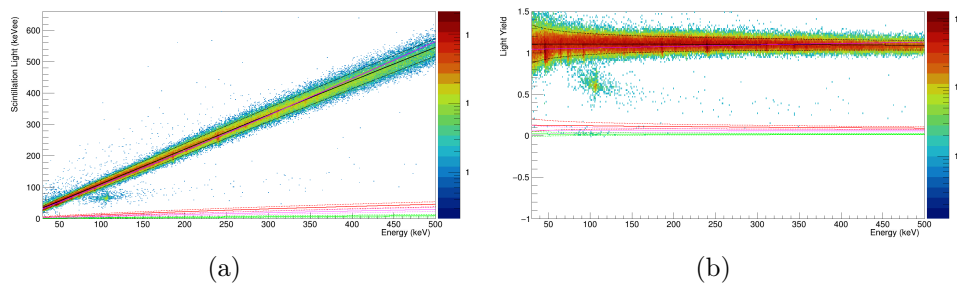


Figure B.28: Band fit result with background dataset in the Light-Energy plane (figure B.28(a)) and in the LY-Energy plane (figure B.28(b)).

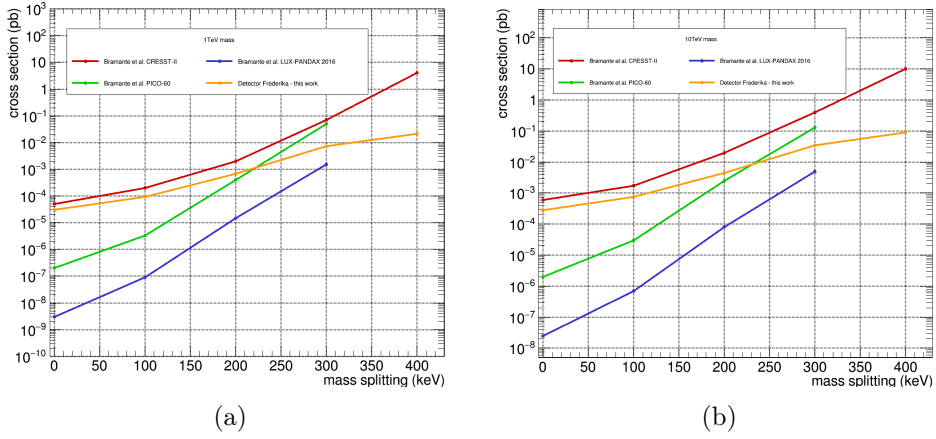


Figure B.29: Exclusion limit obtained using the energy region  $[30, 500]$  keV for a dark matter mass of 1 TeV (figure B.29(a)) and 10 TeV (figure B.29(b)).

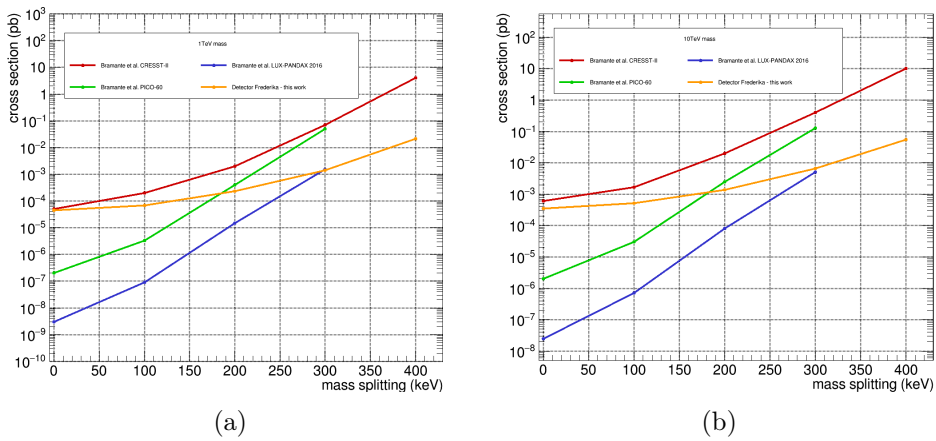


Figure B.30: Exclusion limit obtained using the energy region  $[150, 500]$  keV for a dark matter mass of 1 TeV (figure B.30(a)) and 10 TeV (figure B.30(b)).

## B.7 Detector Verena

Design	standard
$\sigma_P$	0.103 keV
$\sigma_L$	0.281 keV
Exposure	164.831 kg day

Table B.7: Detector information.

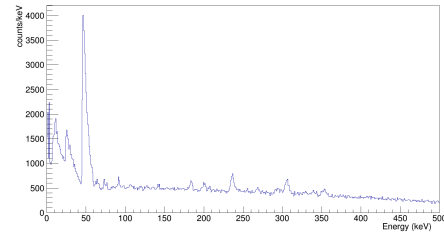


Figure B.31: Energy spectrum.

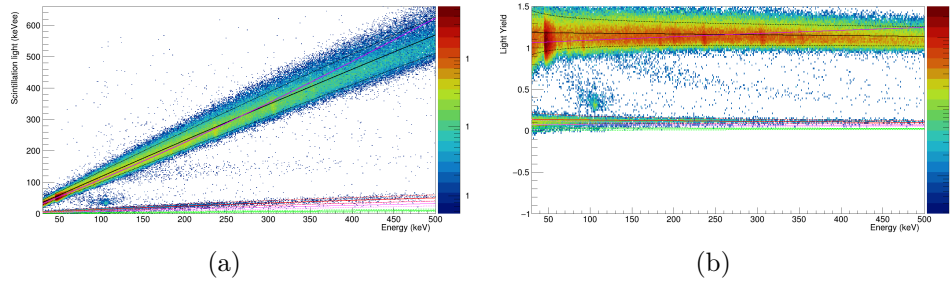


Figure B.32: Band fit result with neutron calibration dataset in the Light-Energy plane (figure B.32(a)) and in the LY-Energy plane (figure B.32(b)).

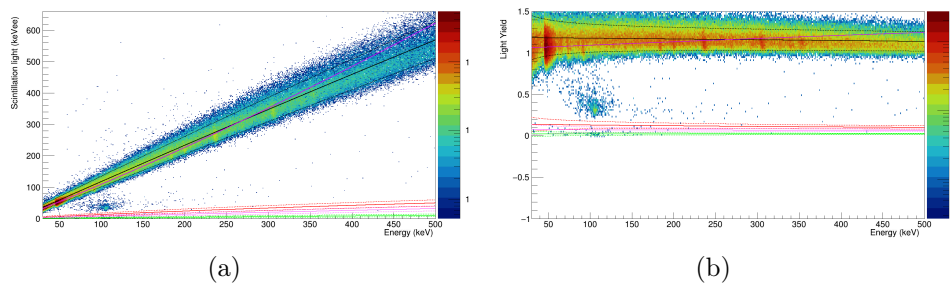


Figure B.33: Band fit result with background dataset in the Light-Energy plane (figure B.33(a)) and in the LY-Energy plane (figure B.33(b)).

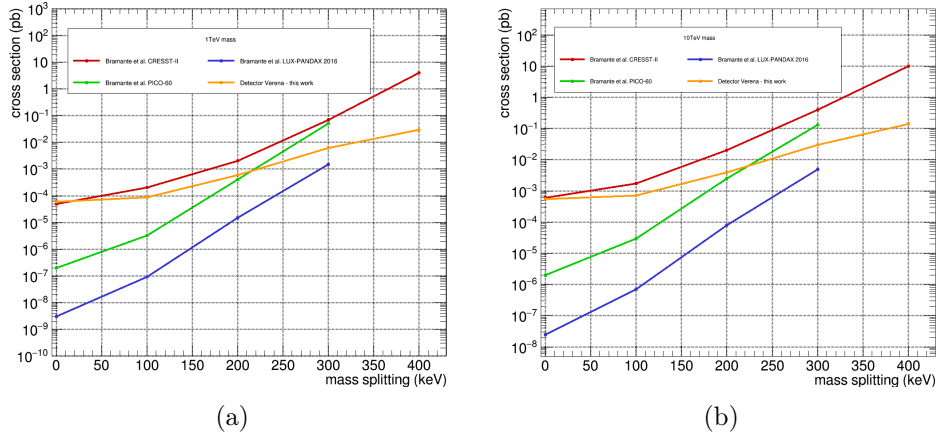


Figure B.34: Exclusion limit obtained using the energy region  $[30, 500]$  keV for a dark matter mass of 1 TeV (figure B.34(a)) and 10 TeV (figure B.34(b)).

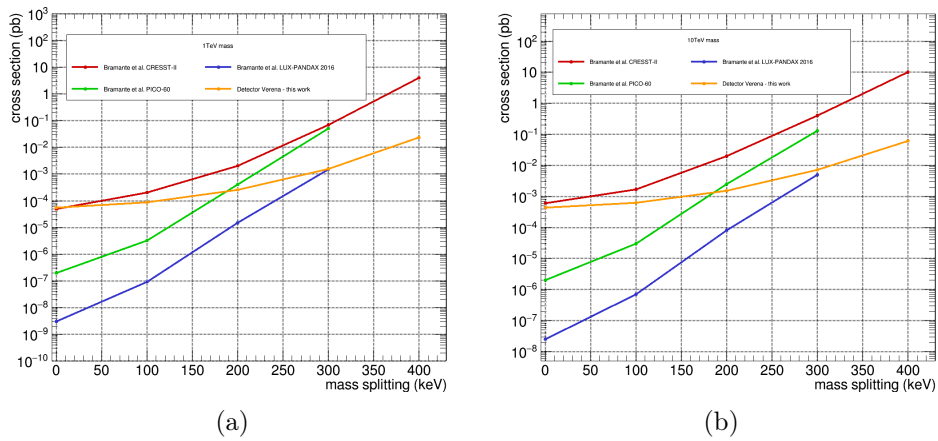


Figure B.35: Exclusion limit obtained using the energy region  $[150, 500]$  keV for a dark matter mass of 1 TeV (figure B.35(a)) and 10 TeV (figure B.35(b)).

## B.8 Detector VK33

Design	standard
$\sigma_P$	0.158 keV
$\sigma_L$	0.8 keV
Exposure	161.576 kg day

Table B.8: Detector information.

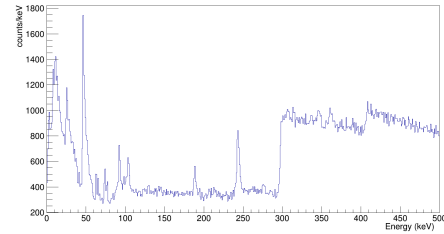


Figure B.36: Energy spectrum.

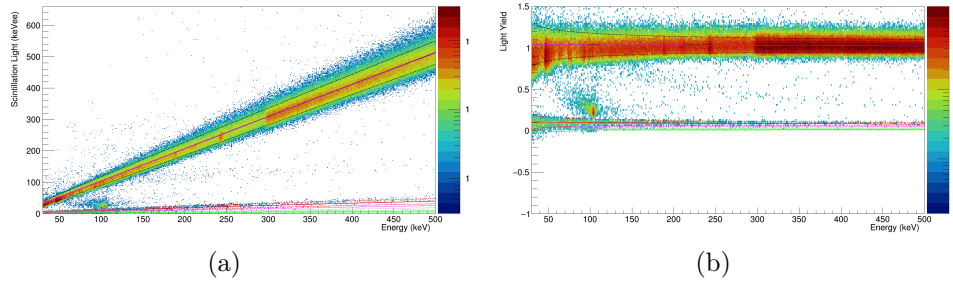


Figure B.37: Band fit result with neutron calibration dataset in the Light-Energy plane (figure B.37(a)) and in the LY-Energy plane (figure B.37(b)).

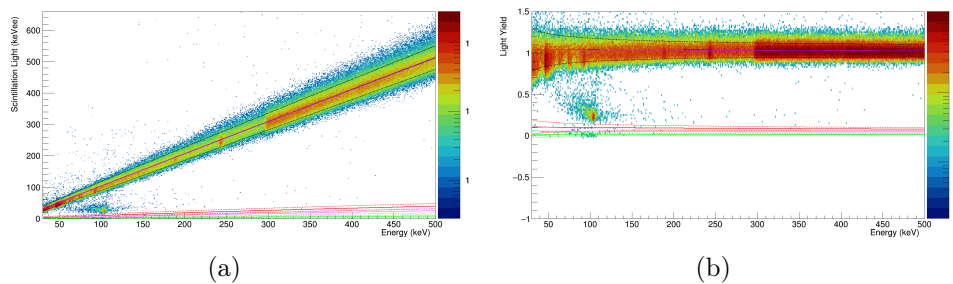


Figure B.38: Band fit result with background dataset in the Light-Energy plane (figure B.38(a)) and in the LY-Energy plane (figure B.38(b)).

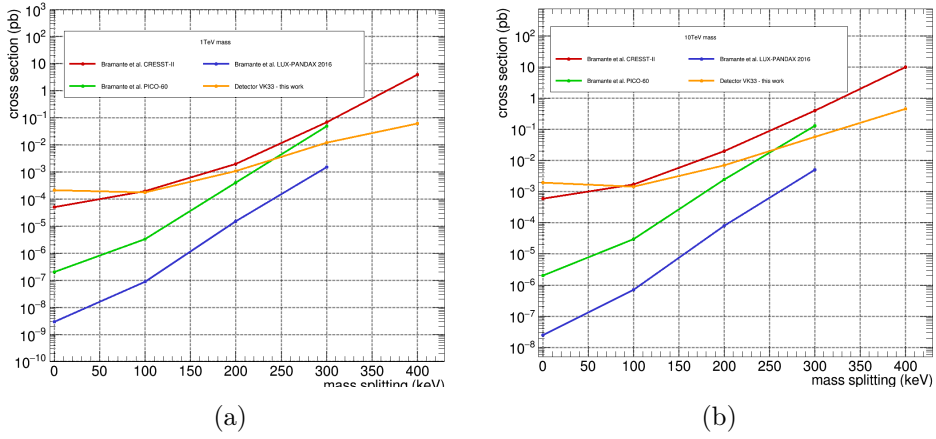


Figure B.39: Exclusion limit obtained using the energy region  $[30, 500]$  keV for a dark matter mass of 1 TeV (figure B.39(a)) and 10 TeV (figure B.39(b)).

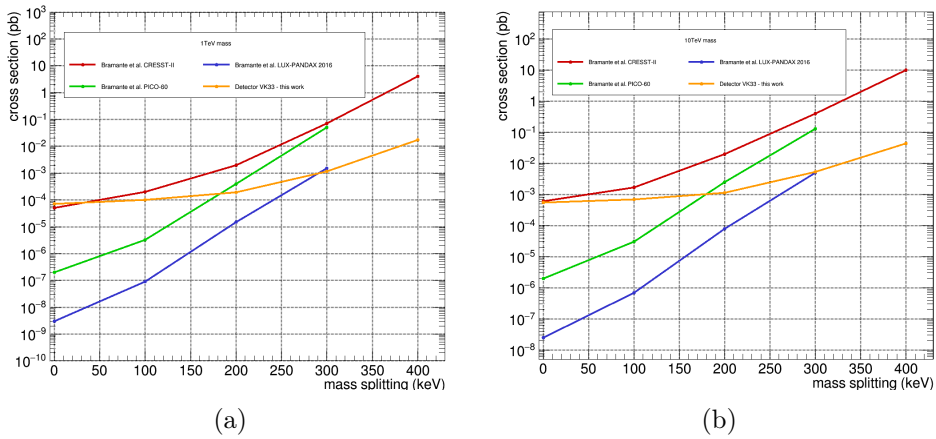


Figure B.40: Exclusion limit obtained using the energy region  $[150, 500]$  keV for a dark matter mass of 1 TeV (figure B.40(a)) and 10 TeV (figure B.40(b)).

## B.9 Detector Zora

Design	standard
$\sigma_P$	0.208 keV
$\sigma_L$	0.320 keV
Exposure	160.148 kg day

Table B.9: Detector information.

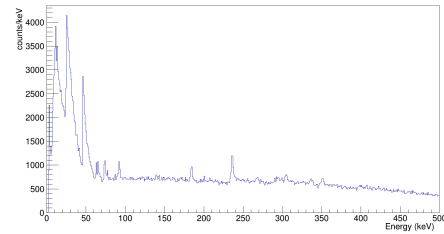


Figure B.41: Energy spectrum.

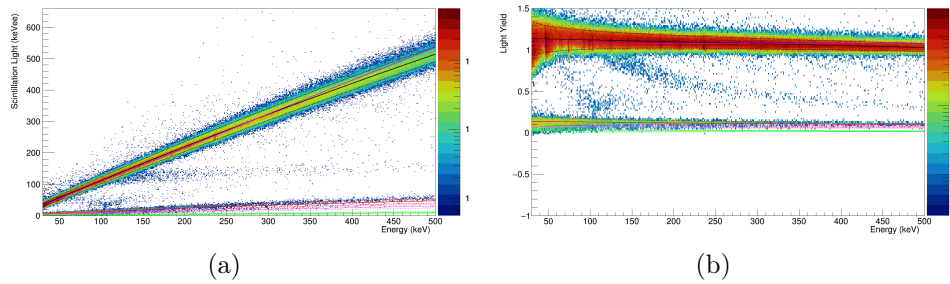


Figure B.42: Band fit result with neutron calibration dataset in the Light-Energy plane (figure B.42(a)) and in the LY-Energy plane (figure B.42(b)).

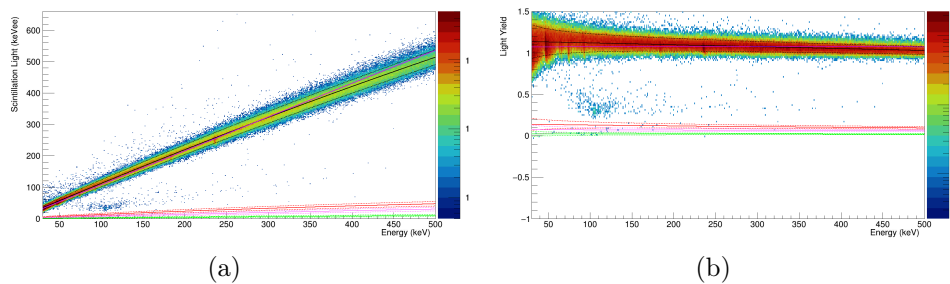


Figure B.43: Band fit result with background dataset in the Light-Energy plane (figure B.43(a)) and in the LY-Energy plane (figure B.43(b)).

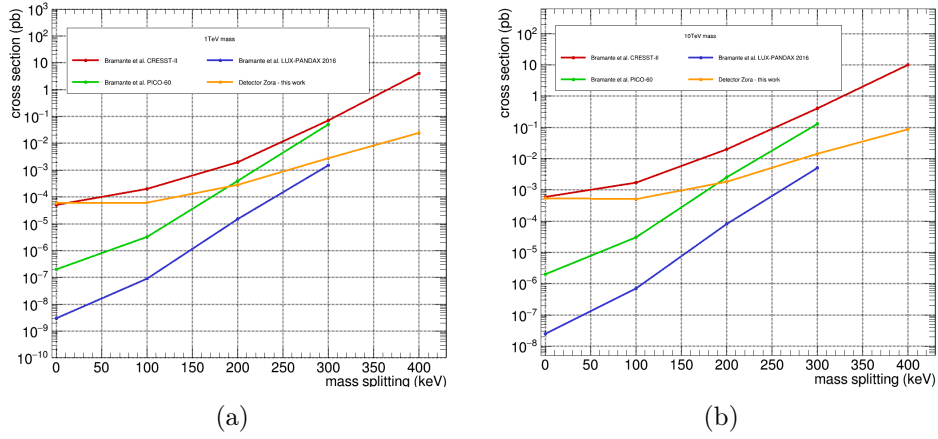


Figure B.44: Exclusion limit obtained using the energy region  $[30, 500]$  keV for a dark matter mass of 1 TeV (figure B.44(a)) and 10 TeV (figure B.44(b)).

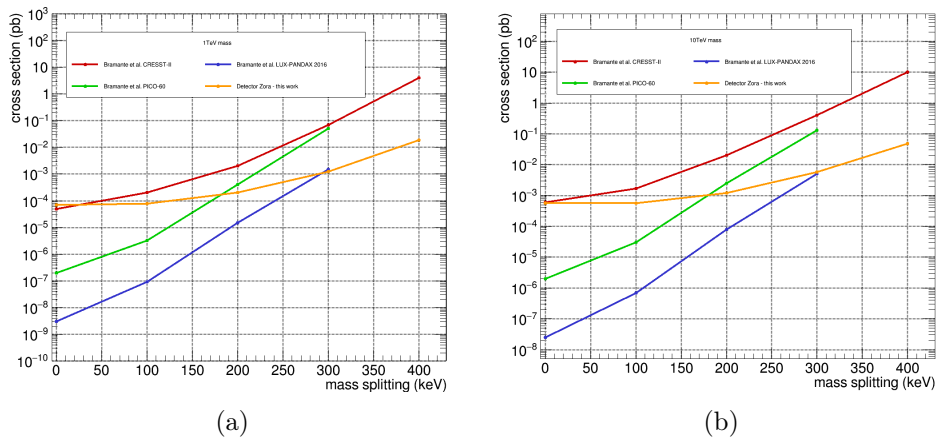


Figure B.45: Exclusion limit obtained using the energy region  $[150, 500]$  keV for a dark matter mass of 1 TeV (figure B.45(a)) and 10 TeV (figure B.45(b)).



## Bibliography

- [1] J. Bramante, P. J. Fox, G. D. Kribs, and A. Martin. “Inelastic frontier: Discovering dark matter at high recoil energy”. *Physical Review D*, 94(11), Dec 2016.
- [2] H. Kluck *et al.* “Search for low-mass Dark Matter with the CRESST Experiment”. 2017. arXiv:1711.01285.
- [3] CRESST Collaboration. “Results on light dark matter particles with a low-threshold CRESST-II detector”. *The European Physical Journal C*, 76(1), Jan 2016.
- [4] J. C. Kapteyn. “First Attempt at a Theory of the Arrangement and Motion of the Sidereal System”. *The Astrophysical Journal*, 55:302, May 1922.
- [5] J. H. Oort. “The force exerted by the stellar system in the direction perpendicular to the galactic plane and some related problems”. *Bulletin of the Astronomical Institutes of the Netherlands*, 6:249, Aug 1932.
- [6] F. Zwicky. “Die Rotverschiebung von extragalaktischen Nebeln”. *Helvetica Physica Acta*, 6:110–127, Jan 1933.
- [7] H. Andernach and F. Zwicky. “English and Spanish Translation of Zwicky’s (1933) The Redshift of Extragalactic Nebulae”. 2017.
- [8] F. Zwicky. “On the Masses of Nebulae and of Clusters of Nebulae”. *The Astrophysical Journal*, 86:217, Oct 1937.
- [9] H. W. Babcock. “The rotation of the Andromeda Nebula”. *Lick Observatory Bulletins*, 19:41–51, 1939.
- [10] J. H. Oort. “Some Problems Concerning the Structure and Dynamics of the Galactic System and the Elliptical Nebulae NGC 3115 and 4494”. *The Astrophysical Journal*, 91:273, April 1940.
- [11] K. C. Freeman. “On the Disks of Spiral and so Galaxies”. *The Astrophysical Journal*, 160:811, June 1970.
- [12] V. C. Rubin, W. Kent, and Jr. Ford. “Rotation of the Andromeda Nebula from a Spectroscopic Survey of Emission Regions”. *The Astrophysical Journal*, 159:379, February 1970.

- [13] V. C. Rubin, Jr. Ford, W. Kent, and N. Thonnard. “Rotational properties of 21 SC galaxies with a large range of luminosities and radii, from NGC 4605 (R=4kpc) to UGC 2885 (R=122kpc)”. *The Astrophysical Journal*, 238:471–487, Jun 1980.
- [14] M. S. Roberts. “A High-Resolution 21-CM Hydrogen-Line Survey of the Andromeda Nebula”. *The Astrophysical Journal*, 144:639, May 1966.
- [15] S. T. Gottesman, R. D. Davies, and V. C. Reddish. “A Neutral Hydrogen Survey of the Southern Regions of the Andromeda Nebula”. *Monthly Notices of the Royal Astronomical Society*, 133(4):359–387, September 1966.
- [16] M. S. Roberts and R. N. Whitehurst. “The rotation curve and geometry of M 31 at large galactocentric distances”. *The Astrophysical Journal*, 201:327, October 1975.
- [17] D. H. Rogstad and G. S. Shostak. “Gross Properties of Five Scd Galaxies as Determined from 21-centimeter Observations”. *The Astrophysical Journal*, 176:315, September 1972.
- [18] <https://www.eso.org/public/images/eso1424a/>.
- [19] E. Corbelli and P. Salucci. “The extended rotation curve and the dark matter halo of M33”. *Monthly Notices of the Royal Astronomical Society*, 311(2):441–447, January 2000.
- [20] W. Tucker *et al.* “1E 0657-56: A Contender for the Hottest Known Cluster of Galaxies”. *The Astrophysical Journal*, 496(1):L5–L8, March 1998.
- [21] D. Clowe, A. Gonzalez, and M. Markevitch. “Weak-Lensing Mass Reconstruction of the Interacting Cluster 1E 0657-558: Direct Evidence for the Existence of Dark Matter”. *The Astrophysical Journal*, 604(2):596–603, April 2004.
- [22] M. Markevitch *et al.* “Direct Constraints on the Dark Matter Self-Interaction Cross Section from the Merging Galaxy Cluster 1E 0657-56”. *The Astrophysical Journal*, 606(2):819–824, May 2004.
- [23] Maruša Bradač *et al.* “Revealing the Properties of Dark Matter in the Merging Cluster MACS J0025.4-1222”. *The Astrophysical Journal*, 687(2):959–967, November 2008.
- [24] A. A. Penzias and R. W. Wilson. “A Measurement of Excess Antenna Temperature at 4080 Mc/s”. *The Astrophysical Journal*, 142:419, July 1965.
- [25] R. H. Dicke, R. Beringer, R. L. Kyhl, and A. B. Vane. “Atmospheric Absorption Measurements with a Microwave Radiometer”. *Physical Review*, 70(5-6):340–348, September 1946.

- [26] Gamow George. “*The Creation of the Universe*”. Dover Publications, Place of publication not identified, 2004. OCLC: 764473196.
- [27] Helge Kragh. “*Cosmology and controversy: the historical development of two theories of the universe*”. Princeton Univ. Press, Princeton, NJ, 2., printing and 1. paperback printing edition, 1999. OCLC: 247664127.
- [28] J. C. Mather *et al.* “A preliminary measurement of the cosmic microwave background spectrum by the Cosmic Background Explorer (COBE) satellite”. *The Astrophysical Journal*, 354:L37, May 1990.
- [29] Dan Maoz. “*Astrophysics in a Nutshell (aka Basic Astrophysics)*”. Princeton University Press, 2007.
- [30] WMAP home page. <https://map.gsfc.nasa.gov/>.
- [31] Planck home page. <https://www.cosmos.esa.int/web/planck>.
- [32] Planck Collaboration. “Planck 2018 results. VI. Cosmological parameters”. 2018.
- [33] K. Freese. “Review of Observational Evidence for Dark Matter in the Universe and in upcoming searches for Dark Stars”. *EAS Publications Series*, 36:113–126, 2009.
- [34] A. *et al.* Rorai. “Measurement of the small-scale structure of the intergalactic medium using close quasar pairs”. *Science*, 356(6336):418–422, 2017.
- [35] V. Müller, K. Hoffmann, and S. E. Nuza. “Measuring the Cosmic Web”. *Open Astronomy*, 20(2), January 2011.
- [36] H. *et al.* Umehata. “Gas filaments of the cosmic web located around active galaxies in a protocluster”. *Science*, 366(6461):97–100, 2019.
- [37] K. Arun, S.B. Gudennavar, and C. Sivaram. “Dark matter, dark energy, and alternate models: A review”. *Advances in Space Research*, 60(1):166–186, July 2017.
- [38] M. Milgrom. “A modification of the Newtonian dynamics as a possible alternative to the hidden mass hypothesis”. *The Astrophysical Journal*, 270:365, July 1983.
- [39] M. Milgrom. “A modification of the Newtonian dynamics - Implications for galaxies”. *The Astrophysical Journal*, 270:371, July 1983.
- [40] M. Milgrom. “A Modification of the Newtonian Dynamics - Implications for Galaxy Systems”. *The Astrophysical Journal*, 270:384, July 1983.

- [41] Tanabashi *et al.* (Particle Data Group). “Review of Particle Physics”. *Phys. Rev. D*, 98:030001, Aug 2018. with 2019 update.
- [42] G. Bertone. “*Particle Dark Matter: Observations, Models and Searches*”. Cambridge University Press, 2010.
- [43] G. *et al.* Hinshaw. “Nine-year Wilkinson Microwave Anisotropy Probe (WMAP) observations: cosmological parameter results”. *The Astrophysical Journal Supplement Series*, 208(2):19, Sep 2013.
- [44] K. Petraki and R. R. Volkas. “Review of asymmetric dark matter”. *International Journal of Modern Physics A*, 28(19):1330028, Jul 2013.
- [45] S. Nussinov. “Technocosmology - could a technibaryon excess provide a “natural” missing mass candidate?”. *Physics Letters B*, 165(1):55 – 58, 1985.
- [46] G.B. Gelmini, L.J. Hall, and M.J. Lin. “What is the cosmion?”. *Nuclear Physics B*, 281(3):726 – 735, 1987.
- [47] K. M. Zurek. “Asymmetric Dark Matter: Theories, signatures, and constraints”. *Physics Reports*, 537(3):91–121, Apr 2014.
- [48] J. Kumar. “Asymmetric Dark Matter”. *AIP Conf. Proc.*, 1604(1):389–396, 2015.
- [49] R. D. Peccei and H. R. Quinn. “CPConservation in the Presence of Pseudoparticles”. *Physical Review Letters*, 38(25):1440–1443, June 1977.
- [50] R. D. Peccei and H. R. Quinn. “Constraints imposed byCPconservation in the presence of pseudoparticles”. *Physical Review D*, 16(6):1791–1797, September 1977.
- [51] A. Ringwald. “Alternative dark matter candidates: Axions”, 2016. arXiv:1612.08933.
- [52] A. Strumia and F. Vissani. “Neutrino masses and mixings and...”, 2006. arXiv:hep-ph/060605.
- [53] M. Drewes. “The phenomenology of right handed neutrinos”. *International Journal of Modern Physics E*, 22(08):1330019, Aug 2013.
- [54] S. Dodelson and L. M. Widrow. “Sterile neutrinos as dark matter”. *Physical Review Letters*, 72(1):17–20, Jan 1994.
- [55] Xiangdong S. and G. M. Fuller. “New Dark Matter Candidate: Nonthermal Sterile Neutrinos”. *Physical Review Letters*, 82(14):2832–2835, Apr 1999.
- [56] Hitoshi M. “Physics Beyond the Standard Model and Dark Matter”, 2007.

- [57] L. J. Hall, T. Moroi, and H. Murayama. “Sneutrino cold dark matter with lepton-number violation”. *Physics Letters B*, 424(3-4):305–312, Apr 1998.
- [58] D. Smith and N. Weiner. “Inelastic dark matter”. *Physical Review D*, 64(4), Jul 2001.
- [59] D. Tucker-Smith and N. Weiner. “The Status of Inelastic Dark Matter”. *Physical Review D*, 72(6), Sep 2005.
- [60] *et al.* Y. Cui. “Candidates for inelastic dark matter”. *Journal of High Energy Physics*, 2009(05):076–076, May 2009.
- [61] S. Chang, R. F. Lang, and N. Weiner. “Effect of Thallium Impurities in the DAMA Experiment on the Allowed Parameter Space for Inelastic Dark Matter”. *Physical Review Letters*, 106(1), Jan 2011.
- [62] G. Barello, S. Chang, and C. A. Newby. “A model independent approach to inelastic dark matter scattering”. *Physical Review D*, 90(9), Nov 2014.
- [63] D. Smith and N. Weiner. “Inelastic dark matter at DAMA, CDMS and future experiments”. *Nuclear Physics B - Proceedings Supplements*, 124:197–200, Jul 2003.
- [64] S. Chang, G. D. Kribs, D. Tucker-Smith, and N. Weiner. “Inelastic dark matter in light of DAMA/LIBRA”. *Physical Review D*, 79(4), Feb 2009.
- [65] D. P. Finkbeiner, T. Lin, and N. Weiner. “Inelastic dark matter and DAMA/LIBRA: An experimentum crucis”. *Physical Review D*, 80(11), Dec 2009.
- [66] N. Arkani-Hamed, D. P. Finkbeiner, T. R. Slatyer, and N. Weiner. “A theory of dark matter”. *Physical Review D*, 79(1), Jan 2009.
- [67] T. Piffl, C. Scannapieco, and *et al.* “The RAVE survey: the Galactic escape speed and the mass of the Milky Way”. *Astronomy & Astrophysics*, 562:A91, Feb 2014.
- [68] N. Trevisani. “Collider searches for dark matter (ATLAS + CMS)”. *Universe*, 4:131, 11 2018.
- [69] E. Tolley. “Dark Matter searches with the ATLAS Detector”. *PoS, ICHEP2018*:171, 2019.
- [70] W. C. Kalderon. “Dark Matter searches with the ATLAS Detector”. In *Proceedings of XXVI International Workshop on Deep-Inelastic Scattering and Related Subjects — PoS(DIS2018)*. Sissa Medialab, September 2018.
- [71] G. Gomez-Ceballos. “Dark Matter Searches with the CMS Experiment”. In *Proceedings of 2nd World Summit: Exploring the Dark Side of the Universe — PoS(EDSU2018)*. Sissa Medialab, November 2018.

- [72] D. Vannerom. “Dark Matter searches with CMS”. *PoS*, DIS2019:111, 2019.
- [73] R. Essig, J. Mardon, and T. Volansky. “Direct detection of sub-GeV dark matter”. *Physical Review D*, 85(7), Apr 2012.
- [74] R. Agnese *et al.* “Results from the Super Cryogenic Dark Matter Search Experiment at Soudan”. *Physical Review Letters*, 120(6), Feb 2018.
- [75] Q. Arnaud *et al.* “Optimizing EDELWEISS detectors for low-mass WIMP searches”. *Physical Review D*, 97(2), Jan 2018.
- [76] CRESST Collaboration. “First results from the CRESST-III low-mass dark matter program”. *Physical Review D*, 100(10), Nov 2019.
- [77] D. S. Akerib *et al.* “Results from a Search for Dark Matter in the Complete LUX Exposure”. *Physical Review Letters*, 118(2), Jan 2017.
- [78] X. Cui *et al.* “Dark Matter Results from 54-Ton-Day Exposure of PandaX-II Experiment”. *Physical Review Letters*, 119(18), Oct 2017.
- [79] E. Aprile *et al.* “Dark Matter Search Results from a One Ton-Year Exposure of XENON1T”. *Physical Review Letters*, 121(11), Sep 2018.
- [80] P. Agnes *et al.* “DarkSide-50 532-day dark matter search with low-radioactivity argon”. *Physical Review D*, 98(10), Nov 2018.
- [81] R. Bernabei *et al.* “First model independent results from DAMA/LIBRA-phase2”. *Nuclear Physics and Atomic Energy*, 19(4):307–325, Dec 2018.
- [82] J. Amaré *et al.* “First Results on Dark Matter Annual Modulation from the ANAIS-112 Experiment”. *Physical Review Letters*, 123(3), Jul 2019.
- [83] G. Adhikari *et al.* “Search for a Dark Matter-Induced Annual Modulation Signal in NaI(Tl) with the COSINE-100 Experiment”. *Physical Review Letters*, 123(3), Jul 2019.
- [84] G. D’imperio *et al.* “The SABRE experiment for dark matter search”. In *Proceedings of The 39th International Conference on High Energy Physics — PoS(ICHEP2018)*. Sissa Medialab, August 2019.
- [85] K. Schäffner *et al.* “A NaI-Based Cryogenic Scintillating Calorimeter: Results from a COSINUS Prototype Detector”. *J. Low. Temp. Phys.*, 193(5-6):1174–1181, 2018.
- [86] A. Aguilar-Arevalo *et al.* “Constraints on Light Dark Matter Particles Interacting with Electrons from DAMIC at SNOLAB”. *Physical Review Letters*, 123(18), Oct 2019.

- [87] I. Giomataris *et al.* “A novel large-volume spherical detector with proportional amplification read-out”. *Journal of Instrumentation*, 3(09):P09007–P09007, Sep 2008.
- [88] C. Amole *et al.* “Dark matter search results from the complete exposure of the PICO-60 C3F8 bubble chamber”. *Physical Review D*, 100(2), Jul 2019.
- [89] The MOSCAB Collaboration. “MOSCAB: A geyser-concept bubble chamber to be used in a dark matter search”, 2017.
- [90] J. B. R. Battat *et al.* “Low threshold results and limits from the DRIFT directional dark matter detector”. *Astroparticle Physics*, 91:65–74, May 2017.
- [91] C. Deaconu *et al.* “Measurement of the directional sensitivity of Dark Matter Time Projection Chamber detectors”. *Physical Review D*, 95(12), Jun 2017.
- [92] Y. Tao *et al.* “Track length measurement of  $^{19}\text{F}^+$  ions with the MIMAC Dark Matter directional detector prototype”, 2019.
- [93] T. Hashimoto *et al.* “Development of a low-alpha-emitting  $\mu$ -PIC for NEWAGE direction-sensitive dark-matter search”. *AIP Conference Proceedings*, 1921(1):070001, 2018.
- [94] G. De Lellis. “Directional dark matter search with the NEWSdm experiment”. *EPJ Web of Conferences*, 209:01019, 2019.
- [95] G. Bellini *et al.* “Cosmic-muon flux and annual modulation in Borexino at 3800 m water-equivalent depth”. *Journal of Cosmology and Astroparticle Physics*, 2012(05):015–015, may 2012.
- [96] C. Arpesella *et al.* “Radon measurements in the Gran Sasso Underground Laboratory”. *Health Phys*, 72(4):629–632, Apr 1997.
- [97] F. Pobell. “*Matter and Methods at Low Temperatures*”. Springer Berlin Heidelberg, 2007.
- [98] F. Pröbst *et al.* . “Model for cryogenic particle detectors with superconducting phase transition thermometers”. *Journal of Low Temperature Physics*, 100(1-2):69–104, July 1995.
- [99] P. Debye. “Zur Theorie der spezifischen Wärmen”. *Annalen der Physik*, 344(14):789–839, 1912.
- [100] C. Kittel. “*Introduction to Solid State Physics*”. Wiley, 8 edition, 2004.
- [101] K.D. Irwin and G.C. Hilton. “Transition-Edge Sensors”. In Christian Enss, editor, *Cryogenic Particle Detection*, pages 63–150. Springer Berlin Heidelberg, Berlin, Heidelberg, 2005.

- [102] J. F. Cochran and D. E. Mapother. “Superconducting Transition in Aluminum”. *Physical Review*, 111(1):132–142, July 1958.
- [103] J. B. Birks. “*The theory and practice of scintillation counting*”. Pergamon Press Oxford [England], 1964.
- [104] W. R. Leo. “*Techniques for nuclear and particle physics experiments: a how-to approach*”. Springer, Berlin, 1994.
- [105] K. Schäffner. “Study of Backgrounds in the CRESST Dark Matter Search”, 2013. PhD Thesis, Technische Universität München.
- [106] R. Strauss *et al.* “Energy-dependent light quenching in CaWO<sub>4</sub> 4 crystals at mK temperatures”. *The European Physical Journal C*, 74(7), July 2014.
- [107] Interactive chart of nuclides. <https://www.nndc.bnl.gov/nudat2/chartNuc.jsp>.
- [108] C. Bruhn. “Production and Characterization of Scintillating CaWO<sub>4</sub> Single Crystals for Rare Event Searches”, 2015. Master’s Thesis, Technische Universität München.
- [109] C. Oppenheimer. “Development, production and characterization of high-purity CaWO<sub>4</sub> crystals for the CRESST-experiment”, 2016. Master’s Thesis, Technische Universität München.
- [110] R. F. Lang *et al.* “Electron and gamma background in CRESST detectors”. *Astroparticle Physics*, 32(6):318–324, Jan 2010.
- [111] F. Reindl. “Exploring Light Dark Matter With CRESST-II Low-Threshold Detectors”, 2016. PhD Thesis, Technische Universität München.
- [112] R. Strauss *et al.* “Beta/gamma and alpha backgrounds in CRESST-II Phase 2”. *Journal of Cosmology and Astroparticle Physics*, 2015(06):030–030, Jun 2015.
- [113] R. F. Lang *et al.* “Scintillator Non-Proportionality and Gamma Quenching in CaWO<sub>4</sub>”, 2009.
- [114] W. W. Moses and S. A. Payne and W. -. Choong and G. Hull and B. W. Reutter. “Scintillator Non-Proportionality: Present Understanding and Future Challenges”. *IEEE Transactions on Nuclear Science*, 55(3):1049–1053, 2008.
- [115] D. Schmiedmayer. “Calculation of Dark-Matter Exclusion-Limits using a Maximum Likelihood Approach”, 2019.
- [116] P. Huff. “The Detector Parameters Determining the Sensitivity of the CRESST-II Experiment”, 2010.

- 
- [117] J. Schmaler. “The CRESST Dark Matter Search - New Analysis Methods and Recent Results”, 2010.
- [118] Table of radioactive isotopes. <http://nucleardata.nuclear.lu.se/toi/nuclide.asp?iZA=740483>.
- [119] R. Barlow. “Extended maximum likelihood”. *Nuclear Instruments and Methods in Physics Research Section A: Accelerators, Spectrometers, Detectors and Associated Equipment*, 297(3):496 – 506, 1990.
- [120] G. Cowan, K. Cranmer, E. Gross, and O. Vitells. “Asymptotic formulae for likelihood-based tests of new physics”. *The European Physical Journal C*, 71(2), Feb 2011.
- [121] A. Wald. “Tests of statistical hypotheses concerning several parameters when the number of observations is large”. *Transactions of the American Mathematical Society*, 54(3):426–426, March 1943.
- [122] S. S. Wilks. “The Large-Sample Distribution of the Likelihood Ratio for Testing Composite Hypotheses”. *The Annals of Mathematical Statistics*, 9(1):60–62, March 1938.